Journal of Materials Chemistry A

ROYAL SOCIETY OF CHEMISTRY

REVIEW

View Article Online
View Journal | View Issue

Cite this: J. Mater. Chem. A, 2025, 13, 5447

Advances in gas sensors using screen printing

Mohamed Ahmed Belal, [a] Sugato Hajra, [a] Swati Panda,[a] Kushal Ruthvik Kaja,[a] Mohamed Magdy Mohamed Abdo, [b] Ahmed Abd El-Moneim,[c] Dawid Janas, [d] Yogendra Kumar Mishra [e] and Hoe Joon Kim *[a]

Received 17th September 2024
Accepted 23rd December 2024

DOI: 10.1039/d4ta06632d

rsc.li/materials-a

Gas sensing is crucial for detecting and monitoring hazardous, gases in various environments to ensure safety and prevent potential health risks. It helps in the early identification of gas leaks, air quality monitoring, and environmental protection, contributing to public health and industrial safety. Screen-printed gas sensors are trending nowadays due to their ability to fabricate electrodes or deposit functional components onto substrates and their cost-effective and scalable manufacturing process, making them suitable for mass production. This review provides an overview of screen printing and hybrid screen printing techniques utilizing different methods, such as spin coating, drop casting, spray coating, and inkjet printing (IJP), with screen printing for various gas sensing applications. The mechanism of each hazardous gas detection technique, their precision in the identification of hazardous gases, and their impact on sensor enhancement were thoroughly analyzed. Furthermore, the vital integration of screen-printed gas sensors with various futuristic technologies, such as artificial intelligence (AI), machine learning (ML), and Internet of Things (IoT) devices, supercapacitors (SCs), triboelectric nanogenerators (TENGs), and microheaters, was demonstrated to enhance sensor

[a]Department of Robotics and Mechatronics Engineering, Daegu Gyeongbuk Institute of Science and Technology, Daegu 42988, South Korea. E-mail: joonkim@dgist.ac.kr
[b]Physics and Mathematics Engineering Department, Faculty of Engineering, Ain Shams University, Cairo, 11535, Egypt. E-mail: engmohamed.abdo92@eng.asu.edu.eg
[c]Graphene Center of Excellence for Energy and Electronic Applications, Egypt-Japan University of Science and Technology, New Borg El-Arab 21934, Egypt
[d]Department of Organic Chemistry, Bioorganic Chemistry and Biotechnology, Silesian University of Technology, B. Krzywoustego 4, 44-100 Gliwice, Poland
[e]Mads Clausen Institute, NanoSYD, University of Southern Denmark, Alsion 2, 6400, Sønderborg, Denmark

Mohamed Ahmed Belal

Mr Mohamed A. Belal is a PhD candidate in the Robotics and Mechatronics Engineering Department, Daegu Gyeongbuk Institute of Science and Technology (DGIST), South Korea. He worked as a lab engineer and research assistant at the Egypt-Japan University of Science and Technology (Egypt, 2021–2024). He received a master's degree in organic chemistry from the Chemistry Department at Alexandria University (Egypt, 2019) and a BSc in Chemistry/Physics from the Faculty of Science at Damanhur University (Egypt, 2007–2011). His research interest focuses on gas sensors, supercapacitors, and inkjet printing technologies.

Sugato Hajra

Dr Sugato Hajra is currently a Postdoctoral fellow at the Daegu Gyeongbuk Institute of Science and Technology. He completed his PhD in the Department of Robotics and Mechatronics Engineering, Daegu Gyeongbuk Institute of Science and Technology, South Korea, in 2024. He received a Bachelor in Technology degree from Siksha O Anusandhan University, India, in 2017. He persued his M Tech degree with a specialization in VLSI and Embedded Systems at Siksha O Anusandhan University and also served as a joint researcher at the Advanced Multifunctional and Materials Laboratory in the Institute of Technical Education and Research, Bhubaneswar, India, in 2019. His research interests mainly include lead-free piezoelectric/multiferroic materials, metal–organic frameworks, solid-state electronic devices, and hybrid energy harvesters.

performance and broaden the application area. Moreover, this review highlighted the importance of sensors' sensitivity, selectivity, and environmental stability, which offer plenty of room for innovation. For future improvements, the integration of microfluidic, multi-sensor arrays, functional coatings, and nanomaterials into screen-printed gas sensor devices was proposed. In this context, gas sensing platforms can be refined by operating them using energy harvesting principles, improving their environmental stability, and making them wearable and flexible. This review paper would benefit many researchers and readers working in this field to familiarize themselves with the recent breakthroughs in the rapidly emerging field of screen-printed gas sensing.

Swati Panda

Ms Swati Panda is currently a doctoral student at the Daegu Gyeongbuk Institute of Science and Technology. She received her Bachelor's degree from Utkal University, Orissa, in 2018. She pursued her Master's degree from Siksha O Anusandhan University with a specialization in biotechnology in 2020. Her research interests focus on self-powered biosensors and triboelectric-piezoelectric energy harvesters.

Kushal Ruthvik Kaja

Mr Kushal Ruthvik Kaja is currently a doctoral student at the Daegu Gyeongbuk Institute of Science and Technology. He received a Bachelor's degree from Andhra Loyola College, India, in 2021. He received his Master's in Physics from VIT-AP University, India, in 2023. His research interests focus on solid–solid, solid–liquid and waste-based triboelectric energy harvesters.

Yogendra Kumar Mishra

Dr Yogendra Kumar Mishra is a Professor and the leader of the Smart Materials group at Mads Clausen Institute, NanoSYD, University of Southern Denmark (SDU). Before joining SDU, he led a group at the Functional Nanomaterials Chair, Kiel University, Germany, following anAlexander von Humboldt fellowship. He earned his habilitation (2015) in Materials Science from Kiel University and a PhD in Physics (2008) from Jawaharlal Nehru University (JNU) in New Delhi, India. He developed a new flame-based process for tetrapod nanostructuring and their 3D networks as cellular solids, which found many applications, including their use as sacrificial templates for structuring new materials. The Smart Materials group's main focus is to develop a new class of advanced materials for future green and sustainable technologies.

Hoe Joon Kim

Dr Hoe Joon Kim is currently an Associate Professor of Robotics and Mechatronics Engineering at the Daegu Gyeongbuk Institute of Science and Technology (DGIST), Daegu, South Korea, and holds a courtesy appointment in the Information and Communication Engineering Department. He received his BS degree from Johns Hopkins University, Baltimore, MD, USA, in 2009, and MS and PhD degrees from the University of Illinois at Urbana–Champaign, Urbana, IL, USA, in 2011 and 2015, respectively, all in mechanical engineering. He held a post-doctoral position at the Micro and Nano Systems Laboratory, Carnegie Mellon University, Pittsburgh, PA, USA, where he was involved in the development of low-power low-noise piezoelectric MEMS resonators for sensing and frequency control applications. His research interests focus on piezoelectric MEMS resonators for RF wireless communication, nanogenerators, chemical/physical sensing, environmental monitoring, and emerging nanomaterials.

1. Introduction

Hazardous gases are harmful to human been health and ecosystems, ranging from industrial accidents to environmental and engineering developments that have facilitated the progression of gas-sensing technologies.[1–7] These gases, whether originating from industrial sectors, emissions from transportation, or natural sources, are reported as a substantial hazard because of their detrimental impacts on the respiratory and nervous systems, general health, and environmental well-being.[8–10] This is why many people require dependable and effective detection systems to monitor the levels of harmful gases that have risen due to growing urbanization and industrialization.[2,11–13] Air pollution worldwide poses substantial threats to air quality, human health, and the climate, as it is linked to carbon dioxide (CO_2) emissions from fossil fuels.[14–21] Implementing a conceptual multi-sensor array system that can be used in the Internet of Things (IoT) structure can enable the monitoring of environmental parameters.[22]

The field of gas sensing technology has been developed substantially throughout its history, propelled mostly by progress in materials science, electronics, and sensors' design.[23,24] The goal of gas sensor development is to create functional materials that can accurately and selectively distinguish complex gases. Gas-sensing devices first appeared in coal mines, where canaries were used to detect leaks.[25] The Davy lamp, invented in 1815, was the first gas detector of the industrial age[26] to identify methanol and oxygen depletion in coal mines. However, the initial proposal for chemical gas sensors was made in 1962.[27] Lastly, in recent years, many researchers have frequently focused their attention on detecting humidity and various types of gases, such as ammonia (NH_3), nitrogen dioxide (NO_2), CO_2, carbon monoxide (CO), hydrogen sulfide (H_2S), sulfur dioxide (SO_2), liquefied petroleum gas (LPG), hydrogen gas (H_2), and others.[28–39] Therefore, the detection of such gases holds significant importance in a range of applications, such as occupational safety, environmental surveillance, and regulation of indoor air quality.[40]

The use of printing techniques, such as direct writing, inkjet printing (IJP), 3D, gravure, flexo, and screen-printing, offers various time-saving procedures and enables the complete utilization of sensing signals for gas sensor applications.[35,41–44] Screen printing has a range of methods tailored to meet the requirements of applications, with the most common techniques including flatbed screen printing (FSP), rotary screen printing (RSP), and hybrid screen printing.[45] Firstly, for small-scale production and research orientation with simplicity and precision fabrication, FSP with a stationary substrate and a manual squeegee can create a high-resolution film.[46–50] On the other hand, semi-automated FSP and RSP machines are required for mass production of printed electronics, which employ a semi-automated squeegee and cylindrical screen, respectively, with ideal motion and shear stress controlled by a pneumatic system.[51–53] However, controlling the thickness of printed active layers is one of the drawbacks of screen printing technology; therefore, the hybrid method, which combines two or more printing techniques, is an efficient technique that allows the customization of highly precise electronics.[54,55]

Screen printing technology has notable benefits for printing material-based devices, including gas, temperature, humidity, pressure, strain, and biomedical sensors, solar cells, heaters, batteries, and supercapacitors.[56–58] It has several key benefits, such as low cost and large-scale production of different designs with wide versatility in working with various substrates and functional materials. Moreover, screen printing can accurately apply functional inks, which is essential for producing high-quality patterns for gas sensor applications. However, this technology also faces certain obstacles. Nevertheless, significant problems remain to be investigated, including the low-resolution patterns, optimization of mesh size, and high viscosity of the inks, which affect the physicochemical characteristics of the materials.[57,59,60] Despite this, screen-printing has the potential to grow the gas sensing industry by making it easier to produce low-cost, flexible, and remarkably high-performance sensors for a variety of applications, such as environmental monitoring, biomedical, and industrial safety systems.[36,61]

Rheological properties are important for fabricating high-precision printed films for electronic devices.[62] Therefore, some parameters, such as shear rate and yield stress, are related to the viscoelastic characteristics of the paste, which can explain the nature of the paste when applying high shear stress during printing. For non-Newtonian pastes, such as shear thinning and shear thickening, the viscoelastic properties are controlled by the type of solvent and adhesive content in organic vehicles, carrier organic solvents, and polymers.[63] Other factors, such as the mesh's pore size, surface tension, printing speed, and wall slip behavior, can directly affect the morphology and resolution of the printed film.[64] Hence, optimizing the paste rheology, selecting the appropriate mesh design, snap-off distance, and ink concentration, and controlling the motion of the squeegee lead to fabricating high-quality electrodes for gas sensors.[54,65]

Screen-printing processes have addressed many issues. Moreover, they are efficient and straightforward for depositing sensing materials onto substrates, particularly in gas sensor applications.[36,41,56,66,67] Furthermore, this technology offers numerous benefits in terms of regulating the thickness and chemical composition of sensing materials.[41] Among the several technologies, it has emerged as a versatile and cost-effective approach for producing gas sensors because it is well suited for fast prototyping due to its fast printing speed.[68] Researchers have successfully developed sensors with high sensitivity and selectivity for detecting multiple gases by utilizing the principles of screen printing.[35] This technique entails depositing functional materials onto substrates using a silk screen with an optimized mesh size.[36]

A diverse range of materials, carefully selected for their ability to detect and selectively detect specific target gases, are essential for screen-printed gas sensing. The new materials can be used as sensing materials, such as titanium carbide MXene ($Ti_3C_2T_x$), zeolitic imidazolate framework-67 metal–organic framework (ZIF-67 MOF), cobalt(II,III) oxide (Co_3O_4), nickel cobaltite ($NiCo_2O_4$), alpha-phase iron(III) oxide (hematite-α-

Fe_2O_3), molybdenum diselenide ($MoSe_2$), vanadium carbide MXene (V_2CT_X), vanadium(v) oxide (vanadium pentoxide-V_2O_5), tin(iv) oxide (tin dioxide-SnO_2), copper(ii) oxide (CuO), zinc oxide (ZnO), gallium(iii) oxide (Ga_2O_3), aluminum oxide (alumina-Al_2O_3), V_2CT_x/SnS_2, silver telluride (Ag_2Te), ZnO@ZIF-8 and tungsten(vi) oxide (tungsten trioxide-WO_3), which are cost-effective and easily manufacturable gas sensors.[30,37,69–88] However, the applicability of some oxides, such as ZnO and SnO_2, is limited due to their high operating temperature (200–500 °C), prolonged recovery time, and low selectivity.[89]

By using cutting-edge nanomaterials with high surface activity and improved gas adsorption at lower temperatures, such as doped metal oxides, 2D materials (like graphene), or perovskites, the operating temperature of gas sensors with rigid or flexible substrates can be lowered. MOF materials such as ZIF-8 and ZIF-67 were used to make a composite of MOF-metal oxides such as ZIF-8@ZnO to enhance their sensing capabilities at room temperature because of their surface area, adjustable conductivity, and responsiveness to gas molecules.[38,83,87,90–93] A further issue emerges from the utilization of rigid substrates such as corning glass, seashells, and alumina, thereby limiting their suitability for wearable IoT applications, which need flexible substrates such as polyethylene terephthalate (PET), polyimide (PI), and cellulose nanofibers (CNFs).[41,42,93–95] Researchers are currently working on reducing the operating temperature of gas sensors to address this issue.[41] Lower operating temperatures are made possible by modifications such as heterostructures or noble metal catalysts (like Pt or Pd) that further increase catalytic efficiency. Gas-sensing processes can also be facilitated by using infrared (IR) or ultraviolet (UV) light activation rather than thermal excitation. Flexible substrates enable the localization of heat or light by integration with low-power microheaters or photonic devices, lowering energy requirements without sacrificing sensitivity or selectivity, which ultimately enables the creation of flexible gas sensors for use in wearable IoT devices and other applications that require flexibility and adaptability.[68,96–98]

This review paper provides an overview of screen-printing technology in toxic gas sensing applications. First, the adverse impacts of toxic gases on human well-being and the sources of these emissions are analyzed. Following that, the advancement of gas sensing technologies, tracking their progress from initial chemical indicators to modern electronic sensors, was elaborated. Particularly, the importance of screen-printing gas sensors in gas detection, emphasizing their benefits in terms of scalability, cost-effectiveness, and versatility, was highlighted. Then, a comprehensive analysis of the materials, fabrication techniques, and operational principles that form the foundation of screen-printed gas sensors, as well as the gas sensing mechanism of different gases, is provided. In addition, the review article explores the wide range of uses for these sensors in many industries and sectors,

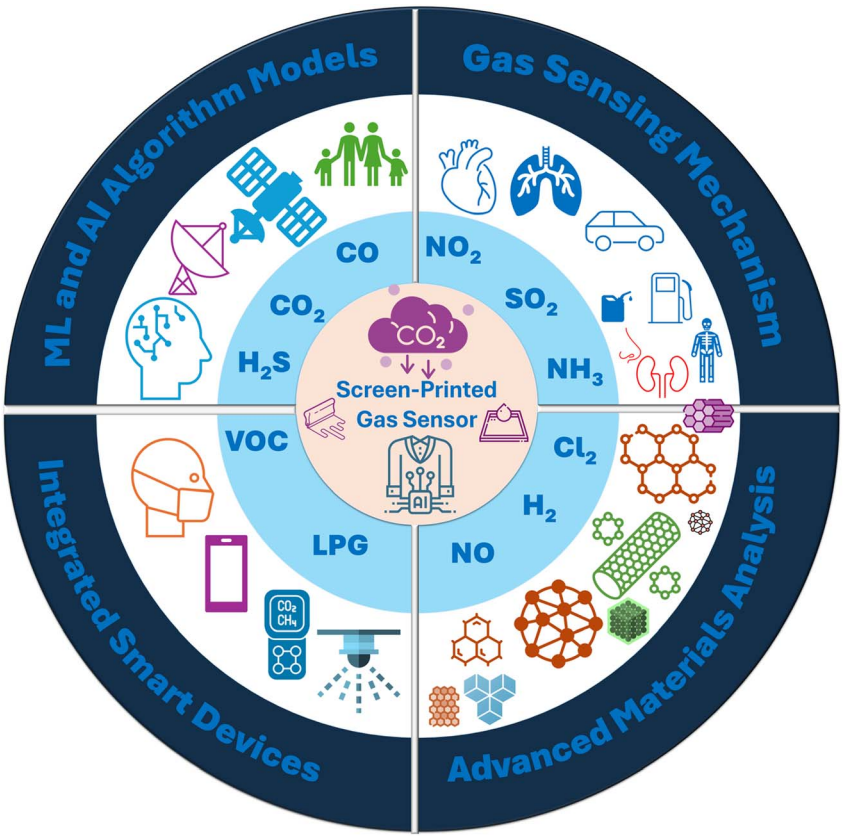

Fig. 1 Schematic overview of advanced materials analysis, gas sensing mechanism, integrated smart devices, and machine learning (ML) and artificial intelligence (AI) algorithm models.

demonstrating their ability to reduce the risk associated with exposure to harmful gases. Integration of Artificial Intelligence (AI) and Machine Learning (ML) in gas sensor data analysis was also highlighted, and the importance of using hybrid devices to improve the performance of gas detectors was discussed. Finally, this review provides significant perspectives on the current advancements in screen printing technology for the detection of toxic gases and detailed information about current challenges, future trends, and developments. A schematic overview of advanced materials analysis, gas sensing mechanisms, integrated smart devices, and ML and AI algorithm models is illustrated in Fig. 1.

2. Fabrication methods

Gas sensor manufacturing is versatile and cost-effective using screen printing technology. This technology can print a conductive transducer and heater on top of substrates, as shown in Fig. 2.[99–101] Furthermore, functional materials can be accurately and efficiently deposited on the transducer, as shown in Fig. 3a.[100] Therefore, different types of screen-printing technology or hybrid printing are necessary to employ their advantages, including the ability to produce a thin sensing layer and regulate its deposition, which can impact the performance of gas sensors. Conventional screen printing uses silk screens to apply ink to substrates to fabricate gas sensor devices.[102,103] Therefore, this approach boosts sensor performance and lifespan for many applications, as shown in Fig. 3b.[36]

FSP and RSP screen printing are two significant methods in printed electronics, each presenting unique benefits. In manual FSP, which is composed of a fixed substrate and manual squeegee, the squeegee presses ink through a stationary mesh silk screen onto a desired substrate such as alumina, PI, or PET. The manual technique is suitable for small-scale, high-resolution applications because it offers precise control over layer thickness and pattern fidelity. Nevertheless, it functions in batch mode, which restricts its scalability and throughput. Prototype development and high-resolution patterning situations commonly utilize FSP, prioritizing precision over volume production requirements.[41]

On the other hand, high-throughput production optimizes semi-automated and automated FSP, which has a controlled squeegee, and RSP, which applies ink to a continuously moving substrate beneath a rotating cylindrical mesh screen, which is upgraded to fabric. The microstructure, stabilized fabric, and balanced structure of the photosensitive coating ensure high printing quality and consistency across fine lines, solid prints, and relief designs. The design of the screen printing plate facilitates optimal ink flow, resulting in rapid and high-quality screen printing performance as discussed by Andreas Lorenz *et al.*[45,105] for using RSP for printing electronic devices. The rotary configuration facilitates seamless scalability, rendering it

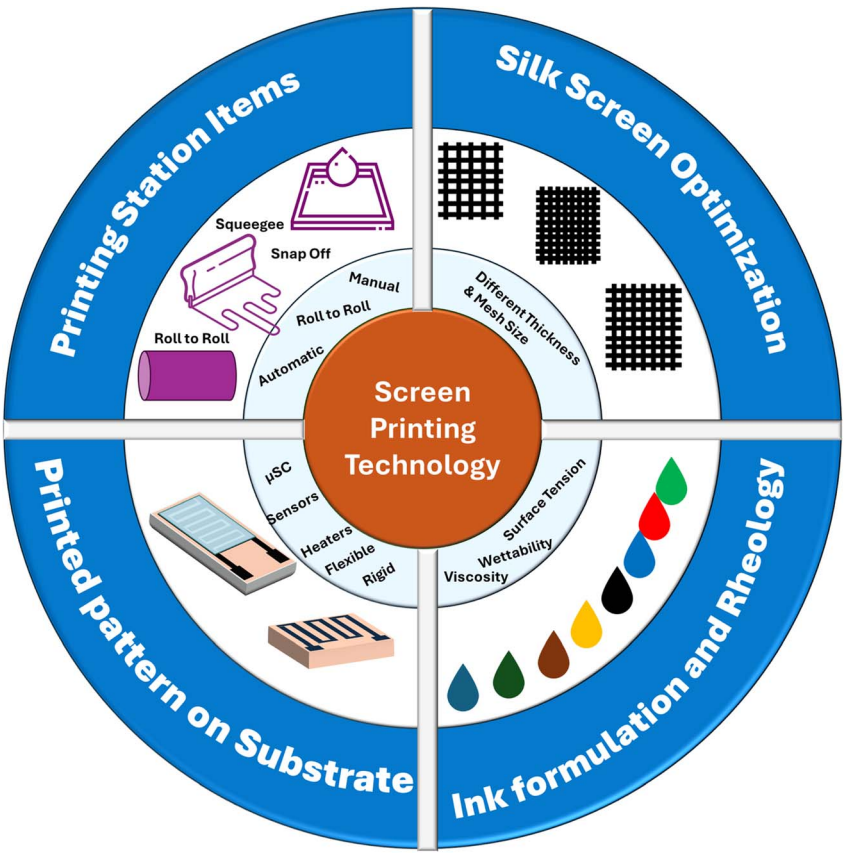

Fig. 2 Schematic diagram of screen-printing technology overview.

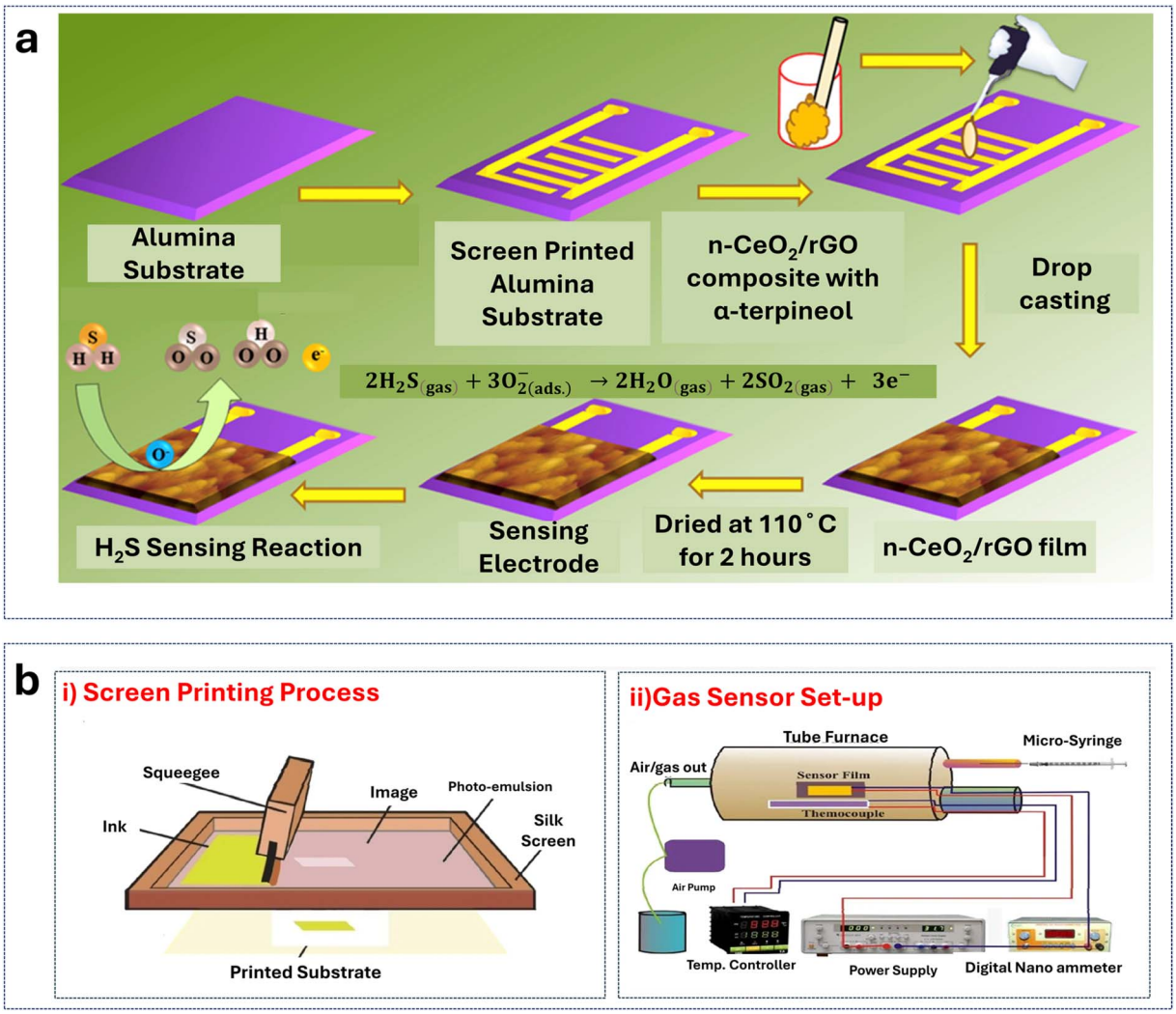

Fig. 3 Gas sensor fabrication, screen printing, and H_2S interaction are illustrated. (a) Screen printing of an IDE electrode on the top of an alumina substrate followed by drop-casting for an n-CeO_2/rGO film in square dimensions, showing the interaction with H_2S gas (reprinted with permission,[90] Copyright 2024, Elsevier); (b) schematic diagram showing the screen printing flatbed silk screen and squeegee as well as the gas sensor set-up: (i) the screen-printing method and (ii) gas set-up for a colorimetric gas sensor (reprinted with permission,[104] Copyright 2020, Springer Nature).

appropriate for large-scale production while maintaining consistent quality. RSP is great for flexible and stretchable electronics because it works well with materials such as polydimethylsiloxane (PDMS) and PET, which makes it easy to cover large applications. Additionally, it facilitates rapid production while minimizing material waste, catering to the requirements of applications including wearable sensors, flexible displays, and conductive interconnects.[106,107]

This technology is suited for many industrial applications due to its easy setup and operation. Secondly, thick-film screen printing uses high-viscosity pastes to create thick layers of functional materials for different types of gas sensors, such as colorimetric gas sensors, as shown in Fig. 4a–c.[41,56,108] Lastly, the hybrid approaches and emerging technologies use modern printing technologies such as IJP and modern aerosol jet printers to deposit particles to accurately design gas sensor devices with intricate patterns and high resolution by fabricating screen-printed electrodes and depositing functional materials by IJP. The drop-on-demand (DOD)[42] and continuous IJP technologies improve the droplet location and material efficiency, making gas sensors more sensitive and selective. These devices are used in environmental monitoring, industrial safety, and healthcare, where gas detection is crucial.[93] Hence, this section will discuss three important types of printing technology: conventional screen printing, thick film screen printing, and hybrid approaches, and emerging technologies.

Screen-printed sensors are flexible and cheap and can be fabricated from a wide range of materials, including metal oxides, metal sulfides, and graphene, as shown in Fig. 5a and b.[61,93,110–113] This section covers each of the various screen-printing methods used to make gas sensors to demonstrate how this objective can be accomplished. Importantly, it involves elucidating their core concepts and distinct advantages. Conventional screen printing is one of the most basic processes for making gas

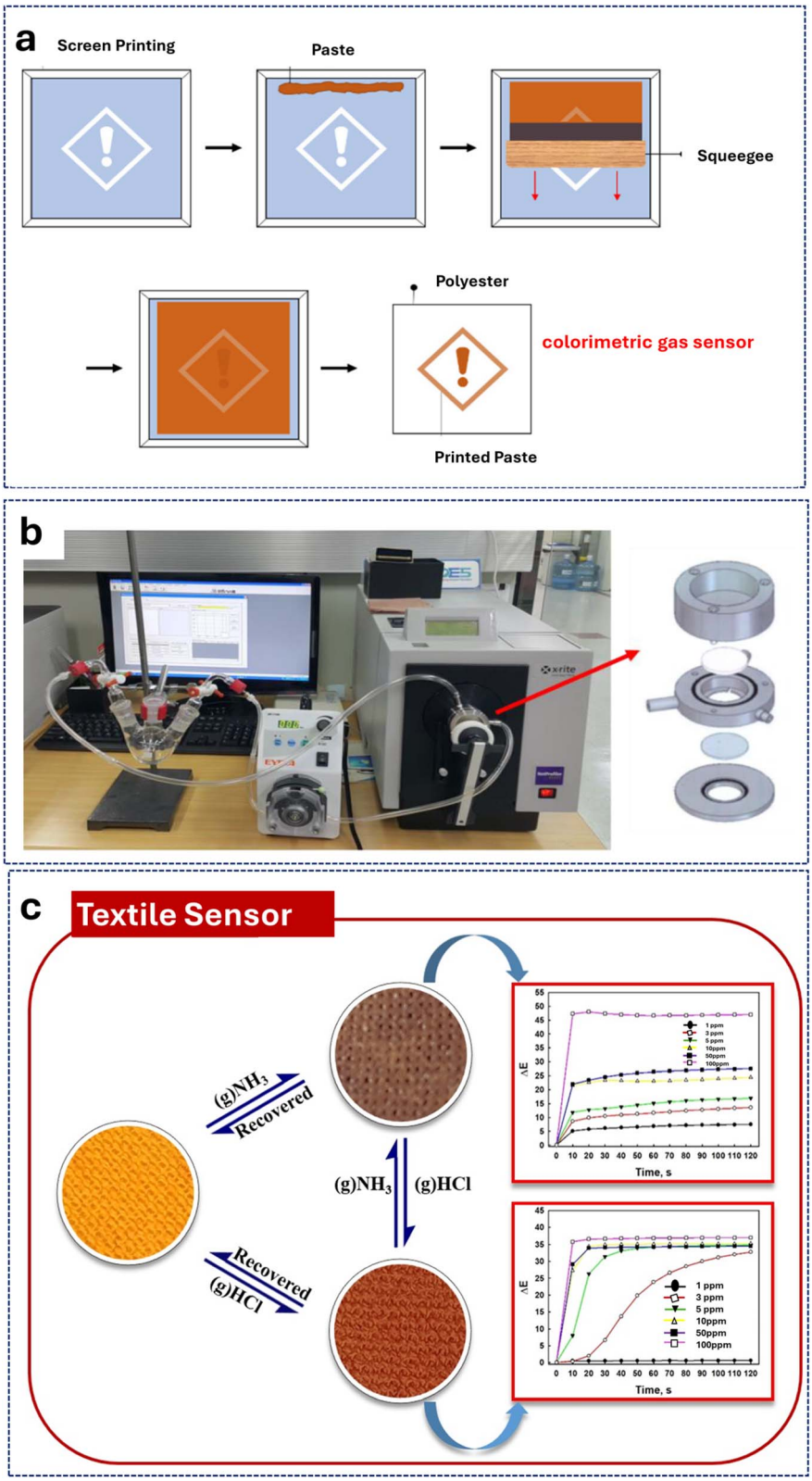

Fig. 4 Colorimetric gas sensor fabrication, setup, and dual-gas detection are illustrated. (a) the fabrication process of a colorimetric gas sensor (reprinted with permission,[109] Copyright 2020, MDPI); (b) gas sensor set-up of a colorimetric gas sensor, including a gas flow device-connected color measurement system for dynamic color change (optical picture of the entire system and chamber schematic with a loaded sample) (reprinted with permission,[109] Copyright 2020, MDPI); and (c) printing based, washable colorimetric textile sensor for the simultaneous detection of NH_3 and HCl gases at different concentrations from 1 to 100 ppm (reprinted with permission,[109] Copyright 2020, MDPI).

sensors. The procedure uses a silk screen stencil to deposit ink onto substrates. This technique is adaptable to many different types of industrial settings due to its simple equipment setup and operation, as shown in Fig. 6a–c. Some materials require a very thick film; hence, modified thick-film screen printing, which is an adaptation of conventional screen printing, uses highly viscous pastes to build up thick films of useful materials, as mentioned in Table 1, to increase the rheology of pastes.[114]

As a division of traditional screen printing, the thick-film screen printing process involves depositing conductive layers and sensing functional material layers onto substrates.[108,117] This technique uses highly viscous pastes prepared with viscosity modifiers, such as ethyl cellulose (EC) and carbitol acetate,[123] to build highly stable sensor structures for detecting different types of gases, whether volatile organic compounds (VOCs) or inorganic gases such as formaldehyde, ammonia, acetone, ethanol gas, NH_3, NO_x, and H_2S.[39,60,70,92,114,117,124,125] Moreover, the humidity sensor can be fabricated by such a technique for detecting the effect of relative humidity on sensing sensitivity by using different advanced functional materials.[57,126–130] Thick-film screen printing allows for controlling film thickness and material composition, thereby improving sensor performance and lifespan. Manufacturers can achieve consistent and repeatable thick-film deposition by fine-tuning printing parameters such as screen mesh size, squeegee pressure, and drying conditions. Due to their reliability, gas sensors made with thick-film screen printing are used in demanding and adverse operating settings.

Hybrid approaches integrating screen printing with other fabrication techniques have attracted attention in recent years.

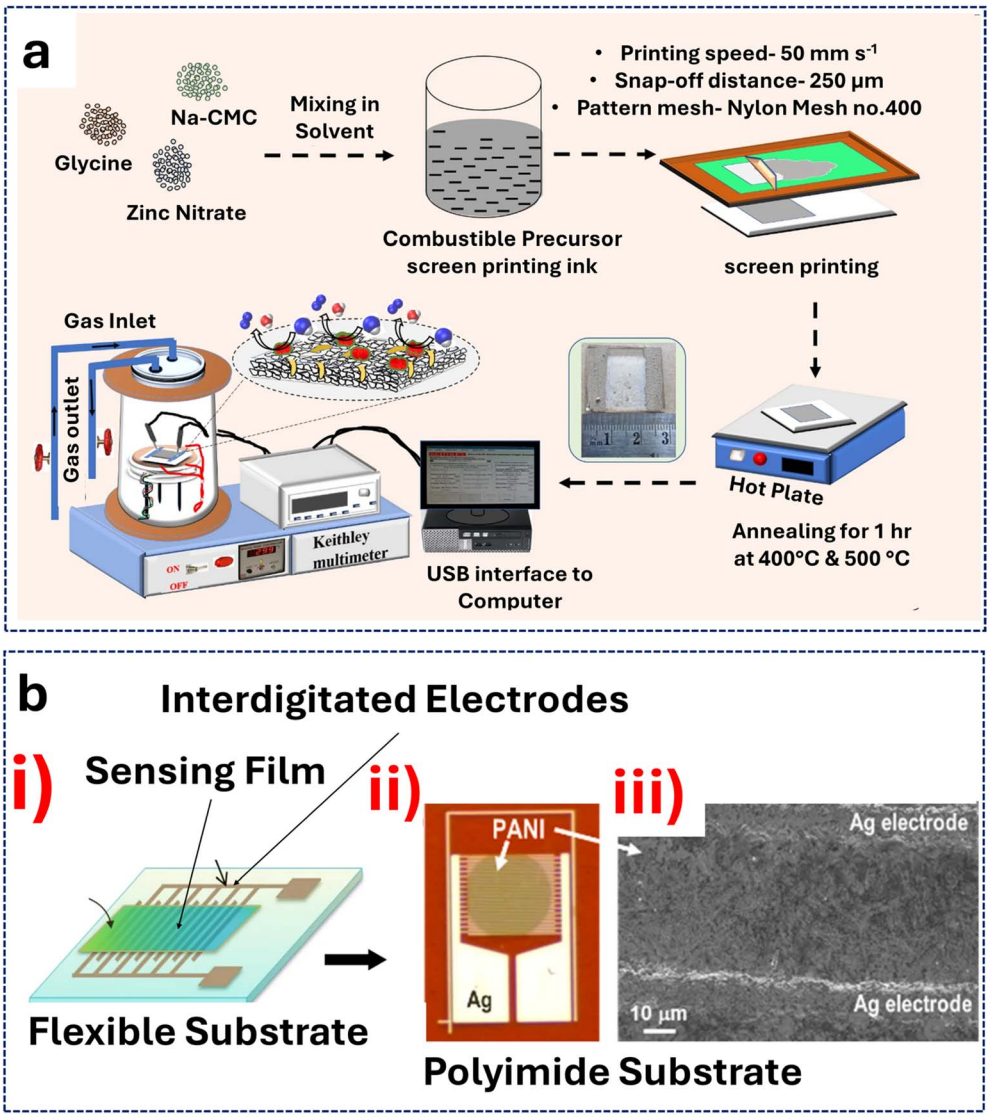

Fig. 5 Gas sensor fabrication, morphology, and ammonia detection process illustrated. (a) Diagram for sensor fabrication and gas-sensing system detection (reprinted with permission,[114] Copyright 2021, Springer Nature); and (b) IDE and sensing film morphology determined using a scanning electron microscope: (i) the schematic of the sensing film on interdigitated electrodes, (ii) the as-fabricated PANI-based NH_3 gas sensor, and (iii) the SEM image of the PANI film (reprinted with permission,[115] Copyright 2021, Springer Nature).

They offer synergistic benefits and expanded capabilities in gas sensor design and performance.[131] These approaches leverage the strengths of multiple printing technologies, such as IJP[132,133] and aerosol jet printing[134] to achieve precise patterning, enhanced resolution, and tailored material properties. By combining the versatility of screen printing with the precision of other technologies, such as laser engraving machines, manufacturers can push the boundaries of gas sensor technology, unlocking new opportunities in fields such as wearable electronics, IoT devices, and smart infrastructure.[98,102] As emerging technologies continue to be established, screen printing in gas sensor fabrication is controlled for further innovation and advancement, driving progress toward more sensitive, reliable, and cost-effective gas-sensing solutions.[131] Furthermore, this method aims to extend the lifespan and improve the performance of sensors. The cutting-edge aerosol jet printing allows for precise material patterning through aerosol deposition. This opens the door to manufacturing gas sensors with complex designs and excellent resolution. Combining the advantages of the inkjet printing technique, including drop-on-demand (DOD)[135] and continuous inkjet (CIJ) technologies, allows for improving the sensitivity and selectivity of gas sensors, as discussed by Minyawi *et al.*[55] Hence, this enables precise droplet location and material efficiency. Environmental monitoring, industrial safety, and healthcare are some of the many industries that rely on these methods for reliable gas detection. Integration of screen printing with additional fabrication processes like aerosol jet printing further demonstrates the potential for flexible sensor design and performance advancements through new methods, according to Krzemiński *et al.*[134] The gas sensor manufacturing industry is well-positioned for more advancements in screen printing thanks to emerging technologies. This will result in better sensor capabilities and a wider range of real-world applications. However, the better design of gas sensing materials needs more understanding of materials characterization and their interaction with gases and the types of charge carriers and their behaviors.

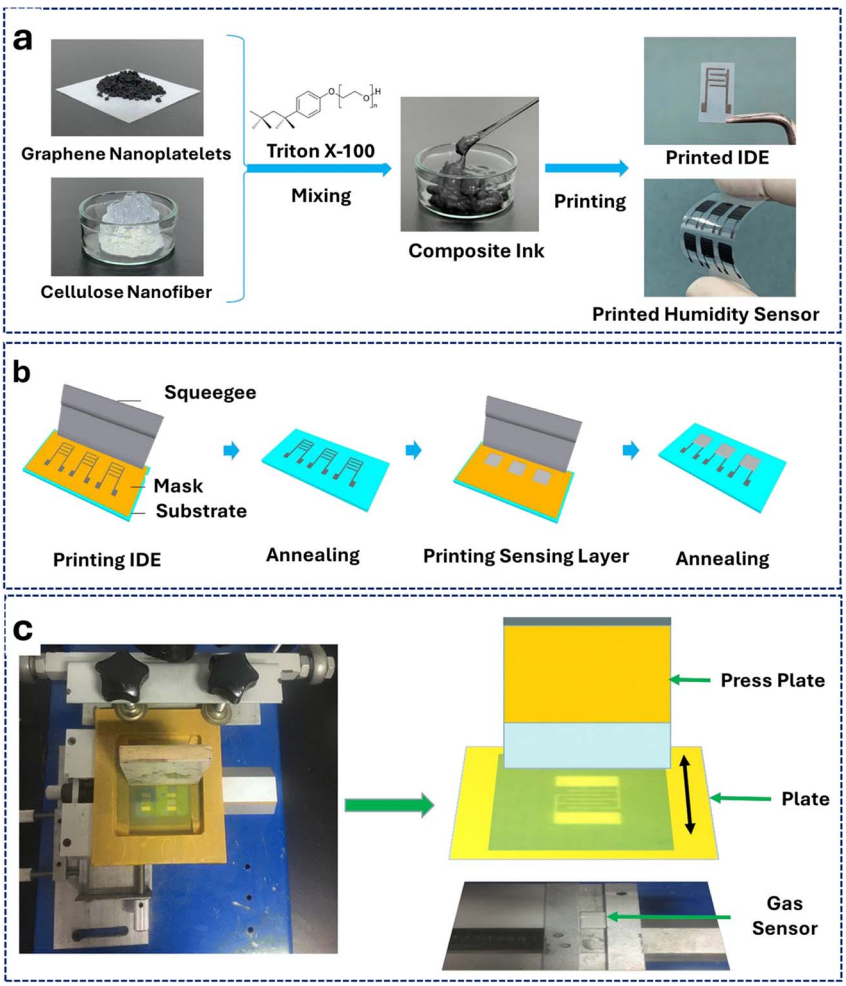

Fig. 6 Screen-printed sensors: materials preparation, fabrication, and device structure are illustrated. (a) The electrodes and sensors printed on a polyethylene naphthalate (PEN) film with CNF/GNP composite ink (reprinted with permission,[93] Copyright 2022, Elsevier); the screen printing fabrication process of the IDE and active layer. (b) Illustration of flexible humidity sensor printing (reprinted with permission,[93] Copyright 2022, Elsevier); the screen printing of gas sensors. (c) A digital photo and schematic illustration of a screen-printing device (reprinted with permission,[116] Copyright 2020, Springer Nature).

Table 1 Rheological properties of screen-printed ink

No.	Ink	Functional materials		Binder		Solvent		Ref.
		Type	Qt	Type	Qt	Type	Qt	
1	MWCNT-PEDOT:PSS	MWCNT	3 v/v%	Ethylene glycol (EG)	3.6 v/v%	DMSO Triton X-100	5.4 v/v% 0.2 v/v%	41
2	Fe_2O_3-$LaFeO_3$-La_2O_3 (Gd)	Fe_2O_3-$LaFeO_3$ La_2O_3 (Gd)	70 v/v%	Ethyl cellulose (EC)	3 v/v%	α-Terpineol	27 v/v%	117
3	CeO_x-$La_xBa_{1-x}SnO_{3-\delta}$	CeO_x-$La_xBa_{1-x}SnO_{3-\delta}$	40 wt%	Hydroxyethyl cellulose	5 wt%	Deionized water (DW)	10 mL	92
4	Zn $(NO_3)_26H_2O$	$Zn(NO_3)_26H_2O$	10 g	Glycine and Na-carboxymethyl cellulose (Na-CMC)	8 and 2 g	DW	20 mL	114
5	Zn doped In_2O_3	Zn doped In_2O_3	70%	EC	15%	Butyl carbitol acetate (BCA)	15%	36
6	PPy-MoO_3	PPy-MoO_3	70%	EC	15%	BCA	15%	118
7	SrM_2O_4 (M = Sm, La, gd, Y)	SrM_2O_4	70 w/w%	EC	1.4 w/w%	α-Terpineol	28.5 w/w%	119
8	Hydroxyapatite nanorods (HAp)/cellulose nanofibrils (CNFHAp), lead borosilicate glass	HAp and CNFHAp, lead borosilicate glass	70%	EC	15%	BCA	15%	120
9	CeO_2-Fe_2O_3 NC	CeO_2-Fe_2O_3 NC-propylene glycol	80%			Acetone	20%	121
10	SnO_2/ZnO	SnO_2/ZnO	80%	Butyl cellulose (BC) + BCA + α-terpineol			20%	122
11	SnO_2-15 wt% lead borosilicate glass	SnO_2-15 wt% lead borosilicate glass	70%	EC	15%	BCA	15%	59

3. Factors affecting the gas sensing mechanism

Assessing sensing performance involves evaluating parameters, including sensitivity, response/recovery time, stability, operating temperature, reproducibility, repeatability, and selectivity, as shown in Fig. 7. Understanding the electron transport on functional material surfaces is critical for the gas-sensing mechanism at room temperature.[136,137] Enhancing the understanding of the sensing mechanism can optimize sensor design for developing novel materials with improved sensitivity and selectivity towards specific gases. This section explains the determination of the sensing mechanism and its significance. Focusing on a specific resistance point may not provide a definitive indication of the sensor's response to target gases due to materials that can switch the mechanism from p-type to n-type, as demonstrated in a study by Bian *et al.*[138] aimed at determining the precise sensor mechanism for NO_2 gas. The type of recovery gas, whether air, H_2S, or N_2, has a potential effect on the MoS_2 sensing material and the recovery time, as discussed by Cho *et al.*[139]

To fully understand the basic functions and properties of gas-sensing materials, it is necessary to describe their gas-sensing mechanism by using advanced characterization techniques, which can help in gas sensor design.[140–142] This knowledge acquisition is critical for the logical design and advancement of gas-sensing materials with sensitivity and selectivity. Establishing the structure–function relationship, which links a material's structure, characteristics, and gas-sensing functionality, necessitates the use of complementary characterization approaches. This methodology enables the investigation of diverse properties, processes, and species conducted within a single experiment or a sequence of experiments. The accurate identification of essential elements that contribute to gas-sensing performance necessitates the differentiation between active and inactive species in the gas-sensing process.[143] The use of selective procedures and time-resolved methods has the potential to improve the accuracy and ability to identify active species.[144] This section discusses important material characterization techniques, which can provide detailed information about the sensing mechanism, including surface area, Hall effect, and temperature-programmed desorption (TPD)/oxidation (TPO)/reduction (TPR) approaches as summarized in Fig. 8 to explain the gas sensing mechanism.

3.1. Surface area

Increasing the effective surface area of the sensing material, such as ZnO/CdO, SnS_2/TiO_2, MOFs, WO_3, and SnO_2, can enhance gas sensing qualities, such as sensitivity and response/recovery time.[145–147] The increase in the surface area leads to a larger number of active sites available for gas adsorption and interaction, resulting in improved sensor performance. Xie *et al.*[145] proved that the porosity and high specific surface area of MOFs-SnO_2/NiO for detecting CO gas, which has more active sites and channels, enhanced due to the favorable behavior of gases for adsorption and transportation. Xu *et al.*[148] obtained the same evidence by studying how the surface area affects the performance of SnS_2-M microsheets for detecting NO_2.

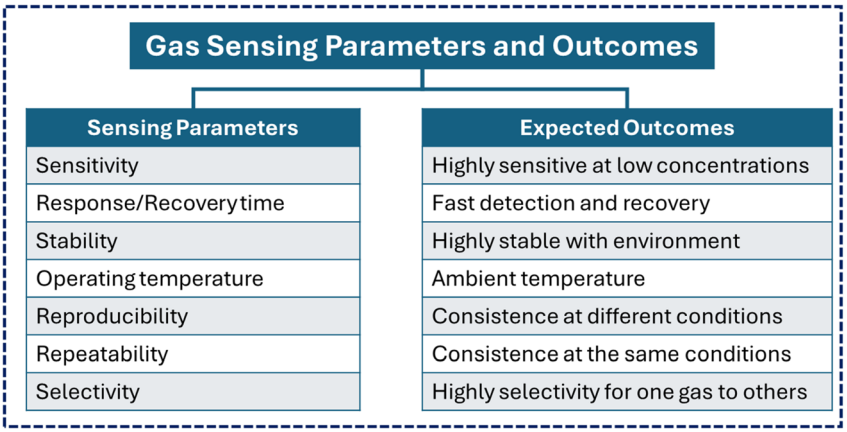

Fig. 7 Schematic diagram of gas sensing parameters and expected outcomes.

Different behaviors of p-type Zn-doped α-Fe_2O_3 nanoparticles were studied by Du *et al.*[149] They found that Zn doping in α-Fe_2O_3 can enhance the sensor performance, even though with a reduced surface area. The increased oxygen vacancy defects for detecting xylene gas, which are responsible for reducing resistance and bandgap, explain the improved sensor performance. Therefore, porous structures, such as ZnO nanosheets@In_2O_3 hollow micro-rods, which can be used for

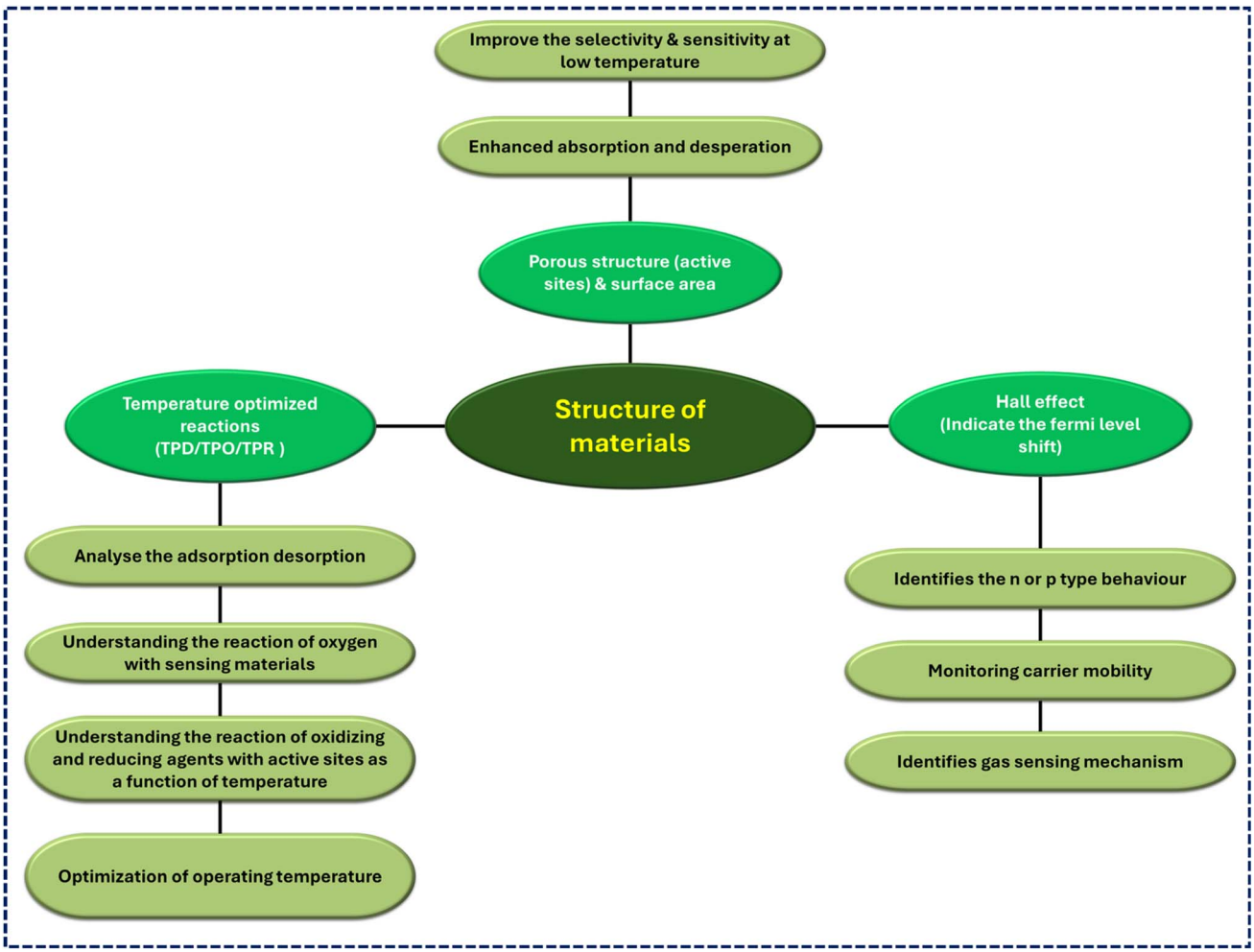

Fig. 8 A schematic diagram presents important parameters for understanding materials structures and gas sensing mechanisms, including surface area, Hall effect, and temperature-optimized reactions (TPD/TPO/TPR).

detecting C_2H_5OH with a large surface area, can provide a significant contact area for gas-sensing materials to interact with target gases.[150] Hence, a larger effective surface area demonstrated enhanced gas sensing properties, including increased sensitivity and response/recovery time, compared to those with a smaller surface area.[140,144,151–153]

3.2. Hall effect

The Hall effect provides valuable information about n-type or p-type semiconducting materials, which can be used as a gas sensing layer. Therefore, this technique can detect changes in the electron concentration and mobility of charge carriers when exposed to 50 °C, as discussed by Chauhan *et al.*[154] to detect the V_2O_5-noble metal (Au, Ag, and Pd) nanocomposite. At the n-to-p transition point of 47 °C, the Hall coefficient R_H was negative below 47 °C, indicating n-type behavior. Conversely, a Hall coefficient R_H above this temperature was positive, indicating p-type behavior. This behavior is unique and switches the gas sensor response because of the n-type to p-type transition and *vice versa*, as shown by Sharma *et al.*[155] and Kumar Gangwar *et al.*[141]

On the other hand, Bian *et al.*[138] studied a complex problem, including the performance of p-type-like pristine WO_3 named De-WO_3 towards NO_2 gas molecules, as they expected resistance to decrease as a behavior of p-type materials. However, the Hall effect proves that the Hall coefficient is negative, meaning that the n-type performance is responsible for conductivity change. To address this issue, the NO_2 adsorption on WO_3 oxidized the surface, filling the oxygen vacancy and releasing NO gas. As a result, NO is adsorbed on WO_3, resulting in charge transfer from NO molecules to WO_3, improving its n-doping behavior. Consequently, the Fermi level of the WO_3 surface moves towards the conduction band, making it more n-type. Similar to DE-WO_3, carbon dots–WO_3 (C dots–WO_3) heterostructure sensors exposed to NO_2 have lower resistance, and the DE-WO_3 surface vacancies may improve sensor response. This result suggests an expected mechanism, whether the sensor exhibits n- or p-type behavior, depending on the increasing or decreasing resistance of the sensor in the presence of the electron-accepting NO_2 gas.

Hence, the Hall effect measurement provides valuable insights into the relationship between the structure, temperature, and function of the sensing material. This is critical for directly revealing the n- or p-type conductivity of the sensing materials and enhancing gas sensing performance.[156–159]

3.3. TPD, TPO, and TPR analysis

Temperature-programmed desorption (TPD)/oxidation (TPO)/reduction (TPR) approaches have the potential to provide significant insights into gas sensing mechanisms under optimized pressure and decomposition temperature of the materials.[42,161] More understanding of adsorbed oxygen and oxygen vacancies was obtained by Ciftyurek *et al.*,[161] who showcased the sensing mechanism intending to design gas sensing materials to improve the sensing performance. The process of adsorbed oxygen being consumed, transported, and undergoing adsorption/desorption is essential for understanding how it interacts with sensing materials, whether it is physisorbed through van der Waals bonds or chemisorption through chemical interactions. Therefore, O_2-TPD and TPO can give a better understanding of the interactions of oxygen with the sensing materials and the amount of consumed gas at specific temperatures. Absorbed gas molecules on a solid surface can acquire an electrical charge through electron exchange, a process known as ionosorption. Additionally, these gas molecules can dissociate into either charged or uncharged atomic species, a phenomenon known as dissociative chemisorption. When solid surfaces come into contact with oxygen, the gas is typically adsorbed, resulting in the formation of several uncharged (O_2 and O) and charged (O_2^-, O^-, and O^{2-}) species.[160]

Moreover, TPO and TPR with specific oxidizing and reducing gases, respectively, evaluate the oxidative and reducible active sites on the surface and determine the consumption of the gases as a function of temperature. Addressing the gas sensing mechanism, O_2-TPD and H_2-TPR were studied by Yang *et al.*[162] They found that indium doping of SnO_2 enhanced the adsorbing oxygen area and active sites and lowered the reduction temperature. Therefore, TPD, TPO, and TPR analysis can shed light on the desorption and reduction properties of adsorbed gas species and sensing gas, which can give preliminary valuable information about the sensing performance with temperature optimization.[142,143,163] These methodologies facilitate the formation of structure–function links, a crucial aspect in the rational design of gas-sensing materials. This leads to improved gas sensor performance.[164,165]

4. Gas sensing performance of different gases

To ensure the safety of industries, humans, and the environment, gas sensors are essential for detecting a wide range of gases, such as oxygen (O_2), chlorine (Cl_2), hydrogen chloride (HCl), ammonia (NH_3), nitrogen dioxide (NO_2), carbon monoxide (CO), sulfur dioxide (SO_2), hydrogen (H_2), low-molecular-weight polar gases, and VOCs, as shown in Fig. 9.[42,69,71,90,112,113,126,166–169] The development of specialized sensors that can detect a small concentration of gases with high sensitivity and selectivity is necessary because each gas has its own unique set of problems and hazards. When it comes to tracking industrial emissions and urban air quality, NO_2 sensors are indispensable, but for measuring interior air quality and attempts to combat climate change, CO_2 and O_2 sensors are crucial.[37,69] CO detectors are essential for preventing silent killer poisoning, particularly in residential and occupational settings.[170,171] This section will present the sensing mechanisms of different gases and the advanced materials that perform well for sensing selective gases. Hence, for better evaluation of the sensing mechanism, we have first categorized the harmful gases into two groups: oxidizing gases, including O_2, CO_2, F_2, NO_2, SO_2, O_3, and Cl_2, and reducing gases, like CO, H_2, NH_3, H_2S, NO, and VOCs.[172]

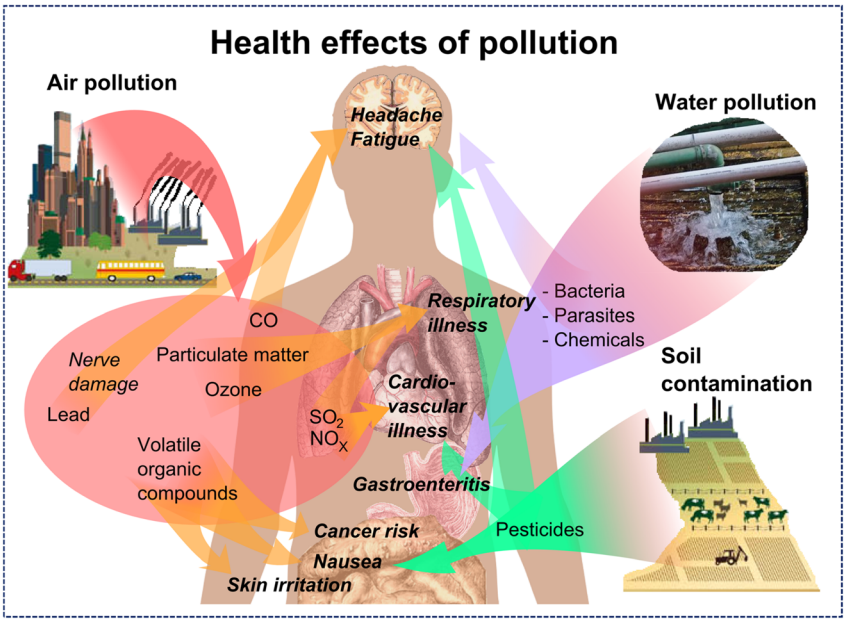

Fig. 9 Major impacts of environmental pollution on human health (reprinted with permission,[173] Copyright 2014, *WikiJournal of Medicine*).

SO_2 sensors are valuable tools for monitoring pollution levels and industrial emissions. H_2 and H_2S safety sensors are necessary for many industrial fields to detect leaks, as these types of gases can lead to invisible fire and death at high levels, respectively. The use of NH_3 sensors is vital in agricultural applications such as fertilizer production and for tracking the use of fertilizers and emissions from livestock.[170] LPG and CH_4 sensors are important for petrochemical and natural gas companies to identify potentially explosive gases during industrial operations.[170,174] This is why NH_3, CO, O_2, and VOC sensors, such as acetone, C_2H_5OH, and C_4F_7N, are crucial for protecting the environment and monitoring indoor air quality. Public health, environmental sustainability, and industrial safety are all aided by gas detection devices for these gases.[98] For evaluating the performance of chemiresistive gas sensors, the electrical resistance of sensors in the air (R_a) and the presence of gas (R_g) were measured to evaluate the gas sensitivity (S) and response/recovery times. The different gas setups as shown in Fig. 10–12 can be used to measure the performance of gas sensors.[70,170,175,176]

The gas response (S%) is calculated using the following eqn (1) and (2).[69]

$$\text{Oxidizing gases } S = \frac{R_g - R_a}{R_a} \times 100\% \quad (1)$$

$$\text{Reducing gases } S = \frac{R_a - R_g}{R_a} \times 100\% \quad (2)$$

The response/recovery times can be calculated using eqn (3) and (4).[178]

$$\text{Response time } (T_{90}) = T_2 - T_1 \quad (3)$$

$$\text{Recovery time } (D_{10}) = T_4 - T_3 \quad (4)$$

The response time is the speed of response, which refers to the duration it takes for a sensor to achieve 90% of the entire response of a signal when exposed to a specific gas.[178] The recovery time is the duration necessary for a sensor to come back to 90% of its initial baseline signal after the elimination of the target gas.[179,180] The above characterization results, including surface area, Hall effect, and temperature programming (TPD, TPO, and TPR), as mentioned in Section 3, opens the door to a better understanding of the gas sensing mechanism for different types of gases, such as NO_2, CO, CO_2, SO_2, H_2, H_2S, NH_3, LPG, CH_3, and VOCs.

4.1. Nitrogen dioxide (NO_2)

Combustion activities, particularly those in the transportation and manufacturing sectors, are the primary contributors to the emissions of NO_2, which is a highly reactive gas.[69] Thermal power plants, pulp mills, and cars generate nitrous oxide (NO_x) gas, which causes a range of environmental problems, such as acid rain, photochemical smog, and ground-level ozone. NO_x is a gas that possesses corrosive properties and can induce physiological irritation. This is why prolonged exposure to NO_x can lead to respiratory tract infections and lung illnesses. Hence, the detection of this gas using high-performance sensors holds significant importance. The inhalation of NO_2 can either cause asthma or make it worse, as well as trigger other respiratory disorders.[36]

Researchers have developed various sensor technologies to detect NO_2 gas. These include electrochemical sensors, polymer sensors, surface acoustic wave sensors, and metal oxide semiconductor (MOS) sensors.[56] Electrochemical cells or MOSs as chemiresistive sensors are some of the components frequently found in gas sensors to detect NO_2.[37] These NO_2 sensors are very

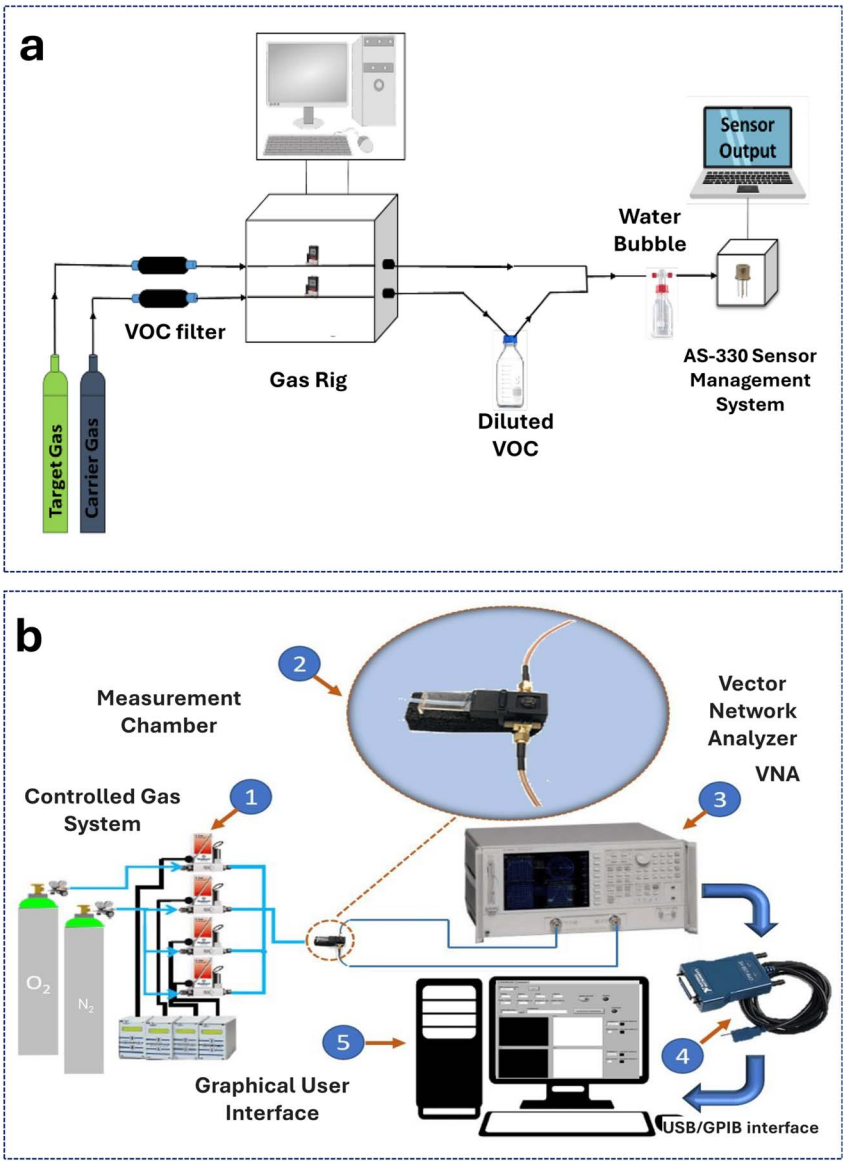

Fig. 10 VOC and oxygen gas sensor setups with detailed system components. (a) The diagram shows the target and carrier gas, VOC filter, gas rig, diluted VOC trap, water bubble for humidity, AS-330 sensor management system, and sensor output (reprinted with permission,[167] Copyright 2021, MDPI); schematic diagram of the oxygen gas sensor and (b) the set-up has five key parts: the controlled gas system, measuring chamber, vector network analyzer (VNA), USB/GPIB interface, and graphical user interface for oxygen monitoring (GPIB) (reprinted with permission,[166] Copyright 2020, MDPI).

sensitive and selective, making them an excellent choice for monitoring the quality of the air inside buildings, factories, and other industrial environments.[181]

The gas sensing mechanism of NO_2 can be elucidated by considering the chemical interaction between target gas molecules and the surface of metal oxides during the adsorption process, as shown in the gas setup in Fig. 13a–c. Adsorption processes can be classified into two categories: physisorption and chemisorption. Physisorption involves the participation of weak van der Waals forces in contact, while chemisorption entails the formation of chemical bonds between the metal oxide surface (adsorbent) and gas molecules (adsorbate) because of charge transfer.[181]

The sensing capabilities of metal oxide gas sensors primarily rely on the rate at which oxygen is adsorbed and desorbed. NO_x exhibits a high degree of oxidation and possesses a notable electrophilic characteristic. As discussed by Cheng *et al.*,[181] the reactivity of NO_x is higher when it comes to oxygen vacancies present on the surface of metal oxides; they found that the vacancies in NiO-Ni_v can promote the sensitivity of nickel oxide towards NO_2 as an oxidizing gas because of the high concentration of holes and reduce the resistance, as shown in Fig. 13a. This sensor showed a response of 12.42 at 20 parts per million (ppm) of NO_2 gas, which is 7.8 times greater than that of pure NiO. Moreover, it demonstrated a significant level of selectivity and stability towards NO_2 gas, with lifetime stability extended to a month.

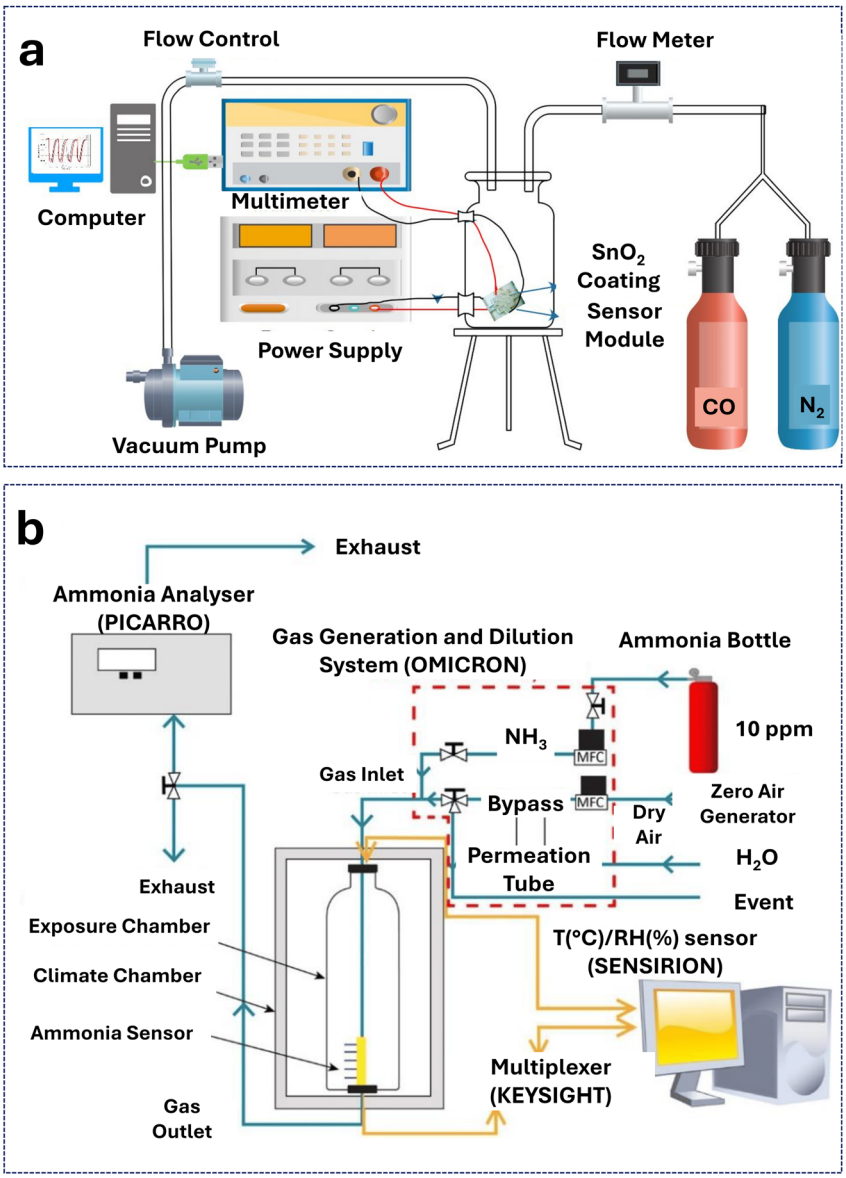

Fig. 11 CO and ammonia gas sensing setups with detailed experimental configurations. (a) schematic of the CO gas sensing system attached with a vacuum pump, multimeter, and power supply (reprinted with permission,[168] Copyright 2020, Wiley); (b) a schematic diagram of the gas sensing set-up of the ammonia sensor, featuring a three-electrode sensor measuring system composed of a gas chamber, MFCs, gas generation, and dilution system (OMICRON), ammonia bottle, Keysight electrical resistant measurements, and temperature and humidity testing device (reprinted with permission,[126] Copyright 2021, MDPI).

According to R. Sivakumar *et al.*,[37] the combination of semiconducting metal oxides with carbonaceous materials showed an effective performance towards the detection of NO_2 and CO_2, as shown in Fig. 13b. They synthesized size-controlled SnO_2 nanoparticles (NPs) decorated with reduced graphene oxide (rGO) as hybrid sensors using a hydrothermal approach. For a better understanding of the physicochemical structure of SO_2/rGO, X-ray Diffraction (XRD), Scanning Electron Microscopy (SEM), Transmission Electron Microscopy (TEM), Brunauer–Emmett–Teller (BET) Surface Area Analysis, and X-ray Photoelectron Spectroscopy (XPS) analysis techniques were used for a full investigation. By adjusting the concentration of rGO in SnO_2 within the range of 0 to 5 wt%, they tested a set of gas sensors with resistance properties, utilizing a combination of the composite SnO_2/rGO and pure SnO_2. The composite sensor demonstrated high capabilities for sensing NO_2 gas with a high response (88.9), selectivity, repeatability, fast response time (12 s), and quick recovery time (34 s).

Another material, such as n-type Pd-V_2O_5, which was discussed by Birajdar *et al.*,[69] facilitates the rapid adsorption of gas on the surface of metal oxides, as shown in Fig. 13c. As the temperature increases, the intrinsic conductance of Pd-V_2O_5 likewise increases.[69] The sensing results of 1 wt% Pd@V_2O_5 exhibited a high response and selectivity towards NO_x gas, including a mixture of NO and NO_2, compared to other gases such as SO_x, NH_3, CH_3OH, C_2H_5OH, acetone, trimethylamine,

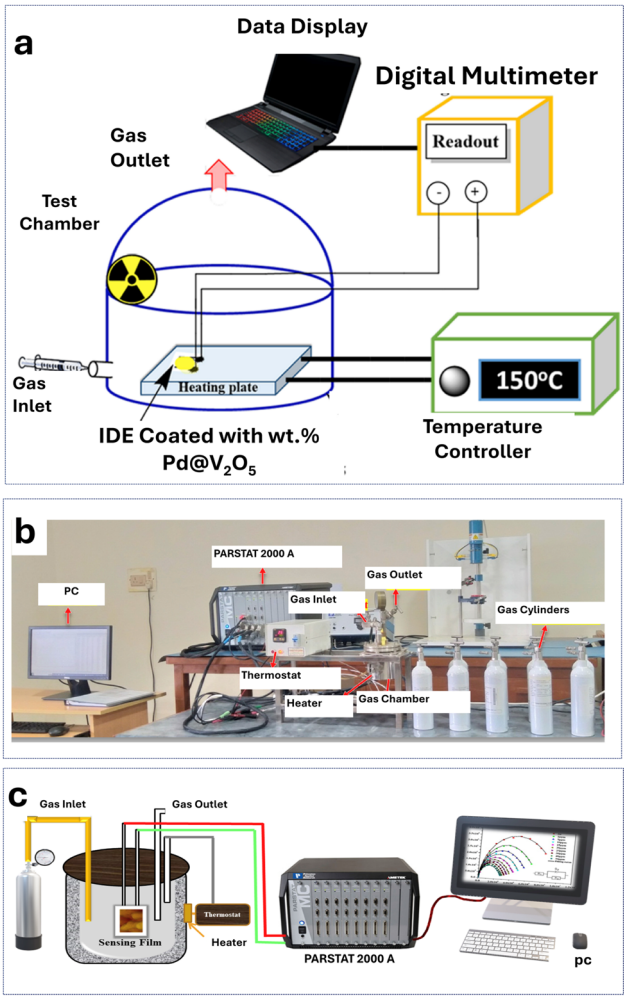

Fig. 12 IDE-based gas sensors and H_2S detection setups are comprehensively illustrated. Gas-detecting assembly schematic diagram: (a) interdigitated electrode (IDE) gas sensor with the heating unit and digital multimeter (reprinted with permission,[177] Copyright 2020, Elsevier); (b) gas sensing setup photo of the full system, featuring the system composed of a potentiostat PARSTA 2000A, PC, thermostat, heater, gas inlet, gas outlet, gas cylinders, and gas chambers (reprinted with permission,[90] Copyright 2024, Elsevier); (c) the schematic diagram of the gas sensor setup showing the full system and sensing film of the H_2S gas sensor (reprinted with permission,[90] Copyright 2024, Elsevier).

triethylamine, and formaldehyde. The sensing performance was evaluated at various temperatures, including 30, 100, and 150 °C in the range of 10 to 1000 ppm. At 150 °C, the sensing performance was high, with a short response time (about 0.53 s) and recovery time (1.5 s) at 10 ppm. While the response time for other concentrations till 100 ppm was 1 s, the recovery time was in the range of 1.5 to 100 s. The mechanism involves the initial adsorption of oxygen molecules onto the surface of Pd-V_2O_5, resulting in the formation of various ions such as O^-, O_2^-, and O^{2-}, as shown in Fig. 12a. This adsorption process occurred by removing electrons from the Pd-V_2O_5 surface and was influenced by operating temperature, as shown in eqn (5).

$$O_{2(gas)} + 2e^- \rightarrow 2O_{(ads.)}^- \quad T = 150\ ^\circ C \tag{5}$$

The surface electron concentration decreased as electrons transferred to chemisorbed oxygen, creating an electron depletion layer. This created a potential barrier at the boundary of the sensor, impeding electron flow. Surface states, including donor and acceptor states, exist above the valence band and below the Fermi level.

The exposure of NO_x gas to the Pd-V_2O_5 surface resulted in the efficient adsorption of the gas by the active sites of the Pd-V_2O_5 surface, leading to the capture of electrons from the surface, as shown in eqn (6)–(8).[69]

$$NO_{x(gas)} + e^- \xrightarrow{150\ ^\circ C} NO_{X(ads.)}^- \tag{6}$$

$$NO_{x(gas)} + O_{(ads.)}^- + 2e^- \xrightarrow{150\ ^\circ C} NO_{X(ads.)}^- + 2O_{(ads.)}^- \tag{7}$$

$$NO_{x(gas)} + O_{(ads.)}^- + 2e^- \xrightarrow{150\ ^\circ C} NO_{X(ads.)}^- + 2O_{(ads.)}^{2-} \tag{8}$$

Furthermore, SnO_2@$Ti_3C_2T_x$ MXene was synthesized using a flexible solvothermal technique in the work of Liu *et al.*[151] The composite exhibited remarkable sensitivity and selectivity toward NO_2 at ambient temperature because it enhanced conductivity toward 300 ppm NO_2 by more than 20 times compared to pure $Ti_3C_2T_x$ MXene. Nitrogen adsorption–desorption isotherm analysis and DFT calculations were used to investigate the sensing mechanism toward NO_2. The large specific surface area, well-balanced heterogeneous structure, and ionic interactions generated between the substrate and NO_2 gas (Sn–N and O–N) demonstrated a positive impact on enhancing the gas reaction capabilities.

To report one of the key challenges for fabricating highly selective chemiresistive-type gas sensors working at room temperature, Ogbeide *et al.*[184] suggested combining rGO with a binary metal oxide $CuCoO_x$ as a sensing material, demonstrating highly stable NO_2 sensors at room temperature with a detection limit of 50 ppb using an IJP technique. To capitalize on these unique results, they then created a framework to facilitate machine-intelligent detection with clear visibility, recognizing specific gases and forecasting their concentration using a single sensor with a good interfering atmosphere. The machine learning-based classifier utilized 10 distinct parameters derived from the sensor response to establish a decision boundary with an accuracy of 98.1%. In addition to that, it is capable of accurately predicting NO_2 and humidity concentrations in an environment with interfering factors, even when these concentrations have not been observed before. This method enables the printing and use of a smart gas sensor system at room temperature. Regardless of the humidity level, it can function in a variety of environments.

4.2. Carbon monoxide (CO)

The insufficient combustion of carbon-containing fuels results in the production of CO, a gas that is odorless and colorless, which is identified as a silent killer.[6] CO poisoning, which can be fatal if it is not detected promptly, can be caused by a long

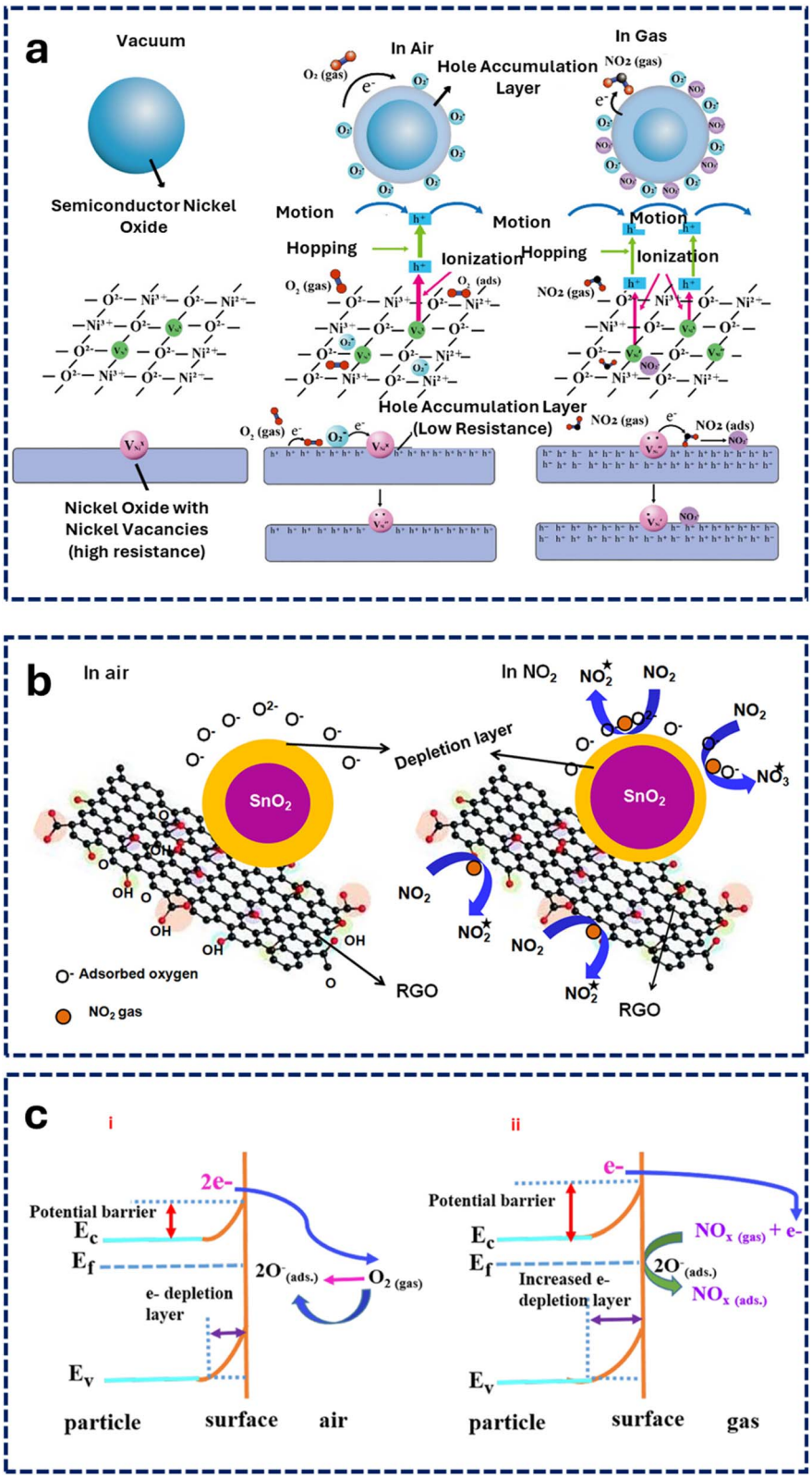

Fig. 13 Gas sensing mechanisms: NiO, SnO_2/RGO, and Pd@V_2O_5 sensor diagram. (a) NiO-Ni_v sensor system in a vacuum, air, and NO_2 at room temperature (RT) (reprinted with permission,[182] Copyright 2024, American Chemical Society); (b) gas sensing mechanism diagram of the SnO_2/RGO sensor for NO_2 gas (reprinted with permission,[183] Copyright 2021, Elsevier); (c) schematic representation of the sensing mechanism of 1 wt% Pd@V_2O_5 towards (i) air and (ii) NO_x (reprinted with permission,[177] Copyright 2020, Elsevier).

exposure time or high concentration level.[71] Gas sensors, such as electrochemical, chemiresistive, and optical sensors, can detect CO using a gas setup, as shown in Fig. 11a. These sensors are highly sensitive to low quantities of CO and have a fast response time, making them vital components for safety applications in many places.

SnO_2 nanoparticles, as described by Taulo *et al.*,[42] which are n-type metal–oxide semiconductors, may detect gases by using electron transfer between the nanoparticles, chemisorbed oxygen species, and target gases. Fig. 14a presents the gas sensing setup for detecting the above toxic gas by using an interdigitated electrode (IDE) with a small size and space gap between fingers. This can achieve high performance due to the high precision and avoidance of overlapping the performance of sensing materials and the transducer conductive layer compared to a single electrode system. Additionally, by optimizing the IJP conditions, they improved the CO gas sensing performance of printed sensors. At a concentration of 200 ppm, the sensor consisting of 10 printed layers demonstrated a sensitivity of approximately 20%, while the sensors with 5, 15, and 20 printed layers exhibited a sensitivity of no more than 14% each. Due to the presence of uniform layers, the printed sensors demonstrated nearly twice the sensitivity compared to identical sensors created using the drop-casting method. To determine the sensing mechanism, they used high temperatures and the presence of air, in which oxygen molecules underwent chemisorption on the surface of SnO_2 and had the capability to acquire electrons from the conduction band, resulting in the conversion of these electrons into anionic oxygen species (O^{2-}, O^{-}, and O_2^{-}), as shown in eqn (9)–(11). Electron capture caused a depletion layer to form on the surface of the nanoparticles, increasing the potential barrier height between them, as shown in Fig. 14b. This is why the sensors exhibited high resistance.

$$O_{2(gas)} \leftrightarrow O_{2(ads.)} \quad (9)$$

$$O_{2(ads.)} + e^{-} \rightarrow O_{2(ads.)}^{-} \quad (T < 100\ ^{\circ}C) \quad (10)$$

$$O_{(ads.)}^{-} + e^{-} \rightarrow O_{(ads.)}^{2-} \quad (T > 300\ ^{\circ}C) \quad (11)$$

Upon the introduction of CO gas, it underwent oxidation to CO_2 through a reaction with oxygen species. Consequently, the trapped electrons were subsequently released into the conduction band, resulting in the narrowing of the depletion layer, as shown in eqn (12). The detected sensor signal results from a drop in resistance due to a reduction in the potential barrier height between the nanoparticles.

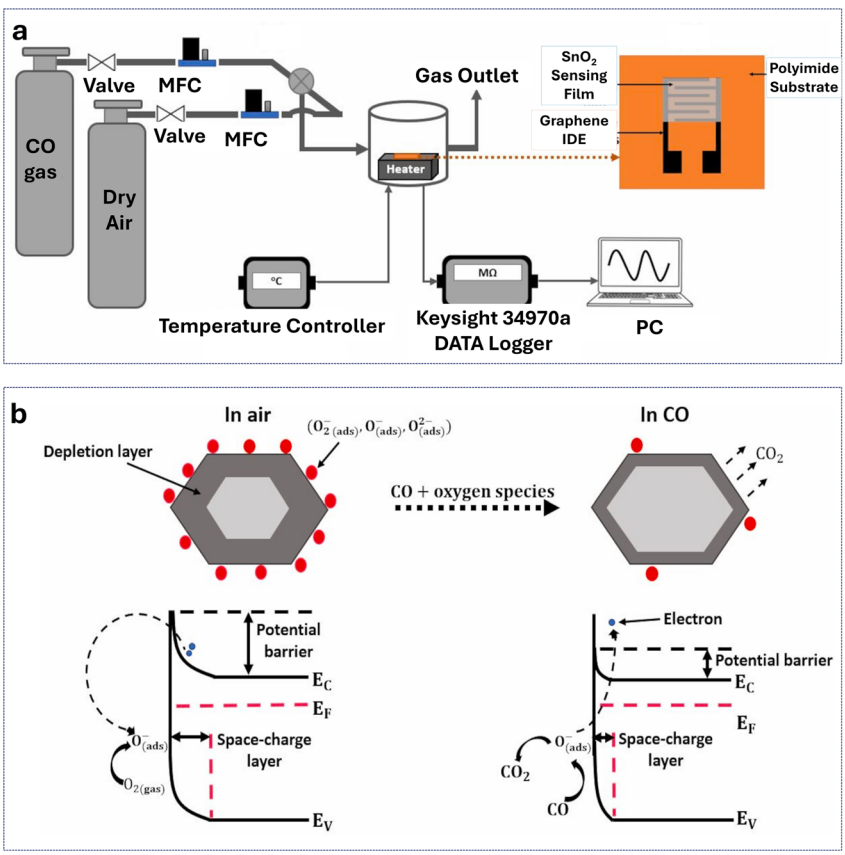

Fig. 14 CO gas detection: printed sensor design and SnO_2 interaction mechanism. Gas detection system: (a) a schematic with a heating unit and sensor design of the printed CO gas sensor (reprinted with permission,[42] Copyright 2024, Elsevier). (b) Schematic illustration of the CO gas sensing mechanism, showing the SnO_2 interaction with CO and air; E_F, E_c, and E_v are the Fermi level, conduction band, and valence band energies (reprinted with permission,[42] Copyright 2024, Elsevier).

$$CO_{(gas)} + O_{(ads.)}^{-} \rightarrow CO_2 + e^{-} \quad (100\ ^{\circ}C < T < 300\ ^{\circ}C) \quad (12)$$

Moreover, one of the good examples of sensing CO is the work of Xie *et al.*[145] They modified SnO_2 to alter metal–organic skeleton-derived NiO using a hydrothermal technique. This composite exhibited a good performance toward CO gas at room temperature due to the high surface area and heterojunction structure. The sensor demonstrated a high response value for CO gas sensing of 5.48 at 100 ppm, a low detection limit of around 1 ppm CO gas, and fast response and recovery times of 56 and 4 s at 100 ppm CO gas, respectively. The high-performance detection of CO gas was achieved using the porous structure and large specific surface area of MOF-derived NiO, as well as the production of a NiO/SnO_2 heterojunction.

4.3. Carbon dioxide (CO_2)

Combustion processes, human activities, and natural sources all contribute to the creation of CO_2 gas. Monitoring CO_2 levels is vital for evaluating the quality of the air inside buildings, the efficiency of ventilation systems, and the effectiveness of initiatives to mitigate climate change. A technology known as non-dispersive infrared (NDIR) or solid-state sensors that are based on metal oxides or carbon nanotubes (CNTs) is generally utilized by gas sensors to detect CO_2. In addition to providing real-time monitoring capabilities, these sensors have applications in a variety of settings, including environmental monitoring networks, automotive systems, and architectures.[185]

Karthik *et al.*[186] found that ZnO, which is one of the n-type metal oxides, has a high sensitivity towards CO_2 gas as the operating temperature reached around 300 °C, and the vacancy sites on the ZnO surface became susceptible to adsorption by ambient oxygen, as shown in eqn (13) and (14). This means that CO_2 reacted with the adsorbed oxygen, creating carbonate compounds like $(CO_3)^{2-}$, as shown in Fig. 15. In turn, this caused the resistance to rise, as CO_2 is an oxidizing gas that subtracts electrons from n-type metal oxides. Hence, the production of CO_2 gas detectors at low temperatures remains a challenge, but Zito *et al.*[187] used a yolk–shell ceria nanosphere to solve this issue at 100 °C.

$$CO_{2(gas)} + O_{(ads.)}^{2-} \rightarrow (CO_3)_{(ads.)}^{2-}$$
interaction with adsorbed oxygen (13)

$$(CO_3)_{(ads.)}^{2-} \rightarrow CO_{2(gas)} + \frac{1}{2}O_{2(gas)}$$
desportion at 300 °C (14)

Le Pennec *et al.*[188] reported the detection of CO_2 using a drop-cast and screen-printed barium titanate sensor. The implemented sensors were evaluated under the conditions of dry and humid air (20–50–70%) with CO_2 gas ranging from 100 ppm to 5000 ppm at 280 °C. Furthermore, the sensor showed a high response at low levels of humidity. The $BaTiO_3$ sensors exhibited excellent repeatability with CO_2 over other gases, including SO_2, NO_2, and CO. The sensors created through screen printing exhibited response and recovery times of 2.5 min and 6 min, respectively, while the sensors fabricated using drop-casting showed response and recovery times of 2 min and 4 min, respectively. The sensor developed with the drop-casting

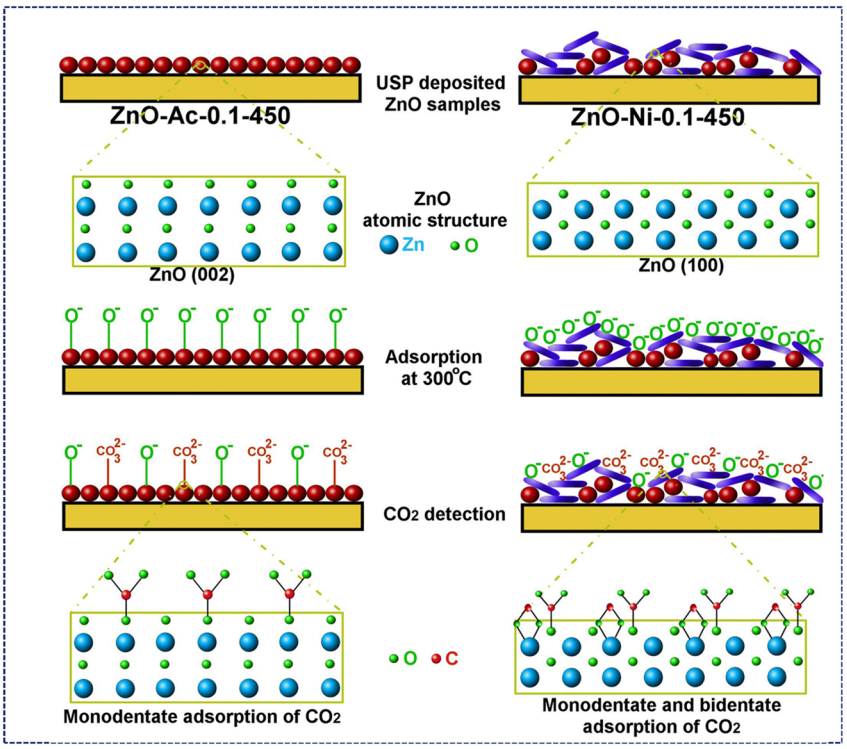

Fig. 15 CO_2 sensing on ZnO surfaces: zinc acetate *vs.* nitrate precursors. CO_2 gas sensing mechanism on the ZnO surfaces prepared with zinc acetate (left side) and zinc nitrate (left side) as precursors (reprinted with permission,[186] Copyright 2020, Springer Nature).

technique demonstrated a marginal improvement in the efficiency of the CO_2 gas detection because of the improved regulation of the uniformity of the sensitive layer's thickness.

Escobedo *et al.* developed good smart sensors designed in the shape of facemasks to prevent SARS-CoV-2 transmission effectively.[189] Moreover, there is evidence supporting the use of facemasks to decrease the spread of infections within a community. However, there is also consensus regarding the potential negative consequences of wearing them for extended periods. These consequences primarily arise from CO_2 inhalation–exhalation and then re-inhaling. In their study, they introduced a detection system that accurately measured CO_2 levels in real-time within FFP2 facemasks. The device comprised an opto-chemical sensor integrated with a flexible, battery-free, near-field-enabled tag with a resolution and detection limit of 103 and 140 ppm, respectively. The sensor had a lifetime of 8 hours, which is similar to the suggested usage period of FFP2 facemasks. They offered smartphone applications enabling wireless power, data analysis, alarms, and measurement. By conducting performance tests during daily activity and tracking exercises, they showcased the effectiveness of this technology as non-invasive.

Awandkar *et al.*[190] synthesized polyaniline-stannous chloride pentahydrate (PSCL) composites to sense CO_2 gas at ambient temperature in an environment containing 150 ppm of this gas. The composites were screen-printed over a glass substrate. The composites had response times of 130, 142, 134, and 113 s, and recovery times of 31, 556, 98, and 90 s or PSCL concentrations of 5%, 10%, 15%, and 20%, respectively. Under ambient conditions, PSCL 15% exhibited enhanced sensitivity towards CO_2 gas with a high degree of repeatability and sensitivity because of the electrons moving across the p–n junction generated and the concentration of the precursor.

4.4. Sulfur dioxide (SO_2)

Burning sulfur-containing fuels in many industrial operations, such as the melting of metals and the production of electricity, generates SO_2. The inhalation of SO_2 can lead to respiratory issues and contribute to the creation of acid rain and air pollution. In most cases, metal oxides or electrochemical cells are utilized as sensing elements in gas sensors to detect SO_2.[69] Because of their great sensitivity and selectivity to sulfur dioxide, these sensors allow monitoring of the quality of the air in the surrounding environment and industrial emissions.

As mentioned by Zhou *et al.*,[191] the chemisorption process significantly changed the electrical characteristics, specifically the resistance, of gas sensors based on metal oxides. The insertion of NiO into the ZnO matrix led to the creation of p–n heterojunctions, as ZnO was classified as an n-type material, while NiO was classified as a p-type material. Consequently, the movement of electrons (e^-) and holes (h^+) varied to achieve an equilibrium condition characterized by comparable energy levels to the Fermi level, as shown in Fig. 16a.

The sensor adsorbed oxygen from the air onto its surface, extracted the free electrons from the conduction band, and formed a depletion layer at the surface of the sensor particles. This reduced the electron density of sensing materials, resulting in a decrease in conductivity and an increase in resistance. Upon the interaction with NiO-ZnO nanodisks, the SO_2 gas underwent direct oxidation to SO_3 gas due to the presence of oxygenated anionic species adsorbed on the sensor's surface, as shown in eqn (15)–(17). From another perspective, the SO_2 gas presented on the surface of the NiO-ZnO nanodisks underwent oxidation to SO_3 when it reacted with NiO, resulting in the formation of NiS, as shown in eqn (18). The reaction between NiS and oxygenated anionic species converted NiS back to NiO, and the free electrons that transferred to the conduction band of ZnO enhanced its conductivity, as shown in eqn (19).[191]

$$SO_2 + O_{(ads.)}{}^- \rightarrow SO_3 + e^- \quad (15)$$

$$2SO_2 + O_{2(ads.)}{}^- \rightarrow 2SO_3 + e^- \quad (16)$$

$$2SO_2 + O_{2(ads.)}{}^{2-} \rightarrow 2SO_3 + 2e^- \quad (17)$$

$$4SO_2 + NiO \rightarrow 3SO_3 + NiS \quad (18)$$

$$NiS + 3O_{(ads.)}{}^- \rightarrow NiO + SO_2 + 3e^- \quad (19)$$

Different researchers tried to detect SO_2 gases; first, Cui *et al.*[194] used a p-CuO/n-ZnO sensor to detect H_2S and SO_2 gases, and the functional material performed well for H_2S but less effectively for SO_2, as will be presented in Section 4.6 and Fig. 16b. Second, Gaiardo *et al.*[195] studied the use of silicon carbide (SiC) for SO_2 detection, which is a widely recognized substance exhibiting exceptional thermal, mechanical, and chemical durability. This study demonstrated the capacity to trigger chemical reactivity in nanostructured SiC, making it suitable for chemiresistive applications under suitable conditions. They created screen-printed thick films from SiC powder and evaluated them as functional materials for chemiresistive gas sensors in thermo-activation mode. They subjected the samples to 13 gases with significant chemical distinctions. Analyses revealed that SiC is a very discerning functional material for detecting SO_2 at quantities within the ppm range. The intriguing finding was discovered at high operating temperatures ranging from 600 to 800 °C, making it valuable for operation under challenging conditions.

4.5. Hydrogen (H_2)

H_2 is highly flammable and explosive. However, it can be used in a variety of industrial operations, fuel cells, and automobiles equipped with hydrogen power.[71] This is why it is crucial to monitor H_2 levels to ensure safety and prevent hydrogen-related accidents. Metal oxide and metal sulfide semiconductors, palladium-based sensors, and proton exchange membrane (PEM) sensors are utilized by gas sensors intended for the detection of hydrogen and oxygen.[71,196] These sensors, with their quick response times and excellent sensitivity to a small concentration of hydrogen, allow for reliable detection of potential dangers and early warnings.

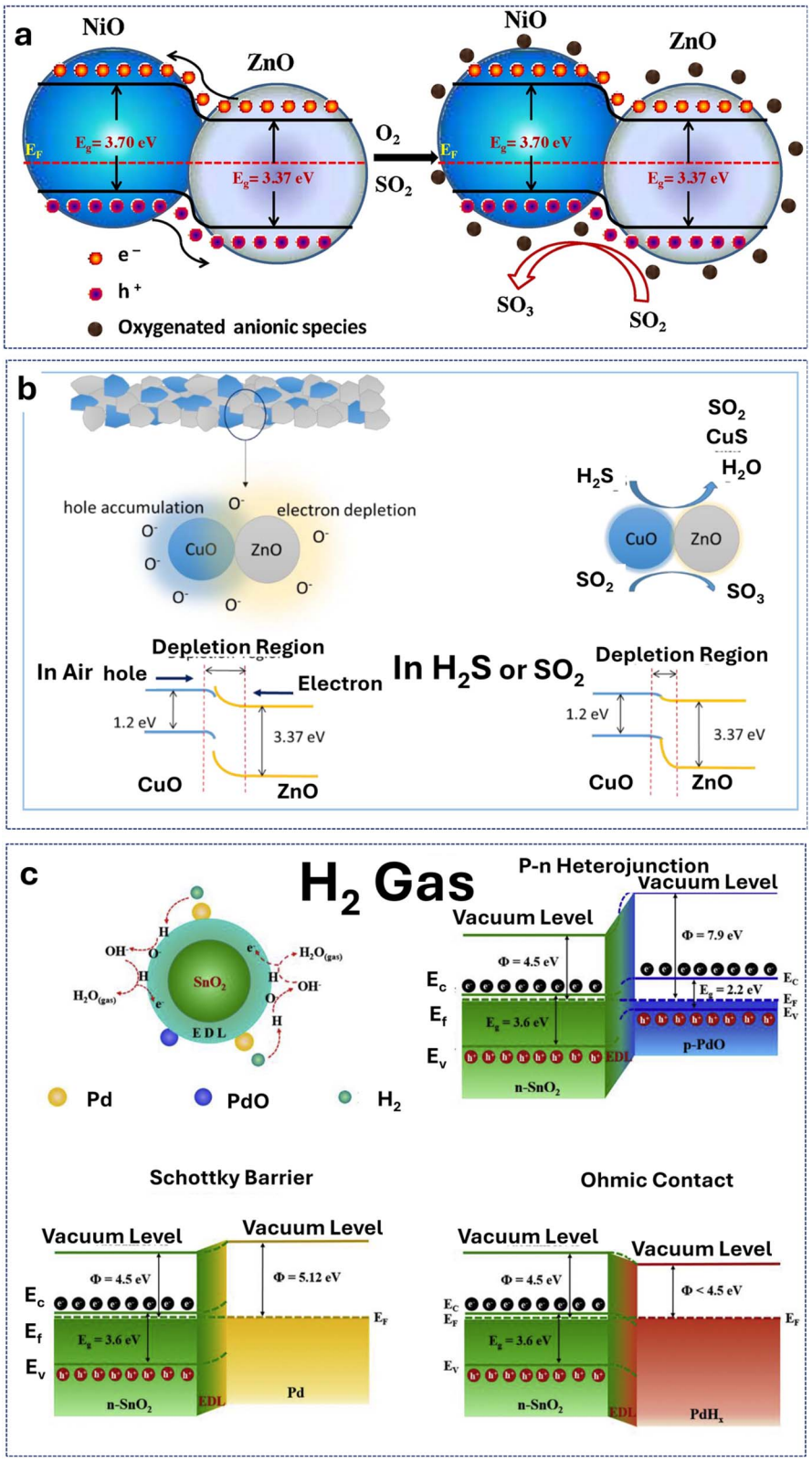

Fig. 16 Gas sensing mechanisms: NiO-ZnO, CuO–ZnO, and Pd/SnO_2 interactions. (a) Proposed SO_2 gas sensing technique for NiO-ZnO nanodisks (reprinted with permission,[191] Copyright 2019, Elsevier); (b) sensor mechanism of p-CuO/n-ZnO nanoparticles, showing material interaction with air, H_2S and SO_2, (reprinted with permission,[192] Copyright 2023, MDPI); (c) H_2 gas sensor mechanism, including a diagram of the Pd/SnO_2 gas sensing interaction and the energy band diagram of n-SnO_2/p-PdO, n-SnO_2/Pd, and n-SnO_2/PdH_x (reprinted with permission,[193] Copyright 2022, Elsevier).

With the growth of the hydrogen production field, the quick detection of H_2 becomes important. Therefore, Meng *et al.*[197] carefully investigated pristine and Pd-modified SnO_2 nanoparticles to sense H_2. The pristine material was synthesized using the hydrothermal technique, and the impregnation process was used for modifying SnO_2 with Pd. The modified sensing material enhanced the H_2 detection capabilities over the pristine material. The sensor with 0.50 at% Pd/SnO_2 showed the highest response magnitude of 254 toward 500 ppm. Additionally, the sensor exhibited a rapid response and recovery time of 1/22 s at 125 °C. Also, the sensor showed great selectivity towards H_2, with a selectivity of 29.83 over C_2H_5OH, while the pristine did not exhibit any selectivity. This is because of the catalytic influence of Pd, the formation of a p–n heterojunction, the presence of a Schottky barrier, and the establishment of an ohmic contact at the Pd/SnO_2 interface.

The gas-detecting process of an MOS sensor, in the work of Meng *et al.*,[197] was attributed to the movement of electrons between the gas and the sensitive body, resulting in resistance switching. At a temperature of 125 °C, O_2 adhered to the surface of SnO_2 and captured unbound electrons from its conduction band, resulting in the formation of oxygen anions. The abovementioned adsorbed oxygen species resulted in the creation of a space charge zone on the surface of SnO_2, thereby reducing the concentration of electron carriers and establishing a state of high resistance, as oxygen is an oxidizing gas. Following this, the introduction of H_2 occurred, leading to a reaction with oxygen anions, terminating the freedom of the resultant free electrons back into SnO_2, as H_2 is the reducing gas, as shown in eqn (20) and (21).

The Pd/SnO_2 sensor demonstrated enhanced H_2 sensing efficacy in comparison to the SnO_2 sensor because of the catalytic action of Pd, as shown in eqn (22)–(25). The presence of Pd reduced the activation energy required for the reaction, resulting in a significant increase in the Pd/SnO_2 response magnitude, as shown in Fig. 16c.

$$H_{2(gas)} \rightarrow H_{2(ads.)} \quad (20)$$

$$H_{2(ads.)} + O_{(ads.)}{}^{-} \rightarrow H_2O_{(gas)} + e^{-} \quad (21)$$

$$H_{2(gas)} \xrightarrow{Pd} H_{(ads.)} + H_{(ads.)} \quad (22)$$

$$H_{(ads.)} + O_{(ads.)}{}^{-} + 2e^{-} \rightarrow OH_{(ads.)}{}^{-} \quad (23)$$

$$OH_{(ads.)}{}^{-} + H_{(ads.)} \rightarrow H_2O_{(gas)} + e^{-} \quad (24)$$

$$Pd + H_{2(gas)} \rightarrow Pd + H_2O_{(gas)} \quad (25)$$

Another example is the highly selective screen-printed Ag-modified SnO_2 for H_2 gas fabricated by Huo *et al.*[198] using an impregnation approach. The sensor composed of 0.6 wt% Ag-SnO_2 had a response of 72.28 to 1000 ppm at 200 °C, 50 times greater than that of pristine SnO_2 (1.38). Furthermore, the modified sensor demonstrated favorable selectivity towards H_2 for CO, CO_2, CH_4, and SO_2 detection. This is because of the combined effects of the chemical spill-over mechanism and the electrical Schottky barriers.

4.6. Hydrogen sulfide (H_2S)

Microbiological activity, industrial activities, and the extraction of natural gas all contribute to the production of H_2S, which is a toxic gas.[74] At high levels, exposure to H_2S can irritate the respiratory system, causing nausea and even death. Consequently, there is an urgent need to detect this gas using several sensing materials, as shown in Fig. 12b and c.[72] These materials include metal oxides, conducting polymers, and nanomaterials. Such sensors possess high sensitivity and selectivity to H_2S, which enable them to provide reliable detection in industrial settings, wastewater treatment plants, and oil refineries.[185]

The gas-detecting mechanism of the pure CuO nanofluid sensor, according to Fan *et al.*,[74] appears to be linked to the absorption of oxygen species on the surface. When the sensor was exposed to the atmospheric air, a significant number of oxygen molecules underwent adsorption on the surface of CuO. This adsorption process involved the capture of electrons located in the valence band (VB), resulting in the formation of oxygen ions, namely O^{2-}, O^{-}, and $O_2{}^{-}$. Upon the introduction of H_2S gas into the gas-sensing test chamber, the resulting oxygen ions underwent a reaction with H_2S, as shown in eqn (26), leading to a reduction in the concentration of free electrons and an increase in the resistance of CuO.

$$2H_2S_{(gas)} + 3O_{2(ads.)}{}^{-} \rightarrow 2H_2O_{(gas)} + 2SO_{2(gas)} + 3e^{-} \quad (26)$$

The gas sensors of CZ NFs had a sensing mechanism connected to both the surface-absorbed oxygen species and the production of p–n heterojunctions when sensing H_2S. The processes of electron transfer from ZnO to CuO and hole migration from CuO to ZnO in the p–n heterojunction system led to the creation of a depletion layer and the bending of the energy band.

After prolonged exposure to air, the gas sensor experienced an expansion of the depletion layer because of electron transfer. At working temperatures below 220 °C, CuO transformed into CuS in the presence of H_2S, as shown in eqn (27). Moreover, when the working temperature exceeded 220 °C, the reaction between CuO and H_2S formed Cu_2S, mostly due to CuS's inherent instability. After eliminating H_2S from the system, CuS converted into CuO, as shown in eqn (26).

$$CuO_{(solid)} + H_2S_{(gas)} \rightarrow CuS_{(solid)} + H_2O_{(gas)} \quad (27)$$

$$2CuS_{(solid)} + 3O_{2(gas)} \rightarrow 2CuO_{(solid)} + 2SO_{2(gas)} \quad (28)$$

The primary function of p–n heterojunctions was to enhance the gas sensing capabilities of CZ NF sensors through the acceleration of charge transfer. Over time, the sensors' resistance stabilized as the oxygen molecules absorbed onto the surface of the CZ NFs. Upon introduction of H_2S gas into the testing atmosphere, it underwent a reaction with oxygen molecules, resulting in the release of a significant number of electrons back to the valence band.

The method reported by Cui *et al.*,[194] in which the p-CuO/n-ZnO sensor detected H_2S and SO_2 gases, which are reducing gases, can be elucidated by the modification of depletion layers

and the p–n junction mechanism, as shown in Fig. 16b. The resistance might vary when subjected to various atmospheric conditions. When exposed to air, oxygen molecules formed near the surface of the sensor's nanomaterial. This reaction involved capturing electrons in the conduction band, resulting in the formation of O_2^-, O^-, and O^{2-}.

Oxygen adsorption thickened the electron depletion layer, increasing the resistance of the p-CuO/n-ZnO sensor in the air. In the given gas environment, the adsorbed oxygen reacted with the gas molecules H_2S and SO_2, as shown in eqn (29). This reaction returned the free electrons to the conduction band, as shown in eqn (30).

$$H_2S_{(gas)} + 3O_{(ads.)}^- \rightarrow H_2O + SO_{2(gas)} + 3e^- \quad (29)$$

$$SO_{2(gas)} + O_{(ads.)}^- \rightarrow SO_{3(ads.)} + e^- \quad (30)$$

Consequently, the formation of a barrier occurred at the interface between CuO and ZnO, leading to an additional augmentation of resistance in the surrounding air. When subjected to H_2S or SO_2 gas, the sensor experienced a reduction in the hole storage width of CuO and the depletion layer width of ZnO due to the release of electrons, leading to a drop in resistance. Hence, when CuO in CuO/ZnO nanoparticles was exposed to H_2S gas, CuO transformed into CuS through a reaction, as shown in eqn (27).

$$CuO_{(solid)} + H_2S_{(gas)} \rightarrow CuS_{(solid)} + H_2O \quad (31)$$

Although CuS exhibited instability under high-temperature conditions, it had the potential to transform Cu_2S. Hence, upon exposure to H_2S gas, the transition from CuO to CuS or Cu_2S resulted in a noticeable decrease in the potential barrier at the p–n heterojunction, consequently enhancing the sensor's conductivity. Upon re-exposure of the sensor to air, CuS underwent conversion to CuO. The sensor's response enabled it to regain its initial high resistance. The sulfuration–desulfuration process explained the CuO–ZnO nanoparticles' increased sensitivity to H_2S compared to SO_2 gas, as shown in eqn (28).

$$CuS_{(solid)} + \frac{3}{2}O_2 \rightarrow CuS_{(solid)} + SO_{2(gas)} \quad (32)$$

Furthermore, Onkar *et al.*[185] synthesized SnO_2 nanoparticles by a microwave-assisted method. They fabricated the SnO_2 film using the screen-printing technique to investigate the gas sensing response towards H_2S, LPG, NH_3, and CO_2 gases. Among them, at 150 °C, the sensitivity and selectivity of the sensor towards H_2S were high, about 16, with no significant response to LPG, NH_3, and CO_2. According to their recommendation, enhancing the H_2S response, response, and recovery time, as well as the selectivity of SnO_2, can be achieved through surface modification or doping with various metal oxides.

Li *et al.*[199] conducted an assessment on an H_2S sensor fabricated *via* electrohydrodynamic (EHD) jet printing. The Pd@TiO_2 and SnO_2 sensing layers was fabricated by single sintering process. Consequently, the sensor's sensitivity was significantly enhanced by increasing the specific surface area and creating a heterojunction because of the presence of PdO nanoparticles on the surface of TiO_2. According to their evidence, the droplets produced by EHD inkjet printing have significantly higher kinetic energy than traditional inkjet printing, resulting in high film thickness, which proves the importance of the thin layer film for some materials. The sensor had a detection limit of 6 ppb and a linear range of 0.02 to 10 ppm of H_2S with a response time of 7 s and a recovery time of 45 s at 2 ppm.

Siriwalai *et al.*[200] created an efficient and dependable H_2S gas sensor using the spin coating technique of RuO_2-decorated WO_3. In the range from 0.25 to 10 ppm, temperatures from 200 to 400 °C, and the humidity levels from 0 to 80 RH%, the 0.2 wt% Ru sensor showed the best response of 71 at 10 ppm and 350 °C in a dry environment with a fast response time of 15.1 s. The sensor also showed long-term stability and high selectivity towards H_2S over methanethiol (CH_3SH), dimethyl sulfide (CH_3SCH_3), acetone (C_3H_6O), ethanol (C_2H_5OH), methanol (CH_3OH), formaldehyde (CH_2O), benzene (C_6H_6), xylene (C_8H_{10}), nitrogen, NO_2, NO, H_2, methane (CH_4), CO_2, acetylene (C_2H_2), formic acid (HCOOH), acetic acid (CH_3COOH), and lactic acid ($CH_3CHOHCOOH$).

Tupe *et al.*[201] focused on the production of thick NiO-CuO films using the screen-printing technique on a glass substrate. The dense layer of the sensing material promoted the detection and analysis of H_2S gas at different concentrations, ranging from 50 ppm to 500 ppm. Hence, the binary oxide sensor exhibited a high sensitivity of 75.01% (100 ppm) at room temperature.

A straightforward solvothermal method was used by Pan *et al.*[72] to prepare Fe-MOF microspheres at 140 °C for 12 hours, followed by annealing at 300 °C for 3 hours to produce hollow nanospheres of alpha-iron oxide, and afterward, different ratios of α-Fe_2O_3 were mixed with molybdenum diselenide to obtain α-Fe_2O_3/$MoSe_2$ (nanosphere/nanoflower shape) confirmed by multiple characterization techniques, as shown in Fig. 17a. The nanocomposite α-Fe_2O_3/$MoSe_2$ in a mass ratio of 4 : 1 exhibited a high performance towards H_2S gas with a very high gas sensitivity response of 57.7, fast response and recovery times (50/53 s) at 30 ppm, and no affect from humidity at room temperature. Furthermore, it exhibited a high selectivity for H_2S in comparison to other gases. Another study by Tan *et al.*[73] used a ZIF-67 MOF as a precursor of double-shelled Co_3O_4/$NiCo_2O_4$ nanocages for H_2S sensing applications, as shown in Fig. 17b. The sensors demonstrated good selectivity, but the response was 8 to 100 ppm H_2S gas at 250 °C, which is low compared to that of Pan *et al.*[72] because of using $MoSe_2$ nanoflowers, which is why the unique double-shelled hollow nanostructures' exceptional gas-sensing capabilities indicated their potential use in the gas sensor industry.

4.7. Ammonia (NH_3)

NH_3 is extensively used in the agricultural industry as a fertilizer.[204] It is also utilized in industrial operations such as refrigeration and the production of chemicals.[205] Prolonged exposure to high concentrations of NH_3 can irritate the

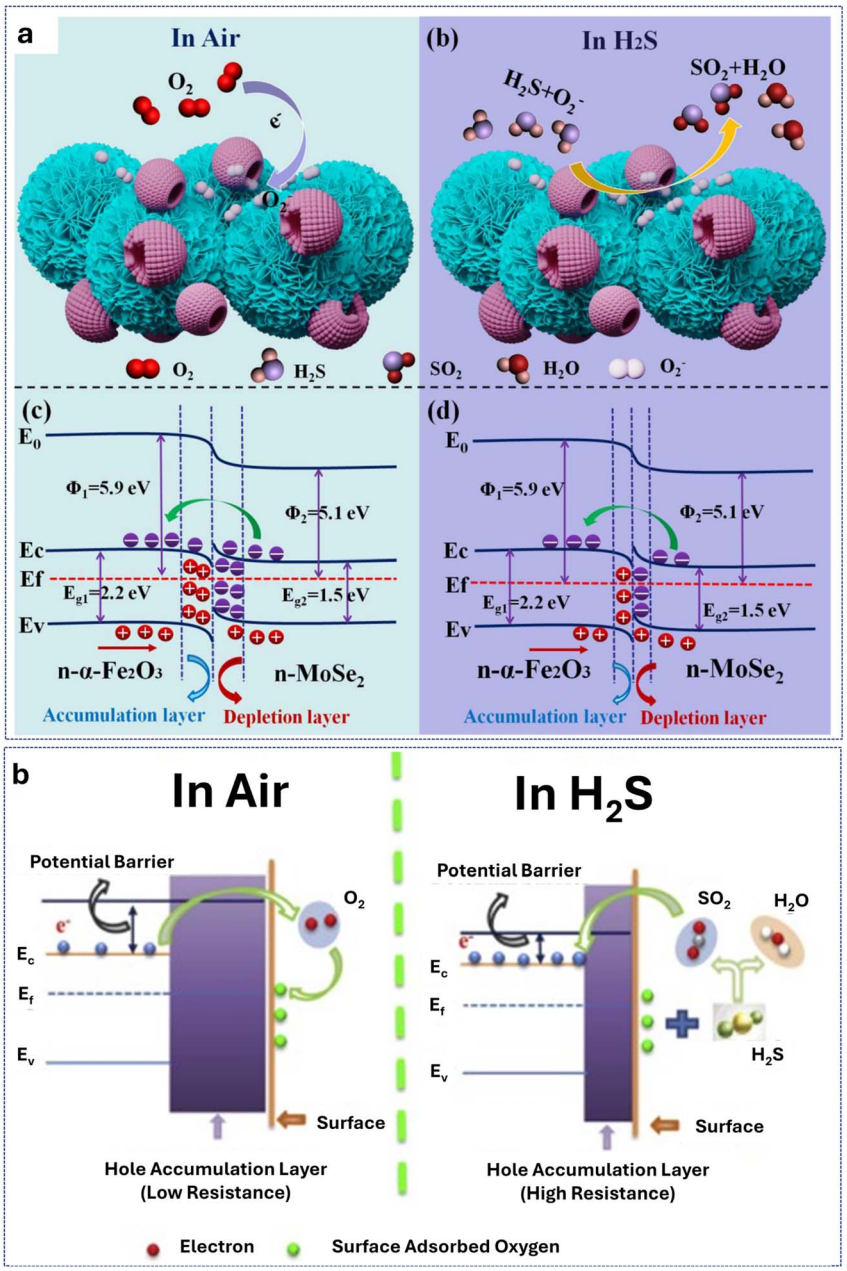

Fig. 17 Materials structure and gas sensing mechanism. (a) Schematic showing the gas-sensing process and energy band structure of the α-Fe_2O_3/$MoSe_2$ composite in air and H_2S gas (reprinted with permission,[202] Copyright 2021, Elsevier); (b) the mechanism of the gas sensor in air and H_2S, showing the hole accumulation layer at low resistance and high resistance with conduction and valence bands and the Fermi level (reprinted with permission,[203] Copyright 2020, Elsevier).

respiratory tract and cause pulmonary edema.[185] Typically, metal oxide semiconductors or electrochemical cells are utilized as sensing elements in gas sensors that are designed for the detection of NH_3, as shown in Fig. 11b.[69] Because of their great sensitivity and selectivity to NH_3, these sensors make it possible to conduct efficient monitoring in a variety of situations, including industrial facilities, agricultural settings, and indoor spaces.[112] The work of Birajdar *et al.*[69] found that when the V_2O_5 material surface was exposed to reducing gases such as NH_3, C_2H_5OH, CH_3OH, and HCHO gas, they reacted with chemisorbed O^- species by releasing electrons into the conduction band, as shown in the reaction below.

The gas-sensing mechanism of metal oxides relied on the fluctuation of their electrical resistance in the presence and absence of the gases being analyzed. The major charge carriers determined the electrical resistance in the presence of analyte gas in metal oxides and the kind of analyte gas. According to Manjunath *et al.*,[92] under normal environmental conditions, a significant number of oxygen molecules underwent adsorption on the surface of the nanostructured BSO (n-type) semiconductor. The dissociation of adsorbed oxygen molecules

occurred, leading to the extraction of free electrons from the conduction band of the metal oxides by each oxygen atom, as shown in Fig. 18a.

During the chemisorption process, the electron density in the metal oxides fell as the electrons from the conduction band returned. Consequently, the electrical resistance of the metal oxides increased. The oxygen molecules that were adsorbed possessed the capacity to eliminate electrons from the surface up to a specific depth known as the Debye length. The area within this Debye length is referred to as the electron depletion layer. The extent of the electron depletion layer is contingent upon several factors, including the size of the grains, the shape of the surface, the concentration of adsorbed oxygen and oxygen vacancies, and the applicable operating temperature. Upon the introduction of the analyte gas, such as NH_3 or HCHO, it underwent a reaction with chemisorbed oxygen species that are dispersed across the surface of the metal oxides, resulting in oxidation, as shown in eqn (33). Concurrently, the electrons engaged in the chemisorption process revert to the conduction band of the single-molecule oxides. Consequently, the electron depletion layer diminishes while the electron density within the metal oxides grows, leading to a reduction in electrical resistance.

$$2NH_3 + 3O_{(ads.)}{}^{2-} \rightarrow N_2 + 3H_2O + 3e^- \quad (33)$$

Guntner *et al.*[206] studied the challenge of the detection of NH_3 at ppb concentrations with high sensitivity, quickly and selectively, using affordable and low-energy sensors at room temperature. They fabricated nanostructured porous CuBr films by depositing CuO onto sensor substrates *via* flame-aerosol deposition and then performing dry reduction and bromination. The porous CuBr films exhibited significantly greater sensitivity to NH_3, with a sensitivity and response time 10 times higher and 5 times faster than those of traditional denser CuBr films at 5 ppb within 2.2 min, even at 90% relative humidity. The NH_3 sensor demonstrated excellent selectivity (30–260) compared to common interfering substances such as C_2H_5OH, acetone, H_2, CH_4, isoprene, acetic acid (CH_3COOH), HCHO, CH_3OH, and CO. Therefore, it can be integrated into wearable electronics.

Narwade *et al.*[120] synthesized hydroxyapatite nanorods on the cellulose nanofibril surface using a hydrothermal method at different temperatures of 120, 150, and 180 °C. The screen-printed thick films were subjected to NH_3 gas sensing using a two-probe electrode set-up at 25 °C. The sample synthesized at 150 °C exhibited superior gas sensing performance, with sensitivity and response and recovery times of 893% and (120/30 s), compared to the other composites.

Cong *et al.*[119] presented a new amperometric NH_3 sensor utilizing SrM_2O_4 (M = Sm, La, Gd, Y) sintered at 1100–1400 °C, with a structural composition similar to $CaFe_2O_4$, which are all classified as n-type semiconductors and coated by screen-printing. Among them, the $SrSm_2O_4$ sintered at 1250 °C showed high performance in detecting NH_3 at concentrations ranging from 25 to 500 ppm and temperatures from 600 to 800 °C. Compared to NO_2, NO, C_2H_4, and CH_4, the NH_3 sensor with a $SrSm_2O_4$-1250 sensing electrode exhibited superior sensitivity at 54.22 nA ppm^{-1}, faster response and recovery times (51/63 s), exceptional selectivity at 500 ppm and 800 °C and long-term stability over 90 days of storage. This indicates promising potential for the implementation of the $SrSm_2O_4$ sensing electrode in automotive equipment.

Yenorkar *et al.*[118] studied pure polypyrrole (PPy), pure molybdenum trioxide (MoO_3), and PPy-MoO_3 formed using mechanical mixing with 40, 60, and 80 wt% of MoO_3 in acetone. The fabricated screen-printed thick films over a glass substrate of pure and polymer–metal oxide hybrids were subjected to calcination at a temperature of 800 °C for 8 hours in the air. The thick film sensors were analyzed using NH_3 and C_2H_5OH gases at room temperature. The pure PPy film exhibited a low sensitivity to the two gases. However, at the same temperature, the thick film containing 60% MoO_3 exhibited a high performance towards NH_3 and C_2H_5OH gases at 60 ppm, with a sensitivity of 1.35 and 0.9, respectively.

As studied by Manjunath *et al.*,[92] the gas sensing properties of heterostructure sensors screen-printed with different ratios of ceria and ruthenate-sensitized $BaSnO_3$ (BSO) with La doping were investigated for the detection of NH_3 and HCHO gases at room temperature. Specifically, they achieved a gas response of 65 to 50 ppm of NH_3 and a gas response of 29 towards 50 ppm of HCHO, as shown in Fig. 18a. Another study by Manjunath *et al.*,[39] as shown in Fig. 18b, compared the sensing abilities of Sr-doped ZnO and RuO_2-activated Sr-doped ZnO heterostructure sensors for detecting NH_3 gas at room temperature with concentrations of ≤50 ppm. For Sr-ZnO, they found that the gas response was 71 at 50 ppm of NH_3 gas at room temperature, while the presence of a passivation layer and the no-spill-over activity of RuO_2 reduced the gas response of the RuO_2-activated Sr-ZnO sensor from 71 to 3. The sensor based on Sr-doped ZnO exhibits excellent selectivity for NH_3 compared to 50 ppm of VOC vapor.

4.8. Liquefied petroleum gas (LPG)

LPG gases are frequently discovered in petroleum and industrial processes, including propane and butane.[174] Monitoring the levels of LPG is necessary for safety, protecting the environment, avoiding fire accidents or explosions, and saving energy. Gas sensors utilize several different technologies for LPG detection. These technologies include metal oxide semiconductors, catalytic combustion sensors, and infrared absorption spectroscopy technologies. Because of their high sensitivity and selectivity to LPG, these sensors can enable precise detection in a variety of scenarios, including residential, commercial, and industrial environments.[185]

In the work of Reddy *et al.*,[207] the adsorption and capture of electrons from the conduction band by atmospheric oxygen in n-type semiconductors resulted in the generation of ionized oxygen anions and superoxide anions (O_2^-) at room temperature. This process resulted in the formation of a depletion layer, which then induced band bending and created a surface potential barrier. Air exposure (R_a) subjected the chemiresistive sensor MgO@CeO_2 to the adsorption of O_2 molecules on the

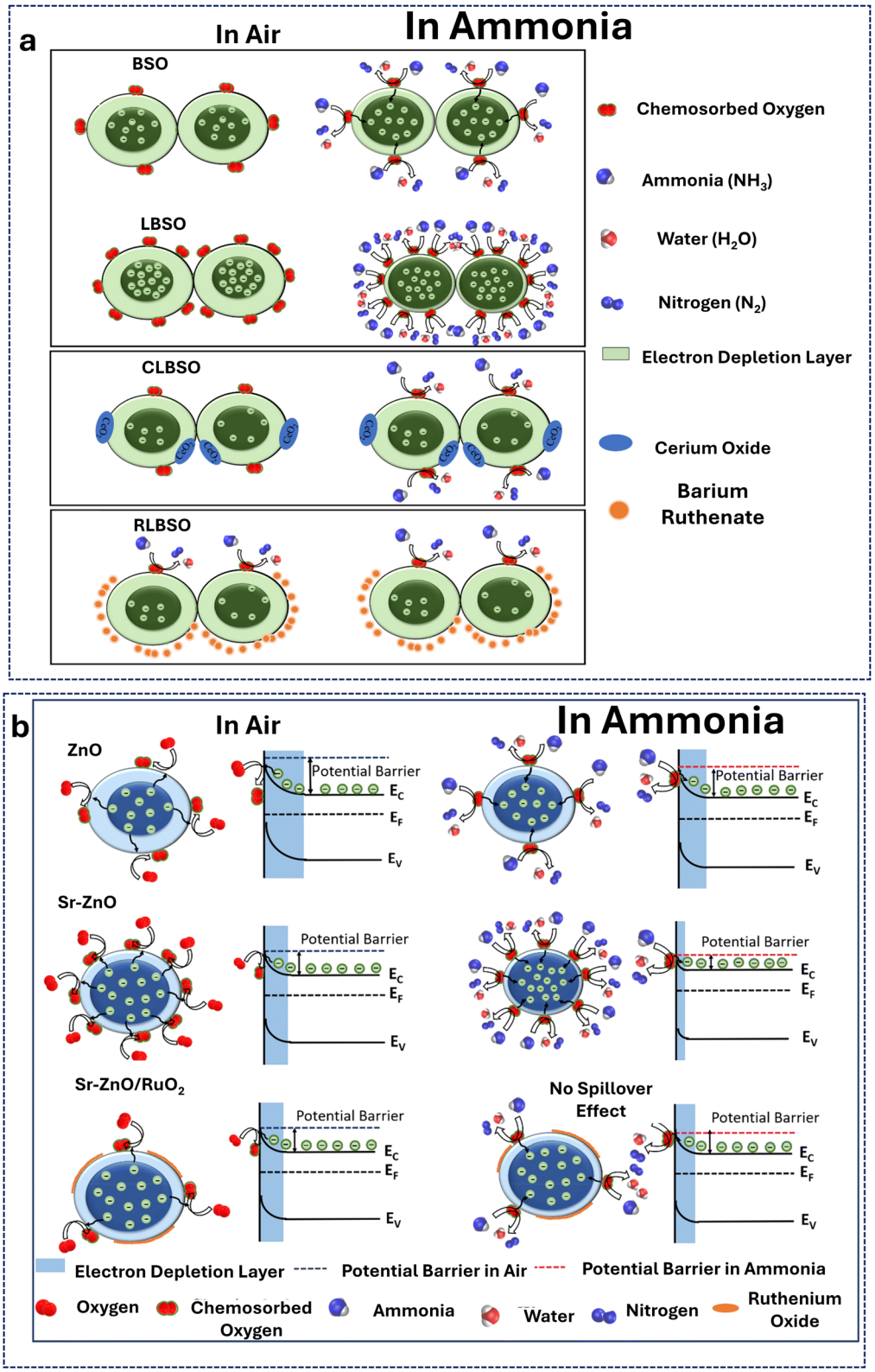

Fig. 18 Gas sensing mechanism for ammonia gas sensing. (a) Diagram showing the interaction of virgin BSO, LBSO, CLBSO, and RLBSO sensors with ammonia gas (reprinted with permission,[92] Copyright 2021, Springer Nature); gas sensing interaction of ammonia with active materials. (b) Schematic of undoped ZnO, Sr-doped ZnO, and RuO_2-activated Sr-doped ZnO gas detecting mechanism with the band diagram in air and ammonia (reprinted with permission,[39] Copyright 2020, Springer Nature).

surfaces of MgO and CeO_2. This adsorption process trapped electrons from the MgO@CeO_2 nanocomposite's conduction bands. As a result, the nanocomposite's surface formed depletion layers, creating a heterojunction interface. When subjected to LPG (R_g), the MgO@CeO_2 sensor exhibited a response characterized by the presence of superoxide anions on its surface. These anions were readily accessible and released a substantial number of trapped electrons, as shown in Fig. 19a–e. This phenomenon has a notable impact on the resistance drop.

In LPG sensing, the reducing gas reacted with adsorbed oxygen anions, and a complex series of reactions took place, ultimately oxidizing LPG gases, as shown in eqn (34)–(37).

$$C_nH_{2n+2} + O_2^- \leftrightarrow C_nH_{2n}{:}O_{2(gas)} + e^- + H_2O_{(ads.)} \quad (34)$$

$$C_nH_{2n+2} + O_2^- \rightarrow CO_{2(gas)} + H_2O_{(gas)} \quad (35)$$

$$C_4H_{10} + \frac{13}{2}O_2^- \leftrightarrow 4CO_{2(gas)} + \frac{13}{2}e^- + 5H_2O_{(gas)} \quad (36)$$

$$C_3H_8 + 5O_2^- \leftrightarrow 3CO_{2(gas)} + 5e^- + 4H_2O_{(gas)} \quad (37)$$

where C_nH_{2n+2} signifies various compositions with $n = 3$ and 4, such as C_3H_8, and C_4H_{10}.

Moreover, Garje *et al.*[59] synthesized a nano-crystalline SnO_2 (101) plane using a surfactant-assisted solution precipitation process. In addition, they created a thick film of a functional

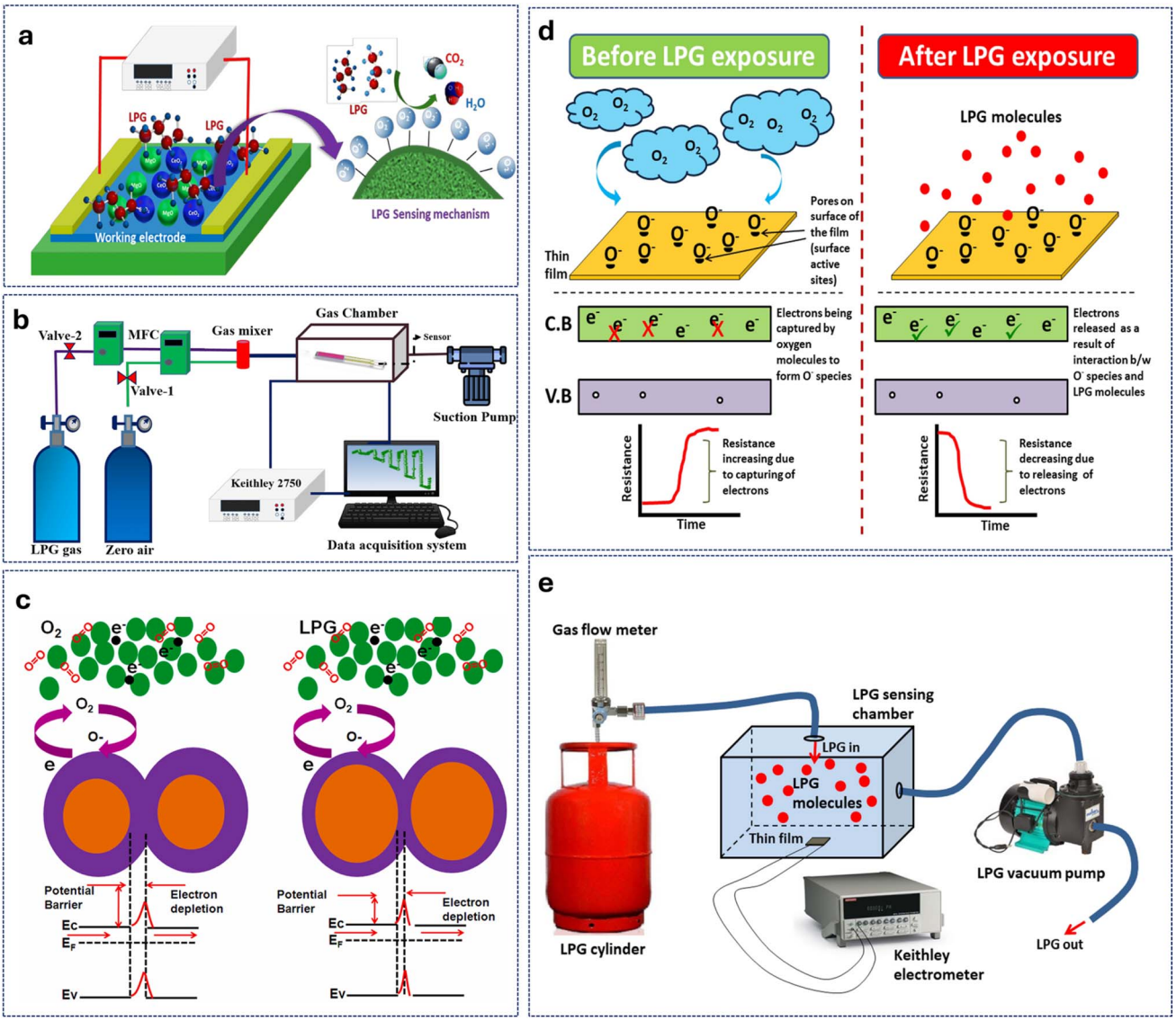

Fig. 19 (a) Gas sensing mechanism of metal oxide semiconductor electrode for LPG (reprinted with permission,[207] Copyright 2019, Springer Nature); (b) a schematic diagram of the LPG gas sensor set-up (reprinted with permission,[207] Copyright 2019, Springer Nature); (c) gas sensing mechanism of LPG gas, highlighting the electron depletion layer of the MoS_2/GR composite for the gas sensing technique with air and LPG gas (reprinted with permission,[208] Copyright 2022, Elsevier); (d) the schematic diagram of the LPG-detecting mechanism before and after exposure to LPG, showing the formation of O^- species on pores prior to LPG gas interaction (reprinted with permission,[209] Copyright 2021, Springer Nature); and (e) LPG sensing setup of LPG gas, comprising an LPG cylinder connected to a gas flow meter and sensing chamber with an LPG vacuum pump to remove the gas as well as a Keithley electrometer (reprinted with permission,[209] Copyright 2021, Springer Nature).

material consisting of the synthesized nanocrystalline SnO_2 with 15 wt% glass frit using a screen-printing technique. The sensor exhibited significant sensitivity towards H_2, CO, and LPG at 400 ppm and the operating temperatures of 120, 150, and 70 °C with sensor responses of 30, 25, and 46, respectively. The calculated response and recovery times of H_2, CO, and LPG at 400 ppm were (12/84), (16/34), and (10/36 s), respectively. What can be concluded is that good selectivity and sensitivity towards LPG at low operating temperatures were because of the small particle size and optical band gap.

Vishwakarma *et al.*[210] investigated the fabrication of thick films based on SnO_2 doped with PbO using the screen-printing technique on an alumina substrate for sensor applications. The sensing capabilities of the produced thick films were evaluated at 200 °C, with different concentrations of LPG ranging from 0 to 5000 ppm. At 200 °C and 5000 ppm for 1 wt% PbO calcined at 900 °C, they observed the greatest response of LPG was 26%, which was 2 times higher than that of pristine SnO_2, while the response for 1 wt% PbO prepared at 800 °C was 20%. For LPG, the sensitivity of sensor S3 compared to S1 is almost twice as high, while its sensitivity compared to S2 is approximately 1.47 times higher. Hence, the PbO-SnO_2 sensor can be used for detecting LPG.

Patil *et al.*[122] synthesized the nanoscale materials of SnO_2, ZnO, and SnO_2-ZnO using a combination of microwave and ultrasonication techniques. The thick film fabrication process was created using a straightforward screen-printing process. The symmetrical *I–V* characteristics illustrated both the ohmic and non-ohmic properties of the thick films. The electrical resistivity measurements demonstrated a negative temperature coefficient of resistance behavior. The LPG response with varying doping concentration indicated that the ZnO-thick film doped with 1 wt% SnO_2 showed a significant response and was highly selective towards 100 ppm of LPG at 50 and 100 °C, compared to other gases, including CO_2, NH_3, H_2, Cl_2, O_2, and ethanol. Therefore, the modified sensor is a suitable candidate for LPG sensing with high selectivity, sensitivity, and fast response and recovery.

Kabure *et al.*[121] reported ultrafine CeO_2, α-Fe_2O_3 nanoparticles (NPs) and CeO_2-Fe_2O_3 nanocomposites (NCs) for LPG sensing applications synthesized using the microwave-assisted sol–gel technique. The screen-printed sensor showed optical examination results that revealed a decrease in band gap energy from 3.19 eV (E_g-CeO_2) to 1.4 eV (E_g-CeO_2-Fe_2O_3). The screen-printed films composed of pure CeO_2, Fe_2O_3, and CeO_2-Fe_2O_3 were tested with different concentrations of 12, 16, 20, 24, and 28 ppm LPG at 250 °C. The CeO_2-Fe_2O_3 film showed the most significant response of 61.43%. The gas sensing results showed that the nanocomposite thin film was extremely sensitive to LPG at 250 °C and could detect a minimum concentration of 24 ppm, with a sensor response of 61.43% and fast response and recovery times of 22 and 52 s. This sensor response was higher than that of pure CeO_2 (52.13%) and α-Fe_2O_3 (48.29%) because of the high porosity and the formation of a p–n heterojunction between CeO_2 and Fe_2O_3. Additionally, the presence of Ce^{4+}/Ce^{3+} species in Fe_2O_3 promoted electron interaction.

4.9. Volatile organic compounds (VOCs)

VOCs are carbon-containing organic compounds that comprise a broad spectrum of chemicals released into the atmosphere by various sources.[69,76] These sources include paints, solvents, cleaning agents, and building materials.[211] VOCs, such as furaneol, methanol, xylene gas, acetone, and formaldehyde, can cause adverse health effects and contribute to the contamination of the air within buildings.[70,98,169,212–214] Pollution leads to a significant increase in the concentration of various types of pollutants in the atmosphere. The presence of diverse contaminants in the atmosphere gives rise to significant environmental and human health risks. Therefore, different gaseous substances such as CO_2, NO_2, CO, and VOC often contain high concentrations of these diverse contaminants.

Furthermore, there are additional prevalent gas vapors in the vicinity that might react with other atmospheric gases, resulting in a significant combination of molecules that can exacerbate severe health risks. Therefore, it is necessary to detect the concentration of these harmful gases at a small scale, such as ppm, as shown in Fig. 10a. Recently, researchers have devised a multitude of methods to detect the harmful concentration of such gases at extremely low levels. For gas detection, researchers have created many sensors, including chemiresistive-based, optical, colorimetric, electrochemical, capacitance-based, and acoustic-based gas sensors.[56,67,169,215–217] Semiconducting materials form the basis of the chemiresistors used in these sensors, as shown in Fig. 20a and b. Semiconductors possess significant advantages in terms of cost-effective synthesis, high efficiency, high gas response ratio, and reduced environmental hazards.[36]

Gas sensors utilize metal oxide semiconductors, polymer films, and photoionization detectors to detect VOCs.[75,219,220] The great sensitivity and selectivity of these sensors to VOCs allow them to be used for effective monitoring in industrial facilities, environments, biomedical devices, and indoor and outdoor air quality networks.[167,221,222]

Furthermore, due to the importance of detection of VOCs, Liu *et al.*[223] fabricated a fully screen-printed transparent ZnO/rGO sensor for ethanol detection that can be used in several applications. They extensively examined and optimized the performance of the sensor for ethanol at 25 °C. The sensor exhibited excellent performance, including favorable selectivity, high gas sensitivity, good stability, and a short response/recovery time of 0.2–9 ppm. The gas sensor presented in their study has several notable advantages, including transparency, breathability, biocompatibility, and biodegradability. These qualities make them highly promising for use in portable or wearable electronic devices designed to detect trace amounts of ethanol at ambient temperatures.

Shedam *et al.*[224] studied a highly selective screen-printed gas sensor prepared using $Mg_{1-x}Cd_x Nd_yFe_2O_4$ ($x = 0.0, 0.1, 0.3, 0.5, 0.7$) toward ethanol over LPG and chlorine. A Mg–Cd–Nd ferrite ethanol sensor, specifically $Mg_{0.5}Cd_{0.5}Nd_{0.02}Fe_{1.98}O_4$, was much more sensitive to 100 ppm ethanol gas at 350 °C and exhibited a notable selectivity for the detection of ethanol in comparison

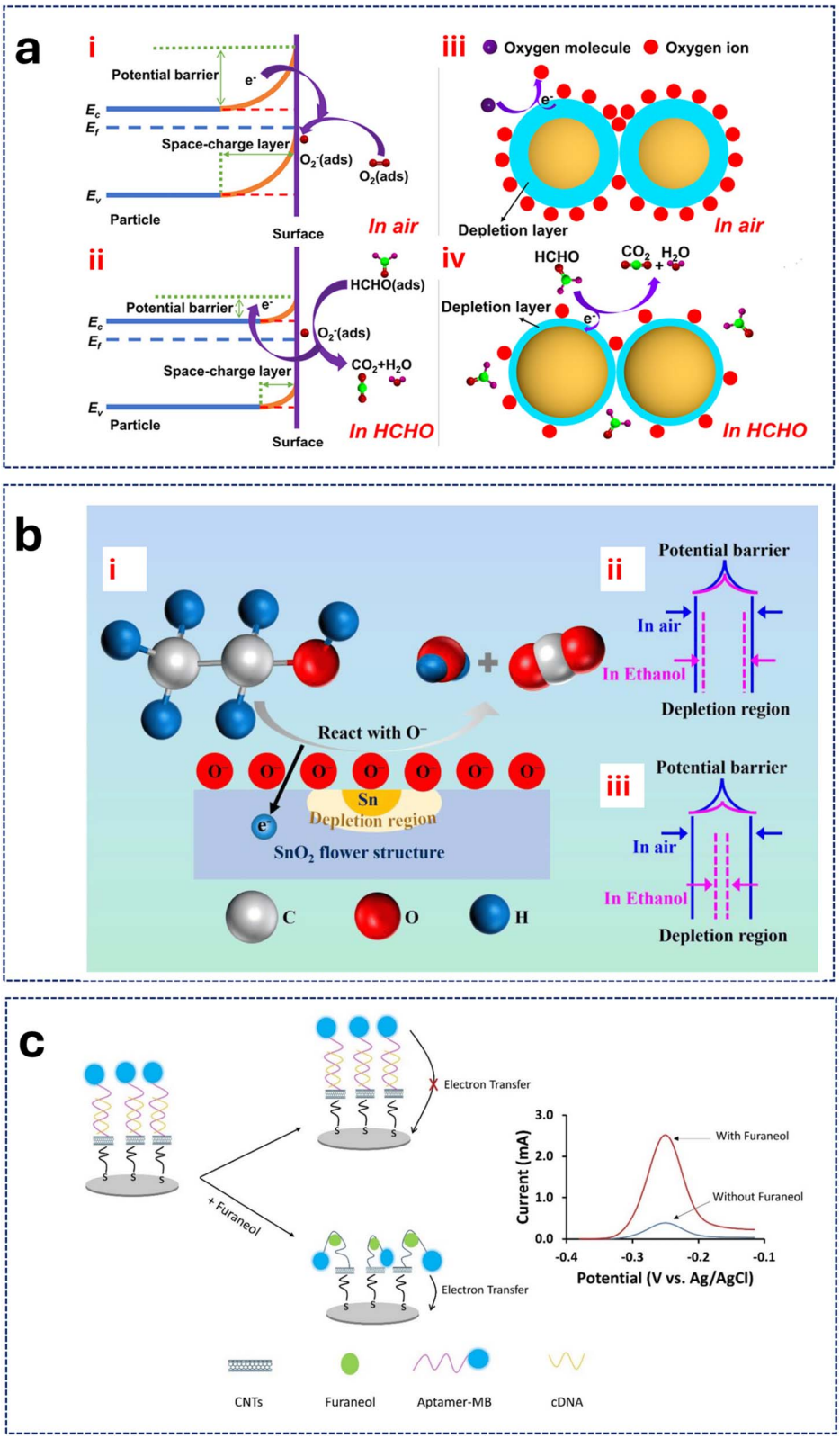

Fig. 20 Gas sensing mechanisms: formaldehyde, ethanol, and furaneol detection schematics are illustrated. (a) Schematic diagram of the gas-sensing mechanism of the laminar SnO_2 gas sensor for formaldehyde, illustrating its behavior in both air (i) and formaldehyde (ii). (iii) and (iv) Schematic diagrams illustrating the electron depletion layer hypothesis for SnO_2 gas-sensing materials (reprinted with permission,[76] Copyright 2022, American Chemical Society); (b) schematic diagram of the possible gas-sensing mechanism of Sn/SnO_2 samples for ethanol gas and the energy band structure of pure and Sn-doped SnO_2 (reprinted with permission,[218] Copyright 2023, MDPI); (c) schematic diagram of the working principle of the CNT-Modified Electrode (ME) aptasensor for furaneol detection by using a carbon nanotube electrode modified with aptamer-methylene blue (MB) and complementary deoxyribonucleic acid (cDNA) as the current change generated by the MB label was used for furaneol detection (reprinted with permission,[214] Copyright 2020, MDPI).

to other gases and demonstrated high levels of repeatability and stability.

Douaki *et al.*[214] studied the detection of furaneol in some fruits, such as strawberries, by comparing two different materials, which were CNTs and Ag nanoparticles, to detect the change in an aptasensor electrochemical sensor, as shown in Fig. 20c. CNT-modified electrodes (CNT-MEs) outperformed AgNP-MEs under optimum conditions. CNT-MEs had a linear detection range of 1 fM to 35 μM, whereas AgNP-MEs had a linear range of 2 pM to 200 nM. Additionally, CNT-MEs exhibited good selectivity towards furaneol, verified using high-performance liquid chromatography (HPLC).

5. Integration of advanced technology

The integration of modern technology with screen-printed gas sensors represents a cutting-edge approach to improving sensor performance, functionality, and versatility.[225] Researchers constructed gas and humidity sensing platforms for the next generation by integrating screen printing with various novel technologies.[78,95] These platforms can address complicated challenges in the areas of environmental monitoring, industrial safety, and healthcare applications.[221] The proposed layer of carbon nanotubes (CNTs) deposited with the spray printing technique exhibits durability throughout future microfabrication procedures, thereby showcasing a resilient approach for incorporating nanomaterials into traditional microelectromechanical systems (MEMS).[32] The flexible smart packaging system was implemented by integrating an RFID chip with an antenna, a printed NH_3 sensor, and an anti-open sensor into a plastic packaging film.[221] The RFID chip, equipped with an antenna, utilizes wireless energy harvesting to facilitate the acquisition of sensed data and enable communication with the reader, which, in this case, is a smartphone. The gas sensor quantifies the relative freshness of the meat contained within the packaging, while the anti-open sensor assesses the integrity of the package.[221] Hence, this section will discuss the potential integration of screen-printed gas sensors with advanced technologies, including AI, ML, photovoltaic solar cells (PVs), micro-supercapacitors (μSCs), triboelectric nanogenerators (TENGs), and heaters for smart applications like digital twins, as shown in Fig. 21.

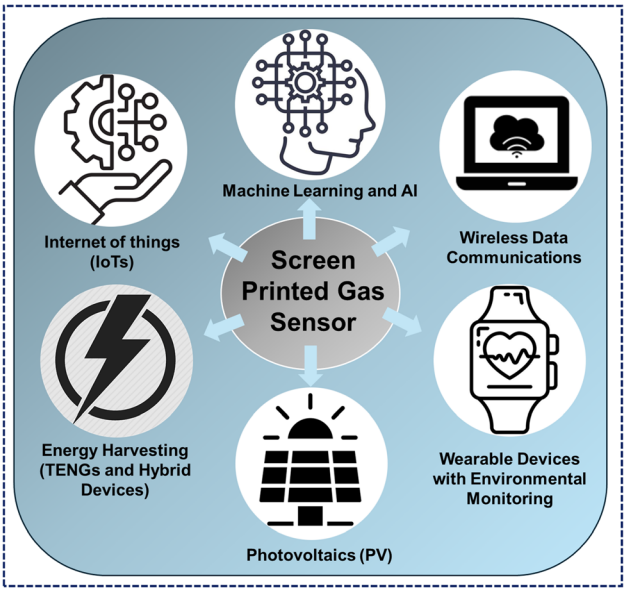

Fig. 21 A schematic diagram of the integration of advanced technologies with screen-printed gas sensors for smart applications.

5.1. Artificial intelligence (AI)

In many different applications, AI has become crucial for enhancing the accuracy and performance of gas sensors. To improve aviation safety, AI can be used to optimize the integration of smoke detectors and CO_2 sensors in aircraft, which increases detection reliability and lowers false alarms, as discussed by Zhu *et al.*[226] By evaluating sensor data to account for environmental variables such as temperature and humidity, AI models were used by Kul *et al.*[227] to improve the performance of TiO_2-based CO_2 sensors and guarantee accurate real-time CO_2 measurements. Furthermore, according to Boonthum *et al.*,[228] AI-driven pattern recognition enhanced the classification of gases, including ethanol and ammonia, despite interference from other gases, thereby resolving cross-sensitivity problems in gas sensor arrays. To improve the sensitivity and response times of $BaTiO_3$-based CO_2 sensors in the work of Chachuli *et al.*,[229] AI techniques could be used. This would guarantee more dependable detection in applications such as environmental protection and air quality monitoring. AI can also be used to improve flexible, printed gas sensors, as discussed by Masat *et al.*[230] These sensors are lightweight and inexpensive and can monitor gases like H_2, NH_3, and H_2S in a variety of environments. Advanced data analytics can improve the accuracy of these sensors.

AI algorithms can analyze data in real-time and find patterns.[231] This leads to predictive maintenance, finding outliers, and adjusting sensor calibration.[232,233] AI-powered gas sensor systems have the potential to intelligently enhance sensor performance and adjust to changing environmental conditions, thereby improving overall reliability and efficiency. Gupta *et al.*[234] applied AI that enables personal computers (PCs) to acquire knowledge without being specifically tailored to their needs to anticipate the performance of gas sensors regarding the information possessed. AI can provide benefits to a variety of strategies.[18] AI is primarily categorized into different types of learning, which are supervised and unsupervised learning through reinforcement.[234]

Another example is multimodal AI studied by Narkhede *et al.*[235] as the solution for the rising number of accidents happening due to gas leaks at coal mines, chemical industries, and home appliances; hence, they presented an innovative methodology for the detection and identification of gaseous emissions using multimodal AI fusion approaches. They manually gathered a total of 6400 gas samples, taking 1600 samples from each of the four classes. They obtained these samples using two distinct sensors: a semiconductor gas sensor

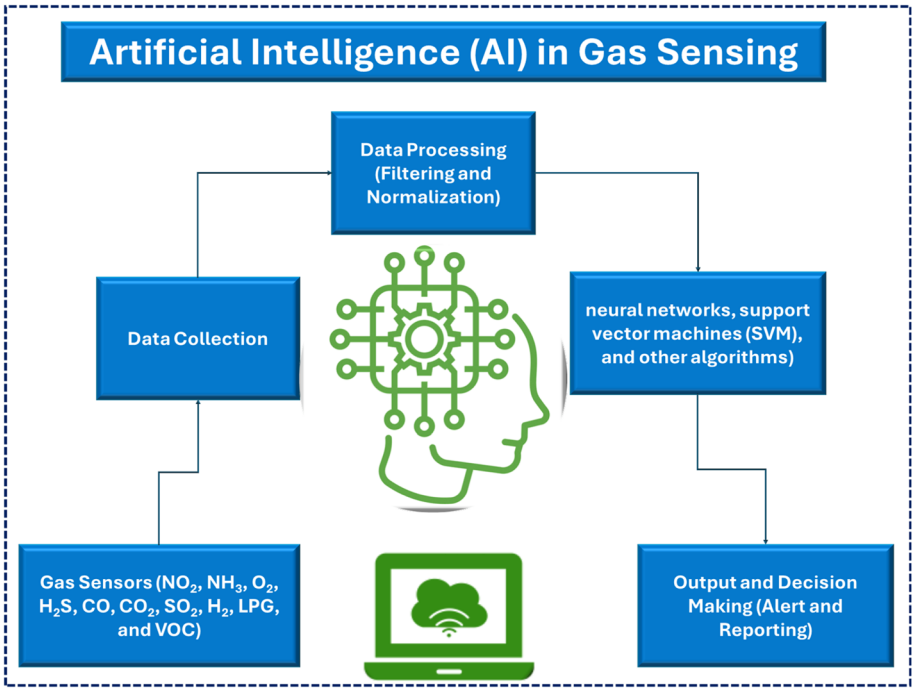

Fig. 22 Schematic diagram of Artificial Intelligence (AI) in gas sensing.

array with 7 groups and a thermal camera. A module in the network structure extracts features specific to each modality and subsequently combines them using a merged layer. A dense layer follows, generating a unified output for gas identification. The fused model achieved a testing accuracy of 96%, whereas the individual models achieved accuracies of 82% (using long short-term memory (LSTM) for gas sensor data) and 93% (using Convolutional Neural Network (CNN) for thermal imaging data). Their findings indicate that the integration of several sensors and modalities yields superior results compared to using only one sensor. To get a precise and effective examination of mixed gases, it is vital to create an electronic nose system that possesses gas sensors with a high level of sensitivity and requires minimal data processing complexity.[236]

Furthermore, Mu *et al.*[236] fabricated a gas sensor array with a micro-electromechanical system (MEMS) based on metal oxide semiconductors (MOSs). They used an inkjet printer to print sensing materials onto a micro-hotplate. The pattern recognition unit employed a one-dimensional convolutional neural network (1D-CNN) to identify seven distinct types of gases accurately. The ideal standard ML algorithm demonstrated a recognition accuracy of 80%, while the 1D-CNN approach demonstrated a significantly higher accuracy of 99.8%. They also evaluated the impact of various time series input lengths on the model's accuracy. They identified an appropriate sample period of 15 seconds based on the findings. The results of this study demonstrate that integrating a MEMS sensor array with the 1D-CNN algorithm has potential as a viable method for complex gas classification and identification.

The utilization of AI in data analysis on cloud servers facilitates the development of novel AI of IoT technology, as shown in Fig. 22.[226] This technology employs affordable and flexible sensors to collect data and then wirelessly transmits them to the cloud. ML methodologies enable remote data assessment in cloud computing environments. With the utilization of upcoming 5G and IoT technologies, there is a high demand for the H_2 sensor due to the need for real-time monitoring in personal healthcare applications. Principal component analysis (PCA) is a valuable method for scientifically studying algorithms and statistical models that enable hydrogen identification in highly distorted environments, allowing for the visualization of huge amounts of data from sensors.[237,238]

Conventional inflexible sensors and flawed calibration techniques pose challenges in meeting the requirements for monitoring the quality and safety of aquatic products in the supply chain. With the need for redesign and optimization of NH_3 sensors, Xu *et al.*[239] developed and enhanced a passive flexible NH_3 sensor for monitoring aquatic environments using an adaptive parameter adjustment artificial neural network (APA-ANN). The sensor could collect data on NH_3 levels and transmit them to a wireless reader using radio frequency identification (RFID) technology operating at a frequency of 13.56 MHz. To collect RF energy, the passive flexible NH_3 sensor used the energy harvesting module with an efficiency of around 63.07%. Then, they used this collected energy to continuously power the sensor, thereby eliminating the need for a battery. In addition to that, they conducted the calibration and verification of the sensor output using oysters and abalone under waterless and watery conditions, respectively. The sensor output exhibited a high level of accuracy within the sensing range ($R^2 > 0.99932$). Additionally, the APA-ANN algorithm improved and optimized the sensor output's precision, even in the presence of various interferents

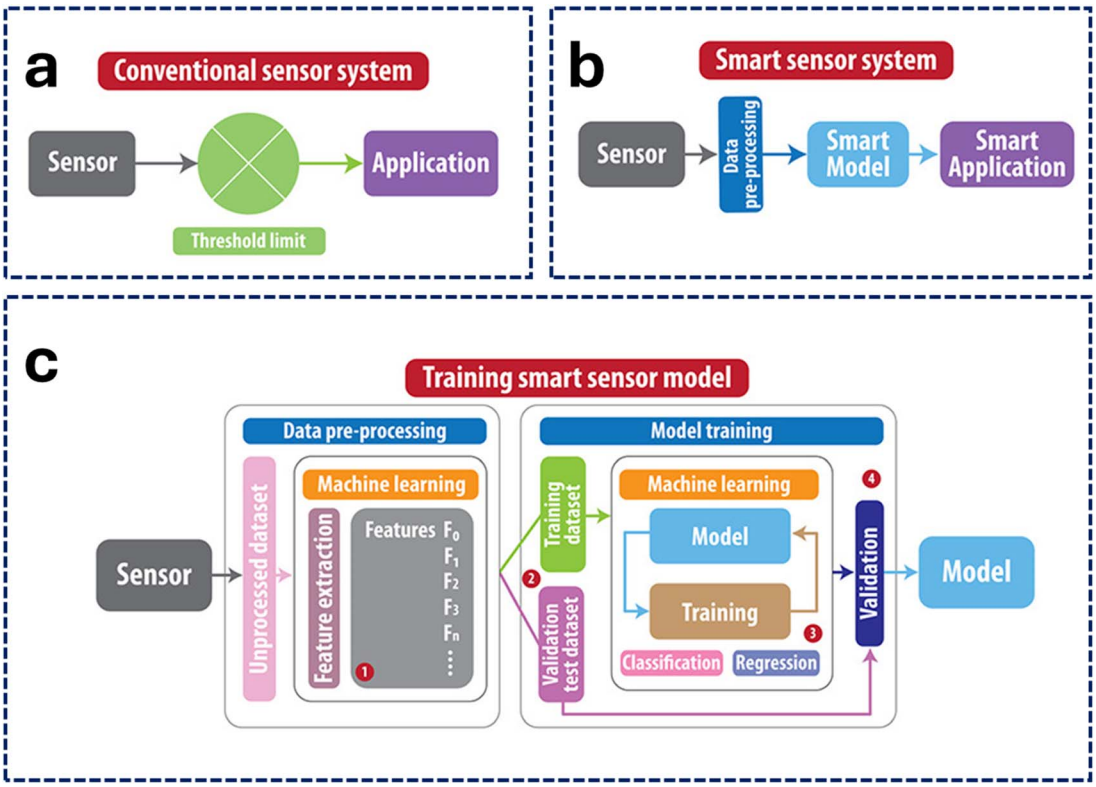

Fig. 23 A comparison between the conventional sensing system and ML-enabled smart sensor system: (a) a block diagram illustrating the traditional sensor-to-application of a conventional sensor system. (b) A block diagram of a modern interpretation of a smart sensor system, and (c) gas sensor data are processed for the smart model and smart application outcome: a general overview of the development and training scheme for a smart sensor system (reprinted with permission,[242] Copyright 2020, Wiley).

and cross-sensitivity. The end outcome showed that all regression coefficients exceeded 0.997, and the accuracy of the optimization model exceeded 89.5%. This confirmed the effectiveness of the passive flexible NH_3 sensor and offered a sustainable monitoring approach for agricultural purposes.

5.2. Machine learning (ML)

ML algorithms enable gas sensor systems to learn from and adapt to data patterns. Abir *et al.*[91] applied ML algorithms to model the gas sensing sensitivity of polyaniline/graphene (PANI/Gr) as they collected a comprehensive dataset gathered from the literature for different gases such as toluene, NH_3, and benzene gases, considering four factors that affect gas sensor performance, including matrix, filler, synthesis conditions, and operating conditions.[91] The model's precision and effectiveness result in notable enhancements to the sensor's accuracy, stability, and reaction time.[240] By utilizing techniques from ML, gas sensors can discern between various species of gases, improve selectivity, and reduce the number of false alarms, which ultimately increases the overall dependability and performance of the system.[237,238,241]

To fully understand the different types of ML algorithms utilized in smart sensor platforms, Ha *et al.*[242] provided a detailed study of intelligence models specifically designed for practical sensing applications. They categorized the ML algorithms into two groups: first, classic non-neural network (non-NN) algorithms such as Principal Component Analysis [PCA], Support Vector Machine [SVM], and Random Forest [RF]. The second category includes neural network (NN) algorithms such as Backpropagation Neural Network [BP-NN], Recurrent Neural Network [RNN], and Convolution Neural Network [CNN].[240] Compared to traditional sensor systems, these models offer a more efficient solution by processing millions of data points simultaneously, resulting in a significant reduction of analysis and training time, as shown in Fig. 23a–c.

Optimizing the sensitivity, selectivity, and calibration of gas sensors requires ML, particularly in difficult-to-detect environments where multiple gases may interfere with detection. Additionally, Le Pennec *et al.*[243] explored how ML models may help maximize the sensitivity of gas sensors that integrate PEDOT:PSS with multi-walled carbon nanotubes (MWCNTs), guaranteeing that these sensors maintain their responsiveness to gases such as ammonia while reducing cross-interference. To improve sensor accuracy despite interference from other ions, Aliyana *et al.*[244] used ML models, such as random forests and neural networks, to correlate impedance changes in zinc oxide/multi-walled carbon nanotube (F-MWCNT/ZnO) composite sensors with NH_4^+ ion concentrations. Similar to this, Mei *et al.*[245] presented how ML can be used to analyze impedance data from MEMS-based gas sensors. This allows for the optimization of the sensitivity and response time of these low-power

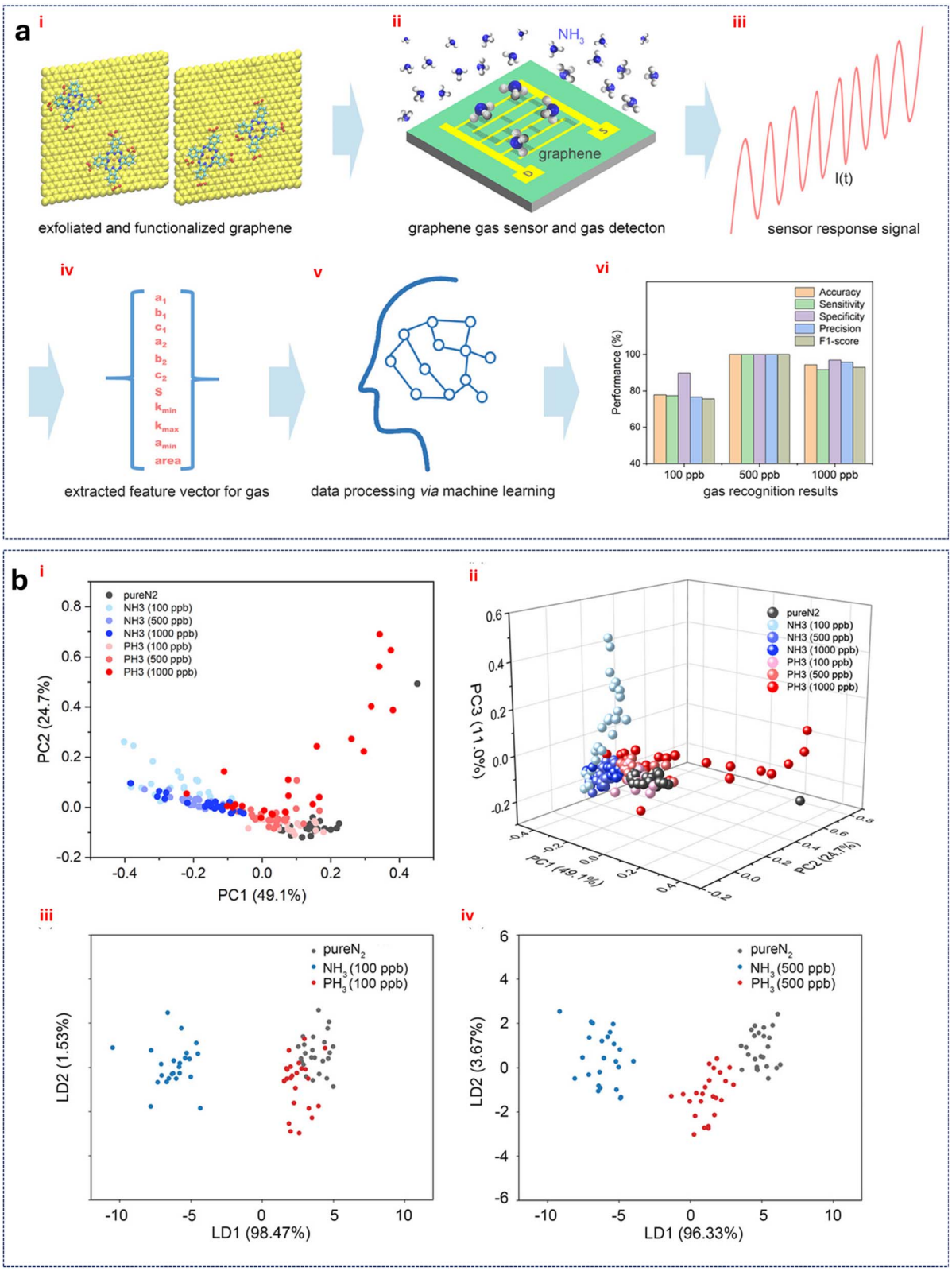

Fig. 24 Graphene-based gas sensing: NH_3 detection, ML classification, and PCA plots. (a) (i) The layered structure of graphene and modified graphene using copper phthalocyanine-3,4′,4″,4‴-tetrasulfonic acid tetrasodium salt (CuPc), (ii) the gas sensor interdigitated (IDE) design composed of graphene as a sensing material interacting with analyte molecules, such as NH_3, (iii) the graphene nanosensor's current signal when exposed to analyte gas, and (iv) the sensor response profile presented as feature vectors to analyze the analyte gas. (v) supervised algorithm machine learning classifier techniques to process feature data. (vi) the results of sensor performance evaluation and identification (reprinted with permission,[238] Copyright 2022, Wiley); PCA score plot for both NH_3 and PH_3 analyte gases at different concentrations: (b) (i) 2D space plot, (ii) 3D space plot, (iii) linear discriminant analysis (LDA) score plot for both NH_3 and PH_3 analyte gases at 100 ppb concentration, and (iv) LDA score plot for both NH_3 and PH_3 analyte gases at 500 ppb concentration (reprinted with permission,[238] Copyright 2022, Wiley).

sensors, guaranteeing their accuracy in real-world scenarios. According to Masat *et al.*,[230] ML algorithms improve gas detection even at low concentrations of gases like H_2 and NH_3 by improving the performance of flexible printed sensors made from nanomaterials like graphene. These studies' application of ML enables better sensor calibration and predictive maintenance, guaranteeing peak performance over time.

To enable a smart sensing platform, Huang *et al.*[238] used ML to detect some toxic gases widely used in industrial operations, including NH_3 and phosphine (PH_3), with excellent sensitivity and selectivity. Even though the development of sensors has advanced significantly, certain obstacles still need to be overcome, such as the requirement for high operating temperatures and difficulties with selectivity and sensitivity. They presented an overly sensitive and accurate method for detecting and identifying NH_3 and PH_3 at room temperature using a graphene nanosensor, which was successfully exfoliated and effectively modified with a copper phthalocyanine derivative. The nanosensor with advanced ML shows exceptional performance in identifying gases at extremely low concentrations. For example, while it can accurately detect 100 ppb NH_3 with 100% accuracy, sensitivity, and specificity, the detection of 100 ppb PH_3 has a relatively small accuracy, sensitivity, and specificity of 77.8%, 75.0%, and 78.6%, respectively. The molecular dynamics simulation resulted in the modified graphene surface facilitating the adsorption of ammonia because of hydrogen bonding interactions, as shown in Fig. 24a and b.

5.3. Internet of Things

Gas sensing systems that incorporate IoT technologies build scalable, real-time networks for ongoing data analysis and environmental monitoring. According to Kul *et al.*,[227] IoT made it possible for TiO_2-based CO_2 sensors to send real-time data to cloud-based platforms such as ThingSpeak. This enabled remote monitoring and prompt action if CO_2 concentrations surpassed acceptable limits. In both residential and commercial settings, this Internet of Things-enabled system enhanced air quality management. Real-time gas level monitoring was made possible by IoT applications in MEMS-based sensors in the work of Mei *et al.*[245] Data transmission capabilities for predictive maintenance guarantee that the sensors continue to function at their best over time. Similar to this, Gu *et al.*[246] described how IoT integration with wearable hydrogen sensors allowed for continuous monitoring in smart clothing. Data from sensors powered by triboelectric textiles is sent to cloud platforms, allowing for the real-time detection of hazardous gas levels. Masat *et al.*[230] highlighted how flexible printed gas sensors can be made more functional by IoT technologies, enabling them to monitor multiple gases at once and send data for analysis and prompt action. By fusing real-time sensor data with cloud-based analysis, IoT can further enhance gas recognition in the work of Boonthum *et al.*,[228] enabling remote detection and management of gas hazards in settings like manufacturing plants and medical facilities.

The incorporation of Arduino microcontrollers results in the creation of a robust and user-friendly platform for processing sensor signals, collecting data, and transmitting information.[237] Because of their scalability, simplicity, and ease of customization, gas sensor systems based on Arduino are suited for experimentation and deployment in a wide variety of applications, as shown in Fig. 25a and b.[247] IoT has become increasingly widespread in various fields, including biomedical healthcare applications, heavy traffic monitoring using global positioning systems (GPSs), smart farm formation in agriculture, hospitality interconnected through smart mobile-based automation, a smart grid for wind and solar energy-saving applications, electric vehicles and drone parameter measurement and control applications, transport vehicle locations such as trucks, cars, trains, planes, and boats, smart cities, smart home automation, safety, vigilance, or security systems, and camera operation.

The ESP32 and ESP8266 stand out in IoT applications for monitoring and controlling gas and VOC sensors in residential and commercial buildings. They are equipped with Wi-Fi and Bluetooth, which makes them ideal for real-time monitoring over wireless networks.[248] Toxic gases that can seriously endanger human health, such as CO_2, CH_3, or VOCs, can be detected using these microcontrollers.[249] When dangerous gases are detected, they are frequently integrated into smart home systems in residential buildings to monitor air quality and automatically start ventilation systems or send out alerts. These platforms can be utilized in industrial settings to deploy distributed monitoring systems that cover wide areas to identify toxic gas leakage, thereby improving safety and adhering to environmental regulations. The ESP32 and ESP8266 are being utilized more frequently in biomedical applications in healthcare settings where patients with respiratory problems depend on good air quality or in sterile areas that need close supervision.

For gas sensing in both home and commercial applications, the Raspberry Pi Pico and Raspberry Pi Pico W offer affordable options.[250] These platforms can interface with a wide range of gas sensors due to their user-friendliness and availability of GPIO pins. For data transmission and remote monitoring essential in IoT-enabled smart homes, Pico W adds Wi-Fi capabilities. They can be used, for instance, to monitor the quality of the air indoors and, when gas levels rise above safe limits, activate ventilation or air purification systems.[251] The Raspberry Pi Pico can gather data from gas sensors in an industrial setting and send it to central systems for analysis and decision-making. These boards can be used in affordable medical devices that monitor the quality of the air in hospitals and other sensitive areas, providing a safe and healthy environment for patients, particularly those who are susceptible to respiratory complications.

The Raspberry Pi Zero, Pi 3, and Pi 4 are compact single-board computers (SBCs). Higher computational power makes them perfect for more intricate gas monitoring systems where real-time processing of data from several sensors is required.[252] These cutting-edge platforms enable the integration of ML models for the analysis of gas and VOC data, identifying patterns and possible dangers before they arise, such as increasing concentrations of toxic gases. These boards can serve as central hubs in commercial and residential buildings,

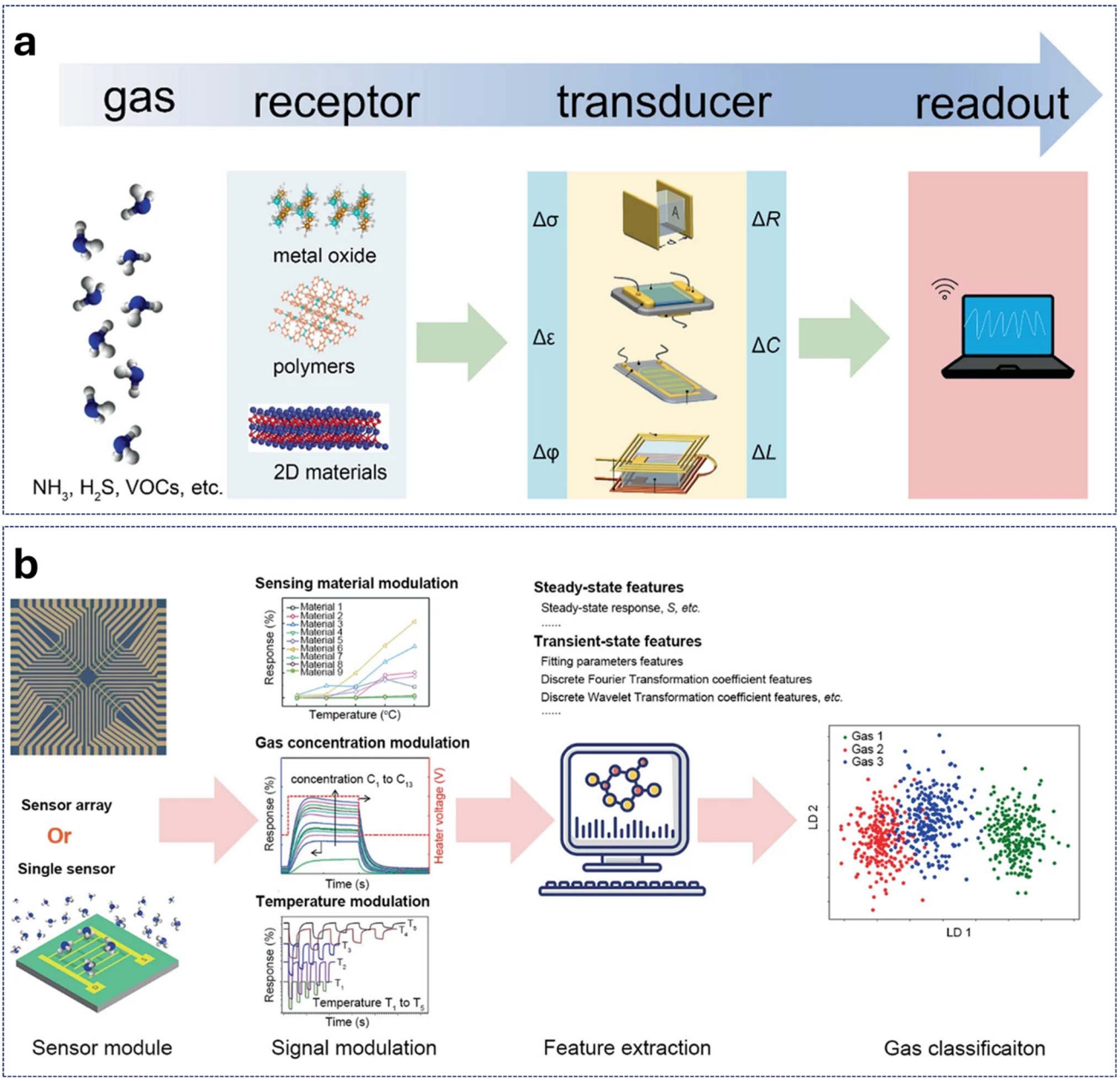

Fig. 25 IoT gas sensing and e-nose system components with analysis. (a) The diagram shows the full system of IoT gas sensing, which is composed of gas, receptor, transducer, and readout (reprinted with permission,[237] Copyright 2023, Springer Nature); (b) main components in the e-nose system, including sensor module, signal modulation, feature extraction, and machine learning classification analysis, and gas sensing signal modulation techniques consist of sensing material modulation methods, gas concentration modulation methods, and operating temperature modulation methods (reprinted with permission,[237] Copyright 2023, Springer Nature).

processing data from gas sensors and managing various systems like emergency alerts and air conditioning. The Raspberry Pi 3 and 4 can be used in medical settings and sensitive manufacturing to track the quality of the air in clean rooms or operating rooms, where preventing and detecting dangerous gases or VOCs is essential for patient safety. Their capacity to manage intricate calculations makes them perfect for creating sophisticated biomedical monitoring systems that can instantly notify medical personnel about air pollution in dangerous situations.

For low-power and real-time gas monitoring systems, PIC, AVR, Arduino, ATtiny, and STM32 microcontrollers are particularly well-suited.[253] In industrial gas sensing systems, where robustness and dependability are crucial for identifying toxic gases in dangerous settings like factories or chemical plants, PIC and AVR microcontrollers are frequently utilized.[254–256] In homes, gas detection systems such as carbon monoxide detectors or smart HVAC units that automatically modify the air quality frequently use Arduino and ATtiny.[257,258] STM32 microcontrollers are ideal for both residential and commercial

buildings due to their effective power management and powerful processing capabilities. They also offer cutting-edge features like edge computing for quicker real-time responses. These platforms can be integrated into portable medical equipment used in healthcare settings for biomedical applications, guaranteeing patient safety in settings where air purity is critical. These microcontrollers provide flexible and scalable solutions for IoT-based gas and VOC sensing systems, whether the application is to detect hazardous gases or guarantee clean air in delicate medical environments.[259]

To the best of our knowledge, monitoring several parameters in industrial environmental processes, including toxic gases, is crucial. The study of Arivalahan *et al.*[260] utilizes an Arduino-based microcontroller to monitor and measure environmental process parameters using IoT or cloud-based automation. Then, they examined the resulting data using mobile phones, laptops, or tablets. The process parameters used for the study include temperature, humidity, pressure, smoke and flame, CO, and others. An Arduino-based microcontroller monitors and measures these parameters within the IoT framework.

5.4. Solar cells and supercapacitors

The incorporation of solar cells facilitates energy extraction to power autonomous and self-sustaining gas sensor systems. Gas sensors driven by solar energy provide enhanced mobility, adaptability, and durability, enabling their use in distant or off-grid areas where traditional power sources are not accessible or unfeasible.

The integration of micro-supercapacitors (μSCs) presents energy storage methods that efficiently address power fluctuations and enhance system stability.[261,262] Supercapacitor-based gas sensor systems offer several benefits, including rapid response times, prolonged operational lifespans, and enhanced performance under demanding working conditions. These factors make them very appropriate for high-severity industrial and environmental monitoring procedures. The hybridization area that includes gas sensing and solar cells is a current trend in IoT technology. We hope that more research papers will be published soon, as solar cells are essential for increasing the sustainability of IoT devices. However, the use of screen-printing technology in this field is limited. Therefore, in all the work on the integration of different devices, the researchers used other techniques, although screen printing has high scalability and high performance.

For example, spray printing technology was employed by Ma *et al.*[263] to fabricate a full system capable of connecting the converted solar energy stored in the μSC. The proposed system includes a monolithically planar, highly flexible, and self-sustaining sensor system. This system consists of a mounted solar cell and a printed NH_3 gas sensor, both located on the same side of a single flexible substrate. The self-sustained sensor system demonstrates a notable level of sensitivity in detecting NH_3, exhibiting a commendable response rate of 18.3% at a concentration of 20 ppm. Furthermore, it demonstrates linear sensitivity when subjected to a range of 2–20 ppm. This system provides efficient electricity to operate microelectronics for NH_3 gas detection. Hence, the incorporation of printed planar devices and integrated systems presents a novel opportunity for the development of flexible microelectronics.[263]

Another example is the scalable fabrication of a self-powered integrated system of dual-channel gas detection constructed by Shi *et al.*[264] In this study, they presented the successful development of scalable, in-plane, microscale, self-powered integrated systems. These systems include Si-based photovoltaics for generating electricity, graphene-carbon nanotube micro-supercapacitors (μSCs) for storing energy, and dual-channel gas sensors that can quickly and accurately sense NH_3 and aniline. The construction of these systems was done by implementing a novel continuous centrifugal coating strategy. According to their results, the created graphene-carbon nanotube (G-CNT) films exhibited high conductivity and can serve as patterned microelectrodes for embedding μSCs and as metal-free interconnects for the circuit. This unique combination of properties enhances the integrity and flexibility of self-powered systems. The self-powered gas detection system demonstrated exceptional performance, with a response rate of 20% at a concentration of 100 ppm, and exhibited optimum linear sensitivity for detecting NH_3 and aniline within the range of 25 to 100 ppm. Hence, their study opens the door to a new pathway for the large-scale production of hybridization and self-powered multi-functionally sensitive systems in the field of flexible electronics.

Finally, according to the work of Guo *et al.*,[265] chemical etching is one of the techniques used to fabricate an integrated self-powered system of solar cells and NO_2 gas sensors. They presented a gas-sensing device that uses a single-walled carbon nanotube (SWCNT) film with excellent flexibility and a substantial surface area to detect a specific gas. A SWCNT/silicon heterojunction solar cell powers the sensor, consistently providing a voltage of approximately 0.5 V when exposed to standard solar intensity. The self-powered sensing system has an optimal rectangular nitrogen dioxide detection curve, superior sensitivity, and a quicker response time compared to an externally powered system operating at ambient temperature. The utilization of SWCNTs in both the sensing and powering stages results in increasing carrier concentration, which is responsible for enhancing sensitivity. Ultimately, the gas sensing system demonstrated a wireless connection with a phone using a Bluetooth Low Energy Module (BLEM) as a full system.

To the best of our knowledge, the majority of the integrated systems in the literature are fabricated using inkjet, spray, and chemical etching, although screen printing is the most scalable technology and can make an accurate printed film. It is important to mention that the literature is limited by the constraints of publishing with this technology.

5.5. Triboelectric nanogenerators (TENGs)

The integration of nanogenerators enables the development of autonomous gas sensor systems that can effectively utilize ambient mechanical or thermal energy.[266–269] Nanogenerator-

based gas sensors offer energy-efficient capabilities, reduce environmental consequences, and improve self-reliance, making them suitable for wearable and portable applications where battery replacement or recharging is impractical. In their study, Mohamadbeigi *et al.*[270] constructed a self-powered breath sensor to detect ethanol levels in exhaled human breath. The sensor utilized a composite nanofiber material consisting of polyethylene oxide (PEO) and copper(I) oxide, along with a TENG, which is composed of fluorine-doped tin oxide (FTO) and PI, as the power source. Detecting the concentration of ethanol in exhaled breath has the potential to be a biomarker for the early identification of lung cancer. Nevertheless, the existence of interfering substances such as methanol and acetone, along with the increased levels of humidity in exhaled air, requires the development of a sensor that exhibits a strong preference for ethanol and maintains stability under high humidity conditions. The performance of the polyethylene oxide/copper(I) oxide composite nanofiber (PCNF) sensor was evaluated in three distinct environments: high humidity, pure ethanol, and ethanol with a relative humidity of 90%.[270]

In addition to that, Zhu *et al.*[226] developed a self-powered inkjet printed H_2 gas sensor driven by a nanogenerator on a textile substrate, in which the sensing material was reduced to graphene oxide (rGO) and Pd nanoparticles. The graphene

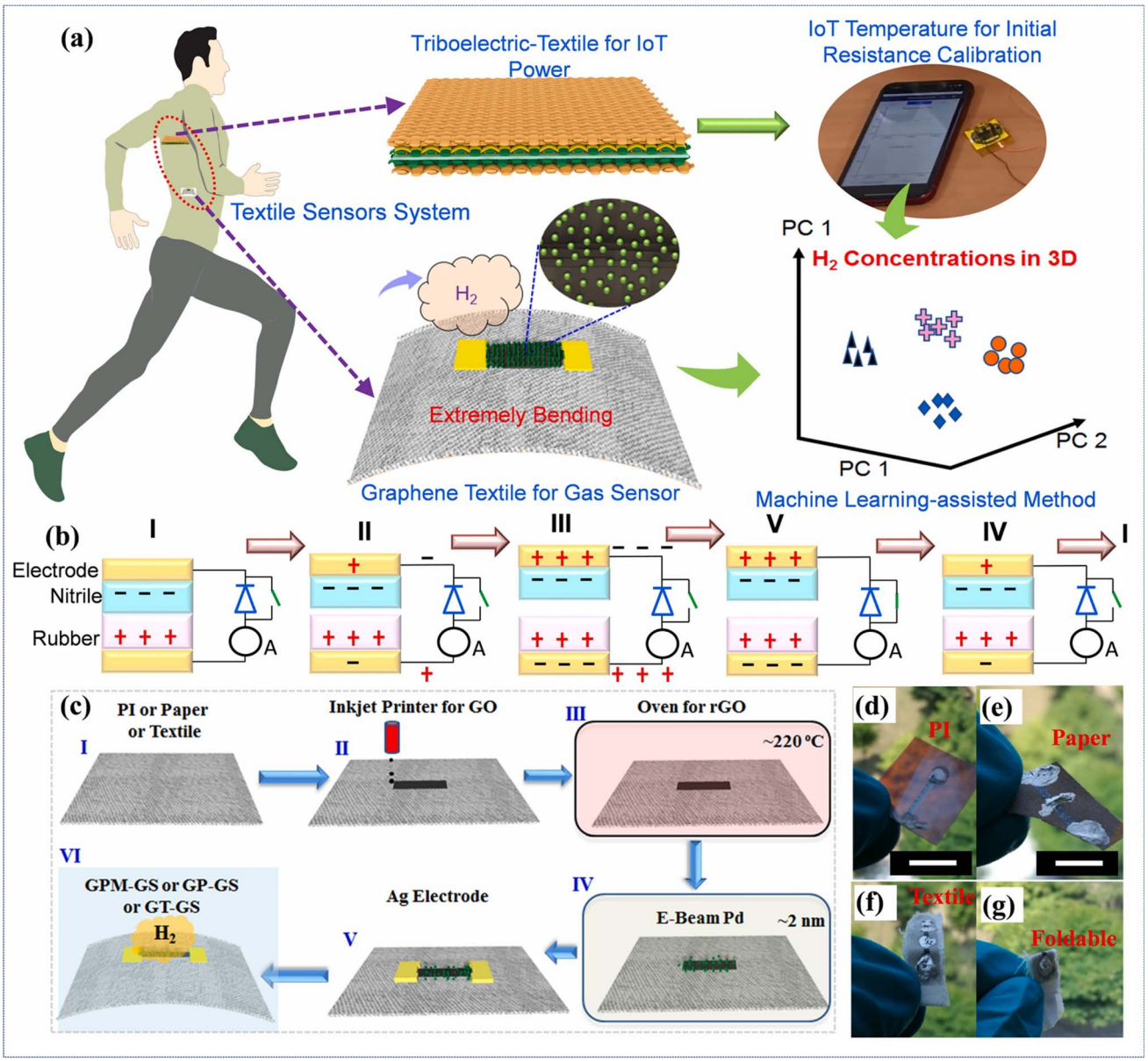

Fig. 26 IoT gas sensing: ML-powered, triboelectric textiles, and graphene sensors. (a) The machine learning-PCA method for all textile-based systems using both triboelectric-textiles to power sensor nodes (humidity and temperature) and the textile graphene gas sensor in an extremely deformed environment; (b) the principle of the triboelectric effect of triboelectric textiles; (c) gas sensor manufacturing; (d–g) optical images of graphene on different substrates such as PI, paper, and textile, and foldable test of the textile gas sensor (reprinted with permission,[226] Copyright 2021, Elsevier).

textile gas sensor (GT-GS) had a detection response that was about six times better than that of the graphene PI membrane gas sensor. This is mostly because the textile substrate has a larger surface area. The analysis of the impact of temperature on the GT-GS reveals that the response of H_2 gas is more favorable at ambient temperatures compared to elevated temperatures, such as 120 °C. Furthermore, the use of ML-enabled technology and triboelectric-based textiles for IoT purposes, specifically in temperature and humidity calibration of gas systems, has led to the recognition of H_2 as a suitable material for wearable applications that possess strong mechanical properties such as flexibility and foldability, as shown in Fig. 26a and g.

5.6. Incorporation of heaters

By incorporating microheaters, the temperature may be precisely regulated and adjusted, leading to enhanced gas-sensing capabilities.[101] Microheater-equipped gas sensors offer improved sensitivity, selectivity, and stability, rendering them well-suited for gas detection applications that need precise temperature control or operation under challenging environmental conditions, as shown in Fig. 27.[168] The in-vehicle wireless driver breath alcohol detection (IDBAD) system was created by Ansari *et al.*,[271] utilizing Sn-doped CuO nanostructures. When the system identifies the presence of ethanol in the driver's exhaled air, it can generate an alarm and subsequently halt the ignition of the vehicle. Additionally, it can transmit the precise location of the car to the user's mobile phone. The sensor employed in this system is a resistive ethanol gas sensor integrated with a two-sided micro-heater, which is constructed using Sn-doped CuO nanostructures. The findings exhibited a notable enhancement in sensor efficacy by Sn doping into CuO nanostructures. The gas sensor under consideration exhibits rapid response, excellent repeatability, and high selectivity, rendering it well-suited for practical applications, including the suggested system.

6. Current challenges and future improvements

Screen-printed toxic gas sensors for various gaseous substances, including NO_2, CO_2, CO, SO_2, H_2, H_2S, NH_3, LPG, and VOCs, encounter many obstacles that impede their extensive implementation and effectiveness in practical scenarios.[37,74,272] One notable barrier is achieving elevated sensitivity and selectivity over a wide range of target gases while maintaining low detection limits. Cross-sensitivity to other NO_x or environmental interference can limit the accuracy of NO_2 sensors, giving rise to misleading results. CO_2 sensors also have the challenge of being cross-reactive with other gaseous substances often present in indoor settings, such as VOCs. This cross-reactivity can lead to inaccurate results and undermine the accuracy of air quality evaluations. LPG gases, such as propane and butane, are difficult to detect due to their small presence and susceptibility to overlapping with other gases. Therefore, it is necessary to enhance the design and calibration methodologies of sensors to overcome these hurdles.

Furthermore, ensuring sensor stability and dependability for long periods is a significant obstacle. For example, H_2S sensors can deteriorate over time if exposed to severe environmental conditions or contaminated by sulfur-containing substances.[74] This can cause a shift in the sensor's response and a decrease in

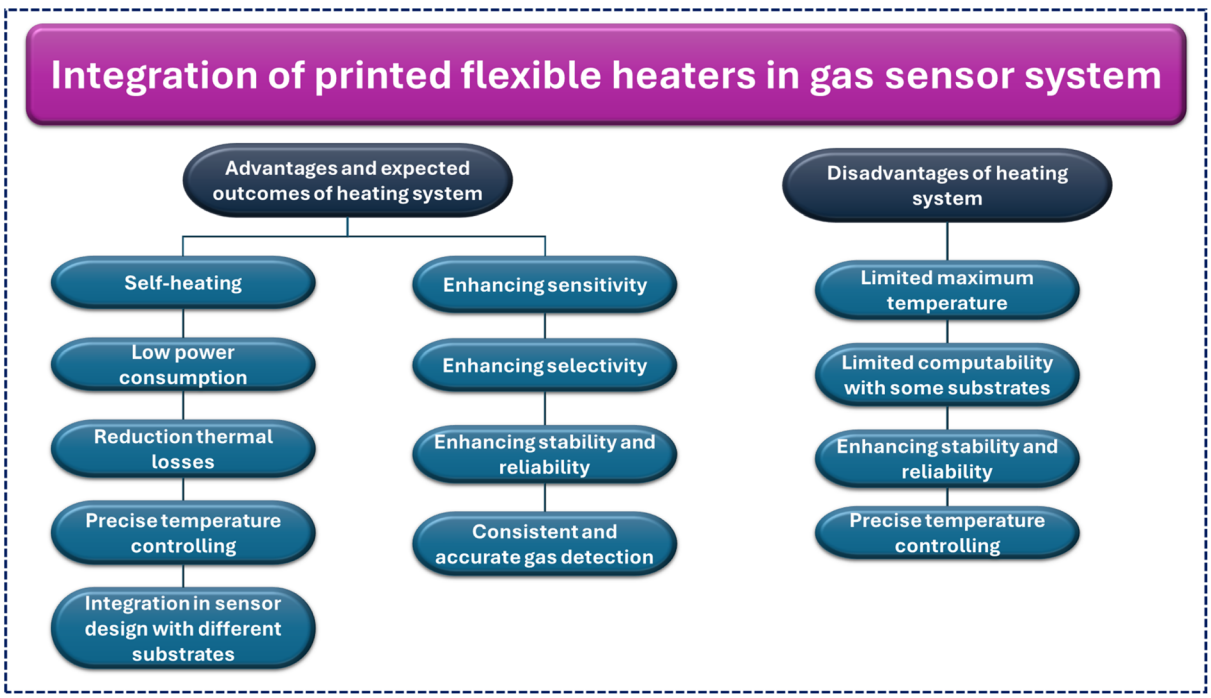

Fig. 27 Schematic diagram presenting the advantages and disadvantages of integration of printed flexible heaters in a gas sensor system.

its accuracy. Dampness or acidic gases can also interfere with the performance and lifespan of NH_3 sensors. To overcome these obstacles, durable sensor materials and coatings, along with efficient calibration and maintenance procedures, are necessary. Another issue, which is one of the most recent challenges, is that fully printed gas sensor circuits are crucial for creating flexible miniaturized IoT devices that can be applied in different industrial fields or indoor networks, as shown in Fig. 28.

One additional obstacle is the ability to downsize and integrate sensor components while maintaining optimal performance. VOC sensors ought to strike a balance between sensitivity and response time while also considering compact size and low power consumption, particularly in the context of wearable or portable devices. Similarly, the incorporation of energy-collecting technologies such as solar cells or TENGs into gas sensor systems presents challenges in terms of power control, energy effectiveness, and system integration.[273] To get the most out of screen-printed toxic gas sensors, these problems must be solved through collaborative research projects and technological advances that make the sensors more useful, dependable, and effective in real life. CO_2 is still one of the gases that need investigations to detect it in a normal environment. However, some researchers used a smart mask system to detect, as shown in Fig. 29a–c.

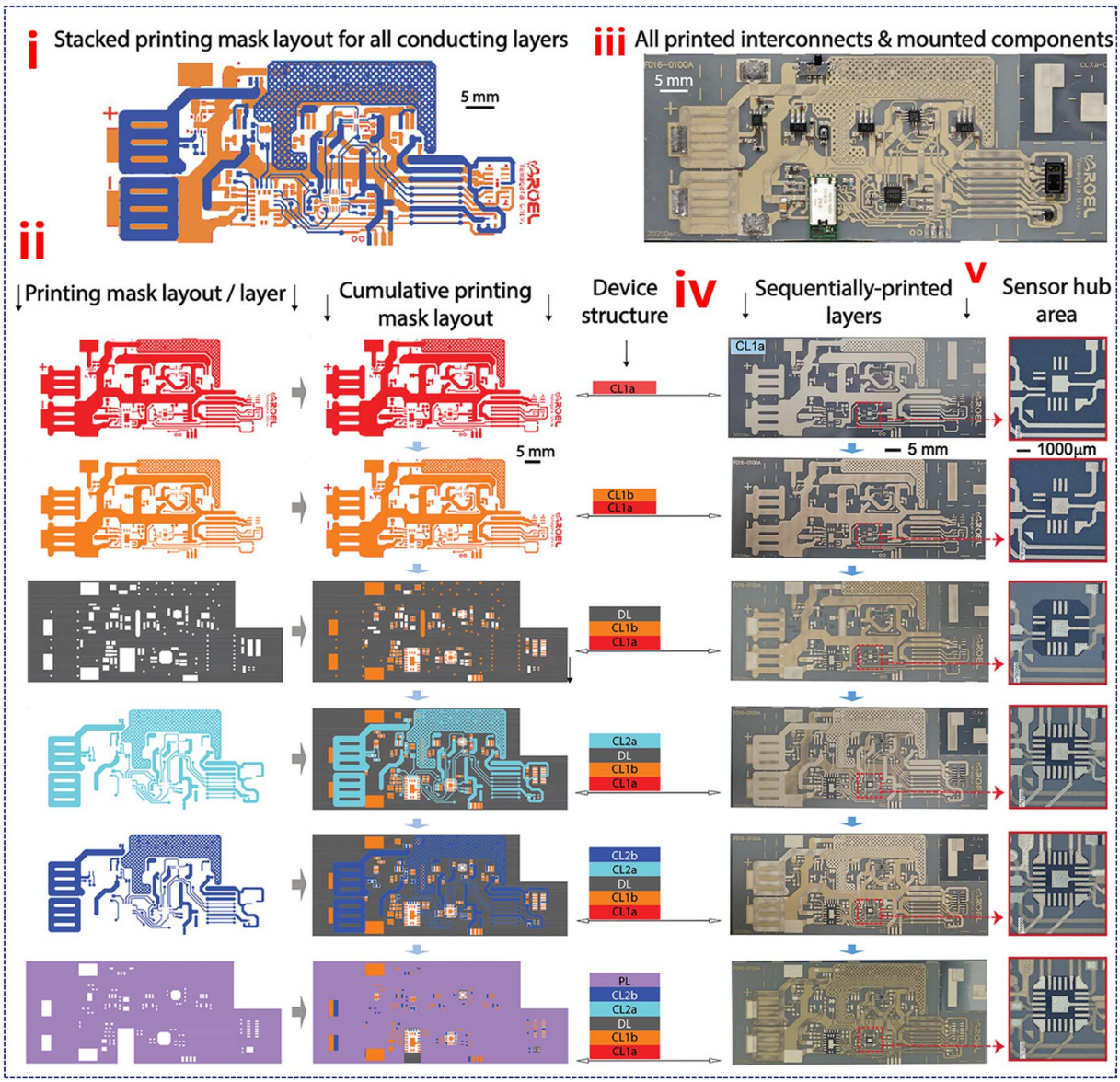

Fig. 28 Multilayer FHE device: printing masks, sequential layers, and microscopy. (i) Stacked printing mask layouts for all conducting circuitry layers, (ii) single layer (left) and cumulative (center) printing mask layout, and device structure (right) for the sequential printing of two conductive, a dielectric, two conductive and a passivation layer, (iii) photograph of the complete FHE device with mounted chips and electronic components of (i), (iv) photographs of sequentially printed layers after annealing of (ii), and magnified photographs of the interconnect circuitry in the sensor hub area corresponding to (v) taken by optical microscopy (reprinted with permission,[58] Copyright 2023, Wiley).

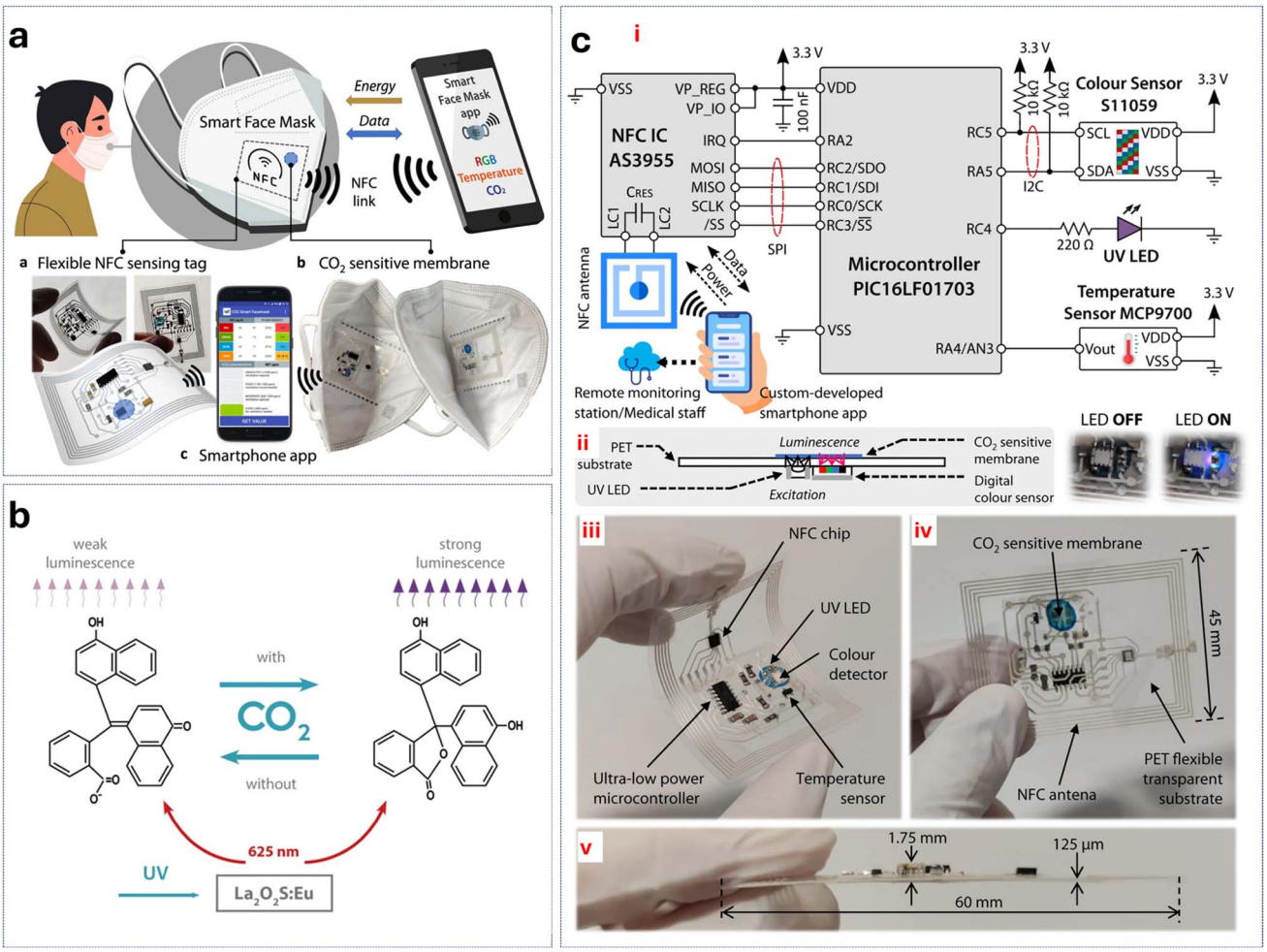

Fig. 29 Flexible NFC sensor: CO_2 detection, smartphone integration, and fluorescence mechanism. (a) The flexible tag's CO_2-sensitive membrane, mounted on the inside layer of a typical FFP2 facemask, the tag provides power and bidirectional communication through a custom smartphone app (reprinted with permission,[189] Copyright 2022, Springer Nature); (b) CO_2 sensing mechanism (reprinted with permission,[189] Copyright 2022, Springer Nature); (c) (i) NFC tag circuit diagram for wireless CO_2 reading, (ii) a schematic of an ultraviolet LED and color sensor positioned in front of a CO_2-sensitive membrane, and the right photo shows LED-on UV excitation and red fluorescence, and (iii, iv and v) the photos of the flexible tag on a 125 micrometer PET substrate (reprinted with permission,[189] Copyright 2022, Springer Nature).

The potential for significant progress in the field of screen-printed toxic gas sensors, specifically designed to detect various gases such as NO_2, CO_2, CO, SO_2, H_2, H_2S, NH_3, LPEG, and VOCs, holds great promise for environmental monitoring and enhancing industrial safety. The incorporation of nano-scale materials, such as metal oxides, metal sulfides, graphene, doped and undoped reduced graphene oxide (rGO), conducting polymers, carbon nanotubes (CNTs), or quantum dots, in nanomaterial integration can provide a viable method that can improve sensitivity and selectivity.[37] Nanomaterial incorporation can enhance the surface area available for gas adsorption and can be designed to deliver distinct chemical characteristics, thus enhancing the sensor's capacity to identify and distinguish various harmful gases. A great attempt was reported by Yoshida *et al.* to detect the heart rate (HR) and pulse oximetry, which is a technique to estimate peripheral (di) oxygen saturation (SpO_2), as shown in Fig. 30a–c, but the literature remains limited in terms of designing such circuits for gas sensors.[35]

Functional coatings offer a promising opportunity for enhancing screen-printed gas sensors in the future, as presented in Fig. 31. The enhancement of sensor selectivity and reduction of cross-sensitivity to interfering gases can be achieved through the development of unique coatings that possess customized chemical capabilities by using hybrid printing technology, such as inkjet printing (IJP). These coatings exhibit a selective interaction with specific gas targets, thus enhancing the precision and dependability of detection processes. Furthermore, the progress made in smart sensing systems, which incorporate AI and ML algorithms such as PCA, presents prospects for the analysis of data in real-time, the identification of patterns, and the ability to adjust calibration accordingly. Intelligent sensing systems can facilitate the ability of sensors to adjust to dynamic environmental circumstances, enhance operational efficiency, and will also offer practical insights to end-users, resulting in enhanced gas monitoring solutions.

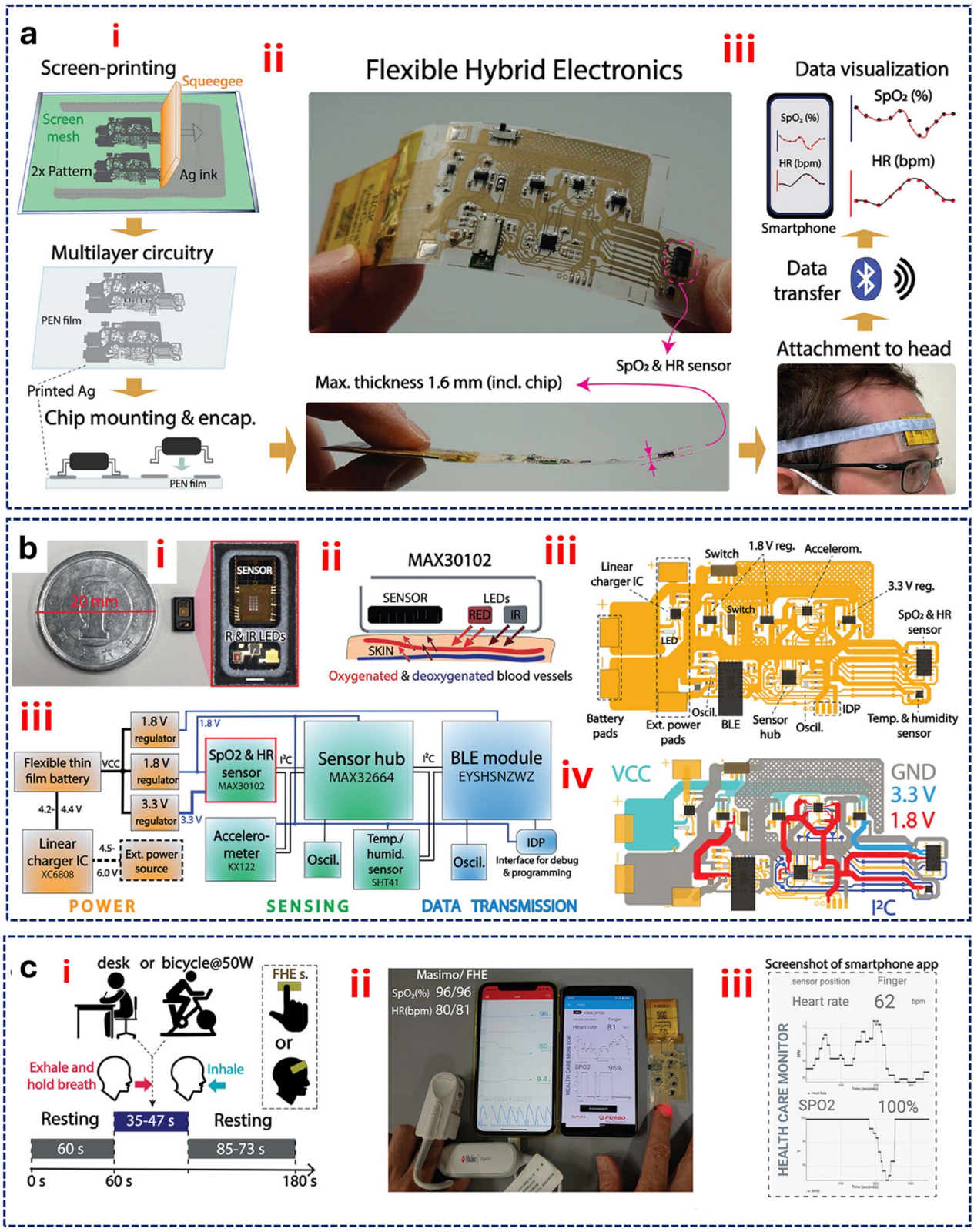

Fig. 30 FHE device: multilayer printing, wearable vital sensor, and wireless monitoring (a). (i) A graphical representation depicting the process of preparing an FHE device by multilayer screen-printing of the circuitry and mounting electronic components, (ii) the provided photographs present the complete FHE device in two views: a slightly tilted top view in its bent state (top) and a side view (bottom), and (iii) the application of the FHE system is illustrated as a wearable vital sensor worn on the forehead (bottom, photograph), with the wireless transfer of the measured vital signals to a smartphone and subsequent visualization on a display (top, graphical illustration); (b) the overall design, system architecture, and sensing principle of the FHE gadget: (i) an optical microscope-taken photo of the SpO_2 and HR sensing chip magnified with a scale bar of 500 μm, (ii) a graphical representation of the sensing principle when the sensor comes into contact with human skin, and (iii) an integrated circuit layout of the FHE system that shows connections with yellow-orange and electronic components with black-grey colors when the signal pathways are (iv)

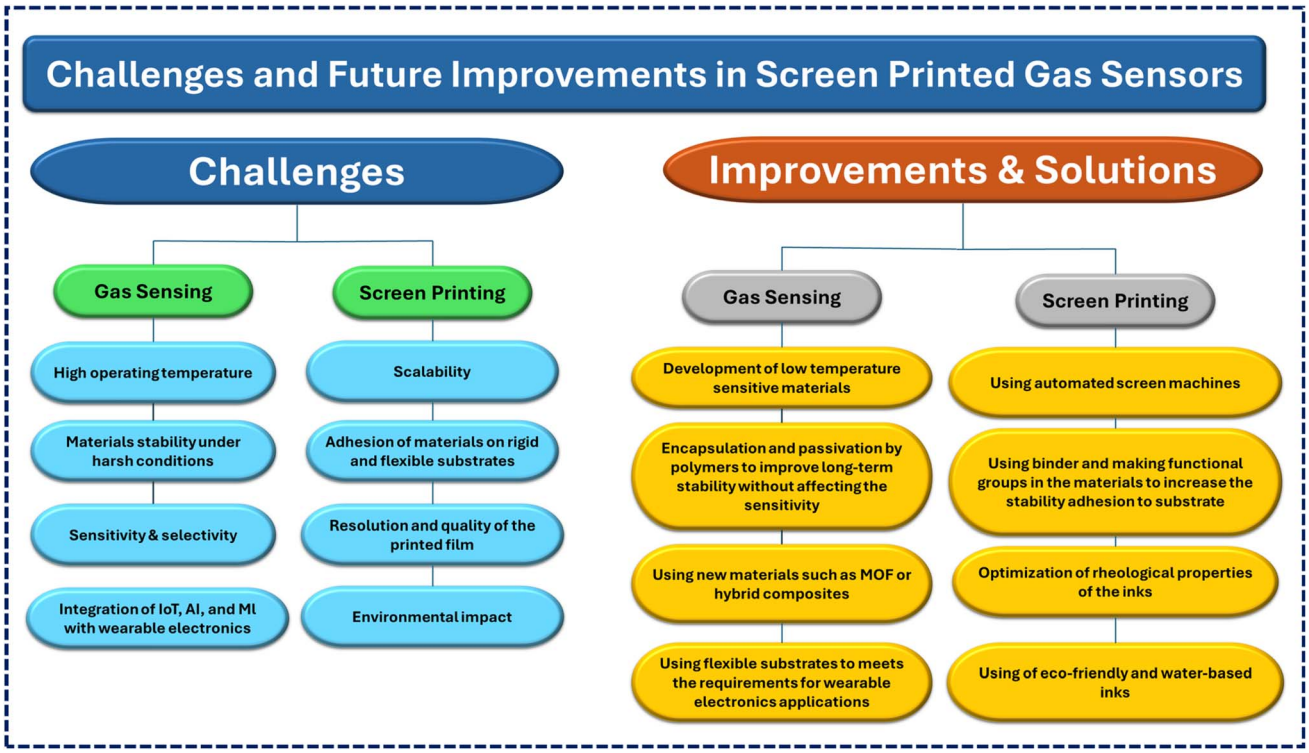

Fig. 31 Schematic diagram presenting the challenges and future improvements in screen-printed gas sensors.

In addition, the incorporation of multi-sensor arrays and microfluidic systems has the potential to enhance the functionalities of screen-printed gas detection.[274] Microfluidic gas sensors can continuously detect the molecules released by explosions, dangerous airborne substances, and environmental pollutants at low concentrations.[275–277] To extend more, microfluidic system in gas sensor applications can enhance sensitivity and selectivity enabling to detect the small quantity of toxic gas such as H_2S and CO.[277,278] Multi-sensor arrays can be used for duplicate measurements and cross-validation. The incorporation of microfluidics can enable the controlled delivery of samples, diffusion of gas, and concentration of analytes. Future improvements in microheaters and screen-printed gas sensors necessitate advancements in energy harvesting technologies, flexible and wearable designs, and environmental stability. These factors are essential for enabling autonomous operation, portability, and long-term reliability in diverse applications.[98,101] For insight into the gas sensor performance, Table 2 lists the comparison results of the sensitivity, response, and recovery time of some gas sensors fabricated using screen printing technology and other technologies.

7. Summary and conclusion

The rapid advancements in screen-printing technology have established it as a pivotal method for the fabrication of cost-effective and versatile toxic gas sensors. By enabling precise deposition of functional materials onto diverse substrates, screen printing has transformed the landscape of gas sensor development, offering scalability and economic feasibility. This review has extensively explored fabrication techniques, including traditional screen printing, thick-film printing, and hybrid approaches, showcasing their foundational principles, applications, and benefits. Furthermore, the integration of emerging technologies such as artificial intelligence (AI), machine learning (ML), micro-supercapacitors (μSCs), photovoltaic (PV) systems, triboelectric nanogenerators (TENGs), and microheaters has demonstrated a transformative impact on the performance and functionality of gas sensors. The incorporation of AI and ML algorithms has revolutionized gas sensing by enabling real-time data analysis and pattern recognition, leading to enhanced precision, adaptability, and decision-making capabilities. These technologies empower sensors to

not distinguished and (v) highlighted signal pathway in colors (reprinted with permission,[58] Copyright 2023, Wiley); and (c) the evaluation of the vital sensing functionality of the FHE device under both normal and hypoxic conditions, while also scrutinizing the wireless signal transfer: (i) a diagram illustrates the testing method and the locations where the FHE device attaches to the human body, (ii) a photograph shows the FHE device wirelessly transmitting real-time SpO_2 and HR data to a smartphone. Finger contact on the sensor acquires the data. The photograph also includes a comparison of the same measurement taken with a commercial device (Masimo $iSpO_2$): (iii) the photo of the smartphone displaying the wirelessly SpO_2 and HR data transmitted from the FHE device as the sensor collected the data by means of finger contact (reprinted with permission,[58] Copyright 2023, Wiley).

Table 2 Sensing performance of screen-printed sensors

No.	Target gases	Materials	Print technique of active materials	Substrates	Electrodes/printing techniques	Gas concentration	Sensitivity	Response/recovery time (s)	Operating temperature (°C)	Flexibility	Sense type	Ref.
1	NH_3	MWCNT-PEDOT:PSS	Screen printing	Polyethylene terephthalate (PET)	Ag/screen printing	80 ppm	67.5%	228/540	Room temperature	Flexible	Chemiresistive	41
2	O_2	Au	Screen printing	Porous PTFE	Ag and CNT/screen printing	12.6%	0.09651 μA/[$\%O_2$]	14/—	Room temperature	Flexible	Electrochemical	61
3	C_2H_5OH	Fe_2O_3-$LaFeO_3$-La_2O_3 (Gd)	Screen printing	Alumina	Ag/screen printing	300 ppm	427%	—	319	Rigid	Chemiresistive	117
4	HCHO and NH_3	CeO_x-$La_xBa_{1-x}SnO_{3-\delta}$	Screen printing	Corning glass substrates	—	50 ppm	65	75/60	Room temperature	Rigid	Chemiresistive	92
5	NH_3	PANI	Electrodeposition	Ceramic	Commercial gold–silver/screen printing	1 ppm	4.27 ppm^{-1}	312/—	Room temperature	Rigid	Electrochemical	126
6	HCHO and NH_3	ZnO	Screen printing	Corning glass substrates	—	5 ppm and 10 ppm	336	69/138	500	Rigid	Chemiresistive	114
7	Furaneol	AgNP-ME and CNT-ME	Screen printing	Polyethylene terephthalate (PET)	—	—	1 fM–35 μM	—	Room temperature	Flexible	Electrochemical	214
8	NO_2	Zn doped In_2O_3	Screen printing	Alumina	—	100	116.8	—	50	Rigid	Chemiresistive	36
9	H_2S	CeO_2/rGO-3	Drop casting	Alumina	Ag/screen printing	1–50 ppm	97.41	9/12	Room temperature	Rigid	Grain-based	90
10	VOC and NO_2	$Co^{2+}SnO_2$	Screen printing	Glass substrate	—	500 ppm	69.30% 80.24%	(24/54 VOC) (22/54 NO_2)	250 200	Rigid	Chemiresistive	56

dynamically learn from their environments, making them robust against interference and fluctuations. Similarly, advancements in energy technologies, such as μSCs and TENGs, address critical issues related to sensor autonomy and environmental sustainability. These devices not only reduce dependency on external power sources but also align with green energy goals by making sensors self-powered and eco-friendly.

Microheaters have further expanded the utility of screen-printed sensors, particularly under challenging conditions where temperature control is critical for response accuracy. By integrating precise thermal management, sensors can maintain consistent performance, even in environments with high variability. Most printed gas sensor prototypes recently created in research labs are designed as single-output sensors. A major obstacle to transitioning these sensors from research to industrial production is their limited ability to detect different gases selectively. While the introduction of sensor arrays in recent years has helped address this issue, challenges such as sensor drift and inconsistent performance in the presence of unknown interferences remain significant barriers. Despite these advancements, challenges such as limited sensitivity, poor selectivity, and environmental instability continue to impede the widespread adoption of screen-printed gas sensors. The presence of unknown interferents, sensor drift, and degradation under harsh conditions highlight the need for innovative materials and robust engineering solutions.

While screen-printing technology has democratized the fabrication of gas sensors, its reliance on conventional materials and manufacturing methods limits its potential for breakthrough innovation. For instance, the performance of sensors heavily depends on the quality and functionality of the printed inks and substrates, which often lack the desired level of reactivity or stability. Nanomaterial integration, such as the use of 2D materials, metal–organic frameworks (MOFs), and functional coatings, holds promise for addressing these shortcomings but requires a delicate balance between scalability and performance enhancement.

Additionally, the convergence of screen-printed sensors with futuristic applications, such as wearable and flexible electronics, presents exciting opportunities but also introduces complexities in mechanical durability and reliability. The push towards multi-sensor arrays and microfluidic integration for enhanced selectivity and multiplexing capabilities is a logical progression. Yet it raises questions about manufacturing consistency and cost-effectiveness at an industrial scale. Another critical issue lies in the reliance on external data infrastructure for AI- and ML-powered sensors, which could be a bottleneck in remote or resource-constrained environments. Ensuring robust, decentralized processing capabilities without compromising data integrity remains a significant challenge.

Finally, the future of screen-printed gas sensors is undoubtedly promising, with huge opportunities to revolutionize hazardous gas detection. With the introduction of materials science, process engineering, and integration with advanced technologies, these sensors can become smarter, more reliable, and environmentally sustainable. Addressing the

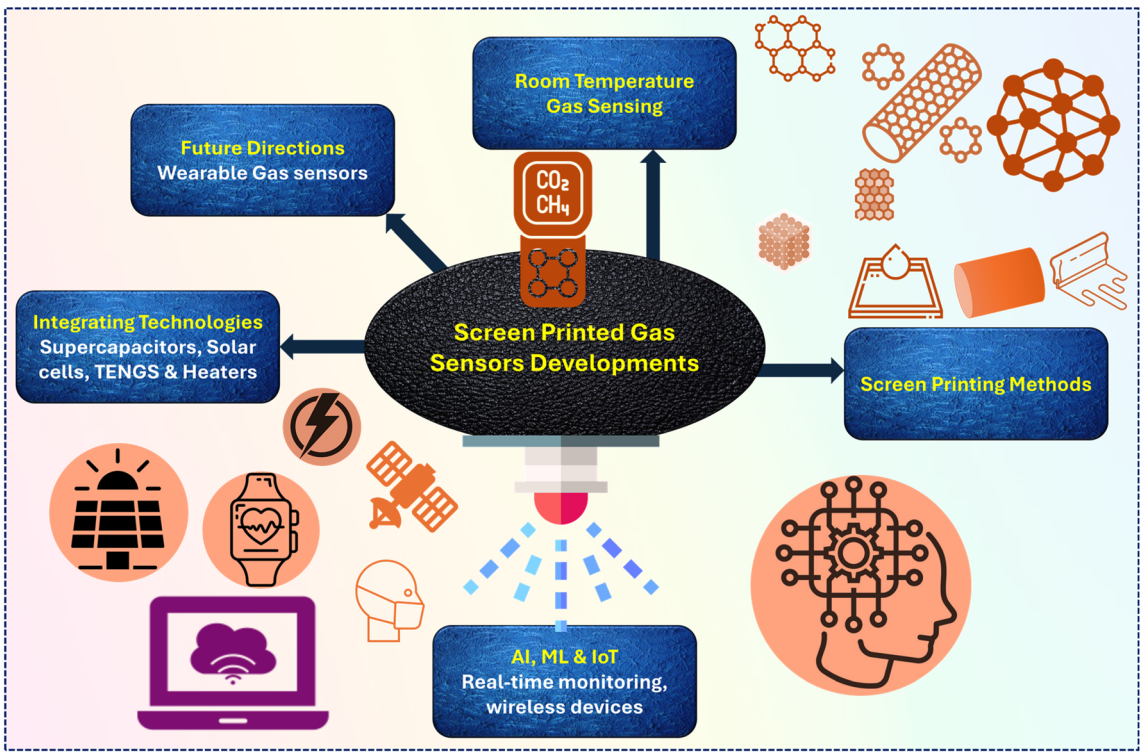

Fig. 32 Summary of screen-printed gas sensor developments, including the future direction, room temperature gas sensing, screen printing methods, AI, ML, IoT, and integrating technologies.

prevailing challenges of sensitivity, selectivity, and stability requires not only incremental improvements but also paradigm-shifting innovations in materials, design, and system-level optimization. By embracing flexible, wearable, and self-sustaining designs, the next generation of screen-printed gas sensors will find applications beyond industrial and environmental monitoring, extending into healthcare, personal safety, and smart home systems. The road ahead will depend on the synergistic collaboration of interdisciplinary fields to tackle existing limitations while unlocking the full potential of this versatile and impactful technology. Screen printing will undoubtedly remain at the forefront of the gas-sensing revolution, paving the way for a safer, healthier, and more sustainable future. An overall illustration of the recent progress made in screen-printed gas sensing technology is summarized in Fig. 32.

Data availability

The data supporting the findings of this review paper are derived from publicly available sources, which are cited in the reference section of the manuscript. All datasets analyzed and used in the study are accessible through their respective publishers or repositories. Specific data related to individual studies can be obtained from the original publications referenced. No new data were generated during this study. For further inquiries or assistance in accessing specific datasets, readers are encouraged to contact the corresponding author.

Author contributions

Mohamed Ahmed Belal: conceptualization and writing – original draft; Sugato Hajra: writing – editing and visualization; Swati Panda: writing – original draft; Kushal Ruthvik Kaja: visualization; Mohamed Magdy Mohamed Abdo: validation and writing – editing; Ahmed Abd El-Moneim: validation and writing – editing; Dawid Janas: writing – editing; Yogendra Kumar Mishra: supervision, funding acquisition, and writing – editing; Hoe Joon Kim: supervision, funding acquisition, and writing – editing.

Conflicts of interest

The authors declare no conflict of interest.

Acknowledgements

The authors would like to acknowledge the financial support from the National Research Foundation of Korea (RS-2024-00346135). YKM acknowledges the funding from the ESS lighthouse on hard materials in 3D, SOLID (Danish Agency for Science and Higher Education, grant number 8144-00002B), Denmark, TORCH: (Interreg Deutschland-Denmark and the European Union under grant number 04-3.2-232, and NANO-CHEM (national infrastructure UFM 5229-00010B, NANO-CHEM, Denmark). DJ acknowledges the support received from the National Science Center (under the OPUS program, grant agreement 2019/33/B/ST5/00631).

References

1 P. Wu, Z. Zhao, Z. Huang and M. Huang, *RSC Adv.*, 2024, **14**, 1445–1458.
2 D. Lu, L. Huang, J. Zhang, W. Zeng and Q. Zhou, *ACS Appl. Nano Mater.*, 2024, **7**, 4239–4251.
3 P. J. Landrigan, M. Britt, S. Fisher, A. Holmes, M. Kumar, J. Mu, I. Rizzo, A. Sather, A. Yousuf and P. Kumar, *Ann. Glob. Health*, 2024, **90**, 1.
4 Y. Ma, H. Xiong, L. Gan and G. Deng, *Surf. Interfaces*, 2024, **45**, 103910.
5 F. O. Okpaga, A. I. Adeolu, F. N. Nwalo, A. O. Okpe, C. C. Ikpeama and C. E. Ogwu, *Bio-Res.*, 2024, **22**, 2274–2291.
6 A. H. Nasser, L. Guo, E. L. H, Y. Wang, X. Guo, A. AbdelMoneim and N. Tsubaki, *RSC Adv.*, 2018, **8**, 14854–14863.
7 A. G. Galallah, M. K. Albolkany, A. E. Rashed, W. Sadik, A. G. El-Demerdash and A. Abd El-Moneim, *J. Environ. Chem. Eng.*, 2024, **12**, 113380.
8 T. Dogan Guzel and K. Alp, *Sci. Total Environ.*, 2024, **912**, 168996.
9 Y. Liang and S. Zhuang, *China Econ. J.*, 2024, **17**, 26–39.
10 A. E. N. Laryea, W. X. Ren, Q. Guo and Z. H. Kang, *Combust. Sci. Technol.*, 2024, 1–33.
11 S. Márquez-Sánchez, J. Huerta-Muñoz, J. Herrera-Santos, A. G. Arrieta and F. De la Prieta, *Ad Hoc Netw.*, 2023, **148**, 103205.
12 X. Song, T. Liu, K. Gu, Z. Luo and M. Zhang, *J. Alloys Compd.*, 2024, **976**, 173153.
13 K. Satyanarayana, L. R. Kumar, S. Sai Akanksha, S. Keerthana, R. K. Sahil Singh, T. Kondaiah, L. Goel, S. Dixit, P. B. Bobba, A. Perveen and S. Debnath, *MATEC Web Conf.*, 2024, **392**, 01084.
14 X. Lin, R. Yang, W. Zhang, N. Zeng, Y. Zhao, G. Wang, T. Li and Q. Cai, *Carbon Balance Manage.*, 2023, **18**, 9.
15 S. Kumar, N. Saha, A. A. Mohana, M. S. Hasan, M. S. Rahman, M. Elmes and G. R. Macfarlane, *Water, Air, Soil Pollut.*, 2024, **235**, 222.
16 S. J. Perumpully, S. Gautam, J. J. Paul and M. Sreenath, *Water, Air, Soil Pollut.*, 2024, **235**, 54.
17 S. Joseph Sekhar, M. S. Samuel, G. Glivin, T. G. Le and T. Mathimani, *Fuel*, 2024, **360**, 130626.
18 K. Pazhanivel, U. D. Kumar, K. Naveen and M. Niranjan, *Int. J. Adv. Res. Sci. Commun. Technol.*, 2023, 10–21.
19 N. K. Singh, P. K. Verma, A. L. Srivastav, S. P. Shukla, D. Mohan and Markandeya, *Sci. Total Environ.*, 2024, **921**, 171117.
20 H. E. Ahmed, M. K. Albolkany, M. E. El-Khouly and A. A. El-Moneim, *RSC Adv.*, 2024, **14**, 13946–13956.
21 M. H. Eldesouki, A. E. Rashed and A. Abd El-Moneim, *Clean Technol. Environ. Policy*, 2023, **25**, 3131–3148.
22 A. I. Sunny, A. Zhao, L. Li and S. Kanteh Sakiliba, *Sensors*, 2020, **21**, 214.
23 A. Milone, A. G. Monteduro, S. Rizzato, A. Leo, C. Di Natale, S. S. Kim and G. Maruccio, *Adv. Sustainable Syst.*, 2022, **7**, 2200083.

24 Y. Su, J. Wang, B. Wang, T. Yang, B. Yang, G. Xie, Y. Zhou, S. Zhang, H. Tai, Z. Cai, G. Chen, Y. Jiang, L. Q. Chen and J. Chen, *ACS Nano*, 2020, **14**, 6067–6075.
25 D. Y. Nadargi, A. Umar, J. D. Nadargi, S. A. Lokare, S. Akbar, I. S. Mulla, S. S. Suryavanshi, N. L. Bhandari and M. G. Chaskar, *J. Mater. Sci.*, 2023, **58**, 559–582.
26 J. Dai, O. Ogbeide, N. Macadam, Q. Sun, W. Yu, Y. Li, B. L. Su, T. Hasan, X. Huang and W. Huang, *Chem. Soc. Rev.*, 2020, **49**, 1756–1789.
27 Y. M. Jo, Y. K. Jo, J. H. Lee, H. W. Jang, I. S. Hwang and D. J. Yoo, *Adv. Mater.*, 2023, **35**, e2206842.
28 S. A. Khan, M. Saqib, M. M. Rehman, H. M. Mutee Ur Rehman, S. A. Rahman, Y. Yang, S. Kim and W. Y. Kim, *Nanomaterials*, 2021, **11**, 1815.
29 C. V. Sudheep, A. Verma, P. Jasrotia, J. J. L. Hmar, R. Gupta, A. S. Verma, Jyoti, A. Kumar and T. Kumar, *Results Chem.*, 2024, **7**, 101255.
30 K. Lee, S. Hajra, M. Sahu, Y. K. Mishra and H. J. Kim, *J. Ind. Eng. Chem.*, 2022, **106**, 512–519.
31 K. Lee, S. Hajra, M. Sahu and H. J. Kim, *J. Alloys Compd.*, 2021, **882**, 160634.
32 K. Lee, J. Park, S. I. Jung, S. Hajra and H. J. Kim, *J. Mater. Sci. Mater. Electron.*, 2021, **32**, 19626–19634.
33 K. Lee, M. Sahu, S. Hajra, K. Mohanta and H. J. Kim, *Ceram. Int.*, 2021, **47**, 22794–22800.
34 J. Park, C. Ryu, I. Jang, S. I. Jung and H. J. Kim, *Mater. Today Commun.*, 2022, **33**, 105007.
35 A. W. Rohde, J. M. Nel and T. H. Joubert, *Agriculture*, 2023, **13**, 1483.
36 S. C. Kulkarni, K. D. Bhalerao, S. Shirse, Y. T. Nakate, U. T. Nakate, B. Pandit and M. A. Yewale, *Ceram. Int.*, 2022, **48**, 29298–29306.
37 R. Sivakumar, K. Krishnamoorthi, S. Vadivel and S. Govindasamy, *Diamond Relat. Mater.*, 2021, **116**, 108418.
38 S. Hajian, X. Z. Zhang, P. Khakbaz, S. M. Tabatabaei, D. Maddipatla, B. B. Narakathu, R. G. Blair and M. Z. Atashbar, *IEEE Sens. J.*, 2020, **20**, 7517–7524.
39 G. Manjunath, P. Nagaraju and S. Mandal, *J. Mater. Sci. Mater. Electron.*, 2020, **31**, 10366–10380.
40 J. P. P. Rajakumar and J. H. Choi, *Sensors*, 2023, **23**, 1590.
41 D. Boonthum, C. Oopathump, S. Fuengfung, P. Phunudom, A. Thaibunnak, N. Juntong, S. Rungruang and U. Pakdee, *Micromachines*, 2022, **13**, 462.
42 G. T. Taulo, N. M. Shaalan, G. G. Mohamed, M. M. Ayad and A. Abd El-Moneim, *Ceram. Int.*, 2024, **50**, 18638–18646.
43 S. Zheng, H. Wang, P. Das, Y. Zhang, Y. Cao, J. Ma, S. F. Liu and Z. S. Wu, *Adv. Mater.*, 2021, **33**, e2005449.
44 M. A. Belal, H. H. Khalil, R. L. Mahajan, A. E. Rashed, S. N. Khattab and A. Abd El-Moneim, *J. Energy Storage*, 2024, **101**, 113900.
45 A. Lorenz, M. Klawitter, M. Linse, L. Ney, S. Tepner, S. Pingel, M. S. Sabet, J. Reiner, K. Oehrle and R. Greutmann, *Energy Technol.*, 2022, **10**, 2200377.
46 L. E. Chaney, W. J. Hyun, M. Khalaj, J. Hui and M. C. Hersam, *Adv. Mater.*, 2023, e2305161.
47 W. Yang, Z. Hu, C. Zhang, Y. Guo and J. Zhao, *Electrochim. Acta*, 2022, **429**, 141041.
48 S. Xu, Y. Dall'Agnese, G. Wei, C. Zhang, Y. Gogotsi and W. Han, *Nano Energy*, 2018, **50**, 479–488.
49 S. Park, S. Ban, N. Zavanelli, A. E. Bunn, S. Kwon, H. R. Lim, W. H. Yeo and J. H. Kim, *ACS Appl. Mater. Interfaces*, 2023, **15**, 2092–2103.
50 X. Lin, X. Li, Z. Zhang, X. Li, W. Zhang, J. Xu and K. Song, *Mater. Today Chem.*, 2023, **30**, 101529.
51 A. N. Gafurov, T. H. Phung, B. H. Ryu, I. Kim and T. M. Lee, *Int. J. Precis. Eng. Manuf.*, 2023, **10**, 339–352.
52 H. C. Weerasinghe, N. Macadam, J. E. Kim, L. J. Sutherland, D. Angmo, L. W. T. Ng, A. D. Scully, F. Glenn, R. Chantler, N. L. Chang, M. Dehghanimadvar, L. Shi, A. W. Y. Ho-Baillie, R. Egan, A. S. R. Chesman, M. Gao, J. J. Jasieniak, T. Hasan and D. Vak, *Nat. Commun.*, 2024, **15**, 1656.
53 I. Brunetti, F. Ferrari, N. J. Pataki, S. Abdolhosseinzadeh, J. Heier, L. J. A. Koster, U. Lemmer, M. Kemerink and M. Caironi, *Adv. Mater. Technol.*, 2024, **9**, 2302058.
54 B. M. Szydlowska, C. C. Pola, Z. Cai, L. E. Chaney, J. Hui, R. Sheets, J. Carpenter, D. Dean, J. C. Claussen, C. L. Gomes and M. C. Hersam, *ACS Appl. Mater. Interfaces*, 2024, **16**, 25169–25180.
55 B. A. Minyawi, M. Vaseem, N. A. Alhebshi, A. M. Al-Amri and A. Shamim, *Nanomaterials*, 2023, **13**, 2567.
56 S. A. Ahire, P. B. Koli, A. V. Patil, B. S. Jagdale, A. A. Bachhav and T. B. Pawar, *Curr. Res. Green Sustainable Chem.*, 2021, **4**, 100213.
57 S. Das, M. L. Rahman, P. P. Mondal, P. L. Mahapatra and D. Saha, *Ceram. Int.*, 2021, **47**, 33515–33524.
58 A. Yoshida, G. Méhes, Y. Okuyama, M. Murakata, T. Shiba and S. Tokito, *Adv. Electron. Mater.*, 2023, 2300615.
59 A. D. Garje, M. Mayaji Ovhal, S. Mishra and N. Bagwe, *Adv. Mater. Lett.*, 2020, **11**, 1–7.
60 K. Pungjunun, S. Chaiyo, N. Praphairaksit, W. Siangproh, A. Ortner, K. Kalcher, O. Chailapakul and E. Mehmeti, *Biosens. Bioelectron.*, 2019, **143**, 111606.
61 H. Wan, X. Liu, X. Y. Wang, Y. T. Chen and P. Wang, *J. Electrochem. Soc.*, 2021, **168**, 067514.
62 C. Mao, Y. Tian, X. Zhou, J. Bai, S. Ma and H. Wang, *Colloids Surf., A*, 2024, **682**, 132982.
63 Y. X. Tian, C. B. Mao, X. Y. Zhou, H. Zhang, L. X. Yin, S. H. Ma and H. Wang, *Colloids Surf., A*, 2024, **697**, 134453.
64 R. R. Suresh, M. Lakshmanakumar, J. B. B. A. Jayalatha, K. S. Rajan, S. Sethuraman, U. M. Krishnan and J. B. B. Rayappan, *J. Mater. Sci.*, 2021, **56**, 8951–9006.
65 G. Barandun, L. Gonzalez-Macia, H. S. Lee, C. Dincer and F. Guder, *ACS Sens.*, 2022, **7**, 2804–2822.
66 L. Zhou, Z. Hu, P. Wang, N. Gao, B. Zhai, M. Ouyang, G. Zhang, B. Chen, J. Luo, S. Jiang, H.-Y. Li and H. Liu, *Sens. Actuators, B*, 2022, **361**, 131735.
67 F. K. Algethami, A. Rabti, M. Mastouri, B. Y. Abdulkhair, S. Ben Aoun and N. Raouafi, *RSC Adv.*, 2023, **13**, 21336–21344.
68 A. Beniwal, P. Ganguly, A. K. Aliyana, G. Khandelwal and R. Dahiya, *Sens. Actuators, B*, 2023, **374**, 132731.
69 S. N. Birajdar and P. V. Adhyapak, *Ceram. Int.*, 2020, **46**, 27381–27393.

70 S. M. Majhi, A. Ali, Y. E. Greish, H. F. El-Maghraby and S. T. Mahmoud, *Sci. Rep.*, 2023, **13**, 3114.
71 S. Jaballah, Y. Alaskar, I. AlShunaifi, I. Ghiloufi, G. Neri, C. Bouzidi, H. Dahman and L. El Mir, *Chemosensors*, 2021, **9**, 300.
72 W. J. Pan, Y. Zhang, S. J. Yu, X. H. Liu and D. Z. Zhang, *Sens. Actuators, B*, 2021, **344**, 130221.
73 J. Tan, S. Hussain, C. X. Ge, M. S. Wang, S. Shah, G. W. Liu and G. J. Qiao, *Sens. Actuators, B*, 2020, **303**, 127251.
74 C. Fan, F. Sun, X. Wang, M. Majidi, Z. Huang, P. Kumar and B. Liu, *J. Mater. Sci.*, 2020, **55**, 7702–7714.
75 M. Krawczyk, P. Suchorska-Wozniak, R. Szukiewicz, M. Kuchowicz, R. Korbutowicz and H. Teterycz, *Nanomaterials*, 2021, **11**, 456.
76 Z. Deng, Y. Zhang, D. Xu, B. Zi, J. Zeng, Q. Lu, K. Xiong, J. Zhang, J. Zhao and Q. Liu, *ACS Sens.*, 2022, **7**, 2577–2588.
77 M. Hou, S. Guo, L. Yang, J. Gao, T. Hu, X. Wang and Y. Li, *Ceram. Int.*, 2021, **47**, 7728–7737.
78 X. H. Zheng, S. L. Zhang, M. J. Zhou, H. B. Lu, S. Guo, Y. X. Zhang, C. L. Li and S. C. Tan, *Adv. Funct. Mater.*, 2023, **33**, 2214880.
79 S. D. Lawaniya, S. Kumar, Y. Yu, Y. K. Mishra and K. Awasthi, in *Complex and Composite Metal Oxides for Gas VOC and Humidity Sensors Volume 1*, 2024, pp. 107–150.
80 S. D. Lawaniya, S. Kumar, Y. T. Yu, H. G. Rubahn, Y. K. Mishra and K. Awasthi, *Mater. Today Chem.*, 2023, **29**, 101428.
81 Z.-M. Török, A. F. Blaser, K. Kavianynejad, C. G. M. G. de Torrella, L. Nsubuga, Y. K. Mishra, H.-G. Rubahn and R. de Oliveira Hansen, *Chemosensors*, 2022, **10**, 167.
82 Y. Zhang, Y. Li, Y. Jiang, Z. Duan, Z. Yuan, B. Liu, Q. Huang, Q. Zhao, Y. Yang and H. Tai, *Sens. Actuators, B*, 2024, **411**, 135788.
83 T. Murugesan, R. R. Kumar, A. Ranjan, M.-Y. Lu and H.-N. Lin, *Sens. Actuators, B*, 2024, **402**, 135106.
84 X. Duan, Y. Jiang, B. Liu, Z. Duan, Y. Zhang, Z. Yuan and H. Tai, *Sens. Actuators, B*, 2024, **402**, 135136.
85 Z. Yuan, Q. Zhao, Z. Duan, C. Xie, X. Duan, S. Li, Z. Ye, Y. Jiang and H. Tai, *Sens. Actuators, B*, 2022, **363**, 131790.
86 X. Duan, Z. Duan, Y. Zhang, B. Liu, X. Li, Q. Zhao, Z. Yuan, Y. Jiang and H. Tai, *Sens. Actuators, B*, 2022, **369**, 132302.
87 Y. Li, B. Zhang, J. Li, Z. Duan, Y. Yang, Z. Yuan, Y. Jiang and H. Tai, *Chemosensors*, 2024, **12**, 43.
88 Y. Guo, B. H. Liu, Z. H. Duan, Z. Yuan, Y. D. Jiang and H. L. Tai, *Mater. Chem. Phys.*, 2023, **302**, 127768.
89 Z. Cui, K. Yang, Y. Shen, Z. Yuan, Y. Dong, P. Yuan and E. Li, *Appl. Surf. Sci.*, 2023, **613**, 155978.
90 V. Balasubramani, T. M. Sridhar and B. Liu, *Ceram. Int.*, 2024, **50**, 4359–4373.
91 A. Boublia, Z. Guezzout, N. Haddaoui, M. Badawi, A. S. Darwish, T. Lemaoui, F. Banat, K. K. Yadav, B.-H. Jeon, N. Elboughdiri, Y. Benguerba and I. M. AlNashef, *J. Mater. Chem. A*, 2024, **12**, 2209–2236.
92 G. Manjunath, R. V. Vardhan, L. L. Praveen, P. Nagaraju and S. Mandal, *Appl. Phys.*, 2021, **127**, 116.
93 A. Yoshida, Y.-F. Wang, S. Tachibana, A. Hasegawa, T. Sekine, Y. Takeda, J. Hong, D. Kumaki, T. Shiba and S. Tokito, *Carbon Trends*, 2022, **7**, 100166.
94 N. Yi, Y. Gao, A. L. Verso Jr, J. Zhu, D. Erdely, C. Xue, R. Lavelle and H. Cheng, *Mater. Today*, 2021, **50**, 24–34.
95 X. Guan, Z. N. Hou, K. Wu, H. R. Zhao, S. Liu, T. Fei and T. Zhang, *Sens. Actuators, B*, 2021, **339**, 129879.
96 Z. Wu, H. Wang, Q. Ding, K. Tao, W. Shi, C. Liu, J. Chen and J. Wu, *Adv. Funct. Mater.*, 2023, **33**, 2300046.
97 S. D. Lawaniya, S. Kumar, Y. T. Yu and K. Awasthi, *ACS Appl. Polym. Mater.*, 2023, **5**, 1945–1954.
98 H. Ma, Y. Jiang, J. Ma, X. Ma, M. Xue and N. Zhu, *Anal. Chem.*, 2020, **92**, 5897–5903.
99 J. Guo, W. Li, X. Zhao, H. Hu, M. Wang, Y. Luo, D. Xie, Y. Zhang and H. Zhu, *Molecules*, 2021, **26**, 6475.
100 W. Wang, Q. Zhang, R. Lv, D. Wu and S. Zhang, *Sensors*, 2021, **21**, 3947.
101 G. Deokar, J. Casanova-Cháfer, N. S. Rajput, C. Aubry, E. Llobet, M. Jouiad and P. M. F. J. Costa, *Sens. Actuators, B*, 2020, **305**, 127458.
102 M. A. A. Rehmani, K. Lal, A. Shaukat and K. M. Arif, *Sci. Rep.*, 2022, **12**, 6928.
103 Y. K. Jo, S. Y. Jeong, Y. K. Moon, Y. M. Jo, J. W. Yoon and J. H. Lee, *Nat. Commun.*, 2021, **12**, 4955.
104 N. L. Myadam, D. Y. Nadargi, J. D. Nadargi and M. G. Chaskar, *J. Sol-Gel Sci. Technol.*, 2020, 56–66.
105 A. Lorenz, M. Klawitter, M. Linse, S. Tepner, J. Röth, N. Wirth, R. Greutmann, M. Lehner, A. Senne and D. Reukauf, *AIP Conf. Proc.*, 2021, **2367**, 020008.
106 L. Gillan and E. Jansson, *Flexible Printed Electron.*, 2022, **7**, 025014.
107 O.-H. Huttunen, T. Happonen, J. Hiitola-Keinänen, P. Korhonen, J. Ollila and J. Hiltunen, *Ind. Eng. Chem. Res.*, 2019, **58**, 19909–19916.
108 A. K. Vishwakarma and L. Yadava, *Environ. Sci. Pollut. Res. Int.*, 2021, **28**, 3920–3927.
109 Y. K. Park, H. J. Oh, J. H. Bae, J. Y. Lim, H. D. Lee, S. I. Hong, H. S. Son, J. H. Kim, S. J. Lim and W. Lee, *Polymers*, 2020, 2595.
110 D. S. Kim, J. M. Jeong, H. J. Park, Y. K. Kim, K. G. Lee and B. G. Choi, *Nano-Micro Lett.*, 2021, **13**, 87.
111 Z. H. Zargar, K. J. Akram, G. R. Biswal and T. Islam, *IEEE Trans. Instrum. Meas.*, 2021, **70**, 1–8.
112 Y. K. Park, H. J. Oh, J. H. Bae, J. Y. Lim, H. D. Lee, S. I. Hong, H. S. Son, J. H. Kim, S. J. Lim and W. Lee, *Polymers*, 2020, **12**, 2595.
113 J. Lee, G. Hussain, N. Lopez-Salas, D. R. MacFarlane and D. S. Silvester, *Analyst*, 2020, **145**, 1915–1924.
114 G. Manjunath, P. Nagaraju and S. Mandal, *J. Mater. Sci. Mater. Electron.*, 2021, **32**, 5713–5728.
115 C. Fisher, B. J. Warmack, Y. C. Yu, L. N. Skolrood, K. Li, P. C. Joshi, T. Saito and T. Aytug, *J. Mater. Sci.*, 2021, **56**, 12596–12606.
116 C. Fan, F. Z. Sun, X. M. Wang, M. Majidi, Z. Z. Huang, P. Kumar and B. Liu, *J. Mater. Sci.*, 2020, 7702–7714.
117 Agustina, M. T. Ulhakim, A. Setiawan, D. G. Syarif and E. Suhendi, *KnE Life Sci.*, 2024, 40–50.
118 S. M. Yenorkar, R. N. Zade, B. M. Mude, V. M. Mayekar, K. M. Mude, K. B. Raulkar, R. R. Mistry and A. N. Patange, *Macromol. Symp.*, 2021, **400**, 2100049.

119 J. Cong, P. Duan, F. Zhong, Y. Luo, Y. Zheng, G. Cai, Y. Xiao and L. Jiang, *Sens. Actuators, B*, 2020, **303**, 127220.
120 V. N. Narwade, K. A. Bogle and V. Kokol, *Emerg. Mater.*, 2021, **5**, 445–454.
121 A. A. Kabure, B. S. Shirke, S. R. Mane, K. M. Garadkar, B. M. Sargar and K. S. Pakhare, *Appl. Phys.*, 2021, **127**, 711.
122 S. D. Patil, H. A. Nikam, Y. C. Sharma, R. S. Yadav, D. Kumar, A. K. Singh and D. R. Patil, *Sens. Actuators, B*, 2023, **377**, 133080.
123 P. R. Chaudhari, V. M. Gaikwad and S. A. Acharya, *Ferroelectrics*, 2022, **587**, 76–83.
124 N. L. Myadam, D. Y. Nadargi, J. D. Nadargi and M. G. Chaskar, *J. Sol–Gel Sci. Technol.*, 2020, **96**, 56–66.
125 A. Al Shboul and R. Izquierdo, presented in part at the *2021 IEEE International Conference on Flexible and Printable Sensors and Systems (FLEPS)*, 2021.
126 A. Korent, K. Zagar Soderznik, S. Sturm, K. Zuzek Rozman, N. Redon, J. L. Wojkiewicz and C. Duc, *Sensors*, 2020, **21**, 169.
127 R. Ma, W. Gan, X. Peng, P. Feng and J. Chu, *Mater. Res. Bull.*, 2024, **175**, 112775.
128 M.-y. Yang, M.-l. Huang, Y.-z. Li, Z.-s. Feng, Y. Huang, H.-j. Chen, Z.-q. Xu, H.-g. Liu and Y. Wang, *Sens. Actuators, B*, 2022, **364**, 131867.
129 Z. Zhang, M. Chen, S. Alem, Y. Tao, T.-Y. Chu, G. Xiao, C. Ramful and R. Griffin, *Sens. Actuators, B*, 2022, **359**, 131620.
130 A. Rivadeneyra, J. F. Salmeron, F. Murru, A. Lapresta-Fernandez, N. Rodriguez, L. F. Capitan-Vallvey, D. P. Morales and A. Salinas-Castillo, *Nanomaterials*, 2020, **10**, 2446.
131 C. C. Yang, A. Abodurexiti and X. Maimaitiyiming, *Macromol. Mater. Eng.*, 2020, **305**, 2070017.
132 L. P. Ge, X. Ye, Z. P. Yu, B. Chen, C. J. Liu, H. Guo, S. Y. Zhang, F. Sassa and K. Hayashi, *npj Flexible Electron.*, 2022, **6**, 40.
133 M. A. Belal, R. Yousry, G. Taulo, A. A. AbdelHamid, A. E. Rashed and A. A. El-Moneim, *ACS Appl. Mater. Interfaces*, 2023, **15**, 53632–53643.
134 J. Krzemiński, D. Baraniecki, J. Dominiczak, I. Wojciechowska, T. Raczyński, D. Janczak and M. Jakubowska, *Crystals*, 2023, **13**, 720.
135 M. Ezzat, A. E. Rashed, S. A. Sabra, M. Haroun and A. Abd El-Moneim, *Mater. Today Commun.*, 2023, **37**, 107549.
136 U. Chakraborty, A. Kaushik, G. R. Chaudhary and Y. K. Mishra, *Curr. Opin. Environ. Sci. Health*, 2024, **37**, 100532.
137 N. Dhariwal, P. Yadav, A. Sanger, S. B. Kang, M. S. Goyat, Y. K. Mishra and V. Kumar, *Mater. Adv.*, 2024, **5**, 4187–4199.
138 W. Bian, H. Dou, X. Wang, C. Li, Y. Zhang, C. Gong, N. Sun, S. Liu, P. Li, Q. Jing and B. Liu, *ACS Sens.*, 2023, **8**, 748–756.
139 B. Cho, A. R. Kim, Y. Park, J. Yoon, Y. J. Lee, S. Lee, T. J. Yoo, C. G. Kang, B. H. Lee, H. C. Ko, D. H. Kim and M. G. Hahm, *ACS Appl. Mater. Interfaces*, 2015, **7**, 2952–2959.
140 P. Yu, M. Zhang, M. You, Y. Gao, L. Xiao, Y. Peng, J. Lai, Z. Shi, S. Luo, G. Guo and G. Guo, *Sens. Actuators, A*, 2024, **365**, 114864.
141 A. Kumar Gangwar, R. Godiwal, U. Varshney, S. Das, J. S. Tawale, G. Gupta and P. Singh, *Appl. Surf. Sci.*, 2024, **655**, 159607.
142 P. Wang, X. Tian, M. Yan, B. Yang and Z. Hua, *J. Mater. Sci.*, 2020, **56**, 4666–4676.
143 C. X. Zhang, S. Zhang, D. N. Zhang, Y. Yang, J. R. Zhao, H. Yu, T. T. Wang, T. Q. Wang and X. T. Dong, *Sens. Actuators, B*, 2023, **390**, 133894.
144 M. Hassan, Z. Liang, S. Liu, S. Hussain, G. Qiao and G. Liu, *Sens. Actuators, B*, 2024, **398**, 134755.
145 R. J. Xie, J. B. Lu and Y. Q. Liu, *Sens. Actuators, A*, 2024, **367**, 115038.
146 P. Bharathi, S. Harish, M. Shimomura, M. K. Mohan, J. Archana and M. Navaneethan, *Chemosphere*, 2024, **346**, 140486.
147 S. Park, T. Y. Eom, R. H. Jeong, H. J. Lee and J. H. Boo, *Appl. Surf. Sci.*, 2024, **657**, 159746.
148 S. Xu, J. Lu, D. Jin and H. Jin, *Chem. Phys.*, 2024, **582**, 112296.
149 M. Du, L. Zhang, R. Jiang, C. Hu, Y. Feng, S. Wang and J. Cao, *Colloids Surf., A*, 2024, **681**, 132804.
150 Y. F. Gao, X. H. Wang, Z. G. Zhang, J. H. Li, H. Y. Wang, G. G. Xu, X. Z. Wang and J. Tian, *Sens. Actuators, B*, 2024, **404**, 135271.
151 X. Liu, H. Zhang, T. Shen and J. Sun, *Ceram. Int.*, 2024, **50**, 2459–2466.
152 J. N. O. Amu-Darko, S. Hussain, M. Y. Wang, S. Y. Lei, A. A. Alothman, S. Mohammad, G. J. Qiao and G. W. Liu, *Sens. Actuators, B*, 2024, **407**, 135464.
153 A. Govind, P. Bharathi, S. Harish, M. Krishna Mohan, J. Archana and M. Navaneethan, *Appl. Surf. Sci.*, 2024, **657**, 159604.
154 P. S. Chauhan, A. Mishra, G. Bhatt and S. Bhattacharya, *Mater. Sci. Semicond. Process.*, 2021, **123**, 105528.
155 B. Sharma, J.-S. Sung, A. A. Kadam and J.-h. Myung, *Appl. Surf. Sci.*, 2020, **530**, 147272.
156 O. Tsymbalenko, S. Lee, Y. M. Lee, Y. S. Nam, B. C. Kim, J. Y. Kim and K. B. Lee, *Mikrochim. Acta*, 2023, **190**, 134.
157 S. Tyagi, A. Kumar, A. Kumar, Y. K. Gautam, V. Kumar, Y. Kumar and B. P. Singh, *Mater. Res. Bull.*, 2022, **150**, 111784.
158 S. M. Merah, Y. Bakha and A. Djelloul, *J. Mater. Sci. Mater. Electron.*, 2024, **35**, 250.
159 R. Wu, J. Hao, S. Zheng, Q. Sun, T. Wang, D. Zhang, H. Zhang, Y. Wang and X. Zhou, *Appl. Surf. Sci.*, 2022, **571**, 151162.
160 S. Dietrich, M. Kusnezoff, U. Petasch and A. Michaelis, *Sensors*, 2021, **21**, 497.
161 E. Ciftyurek, Z. Li and K. Schierbaum, *Sensors*, 2022, **23**, 29.
162 C. Y. Yang, B. H. Liu, Y. Yang, T. T. Wang, T. Q. Wang, H. Yu and X. T. Dong, *Sens. Actuators, B*, 2022, **362**, 131754.
163 S. R. Luo, R. J. Chen, J. Wang and L. Xiang, *Sens. Actuators, B*, 2023, **383**, 133600.
164 D. Huang, W. J. Yuan, S. R. Fan, C. Tian, Z. Q. Hua, X. M. Tian, Y. Wu and E. P. Li, *Sens. Actuators, B*, 2020, **304**, 127339.

165 J. Wang, R. Xu, Y. Xia and S. Komarneni, *Ceram. Int.*, 2021, **47**, 34437–34442.
166 Z. Marinkovic, G. Gugliandolo, M. Latino, G. Campobello, G. Crupi and N. Donato, *Sensors*, 2020, **20**, 7150.
167 S. K. Ayyala and J. A. Covington, *Chemosensors*, 2021, **9**, 247.
168 L. Kulhari, K. Ray, A. Paptan, N. Suri and P. K. Khanna, *Int. J. Appl. Ceram. Technol.*, 2020, **17**, 1430–1439.
169 H. Y. Alolaywi, S. Duanghathaipornsuk, S. S. Kim, C. H. Li, J. R. Jinschek, D. S. Kim and A. C. Alba-Rubio, *J. Electrochem. Soc.*, 2021, **168**, 067525.
170 P. Wu, Y. Li, S. Xiao, J. Chen, J. Tang, D. Chen and X. Zhang, *J. Hazard. Mater.*, 2022, **422**, 126882.
171 A. Madbouly, A. Elzwawy and M. Morsy, *Ceram. Int.*, 2024, **50**, 25473–25483.
172 T. Akamatsu, T. Itoh, N. Izu and W. Shin, *Sensors*, 2013, **13**, 12467–12481.
173 Medical gallery of Mikael Häggström, *WikiJournal of Medicine*, 2014.
174 B. Yang, Z. Zhang, C. Tian, W. Yuan, Z. Hua, S. Fan, Y. Wu and X. Tian, *Sens. Actuators, B*, 2020, **321**, 128567.
175 R. Haribhau Waghchaure, V. Ashok Adole, B. Sonu Jagdale and P. Bhimrao Koli, *Inorg. Chem. Commun.*, 2022, **140**, 109450.
176 S. Taha, S. Begum, V. N. Narwade, D. I. Halge, J. W. Dadge, M. P. Mahabole, R. S. Khairnar and K. A. Bogle, *Mater. Chem. Phys.*, 2020, **240**, 122228.
177 S. N. Birajdar and P. V. Adhyapak, *Ceram. Int.*, 2020, 27381–27393.
178 D. M. ME, N. G. Sundaram, A. Singh, A. K. Singh and S. B. Kalidindi, *Chem. Commun.*, 2019, **55**, 349–352.
179 J. Y. Park, Y. Kwak, H. R. Lim, S. W. Park, M. S. Lim, H. B. Cho, N. V. Myung and Y. H. Choa, *J. Hazard. Mater.*, 2022, **438**, 129412.
180 J. Jaiswal, P. Singh and R. Chandra, *Sens. Actuators, B*, 2021, **327**, 128862.
181 Z. Cheng, R. Fan, J. Liao, G. Yuan, X. Wu, W. Pi, W. Zou, X. Ma and M. Wang, *Cryst. Growth Des.*, 2024, **24**, 2900–2908.
182 Z. W. Cheng, R. Y. Fan, J. J. Liao, G. Yuan, X. Q. Wu, W. B. Pi, W. Zou, X. G. Ma and M. Wang, *Cryst. Growth Des.*, 2024, 2900–2908.
183 R. Sivakumar, K. Krishnamoorthi, S. Vadivel and S. Govindasamy, *Diamond Relat. Mater.*, 2021, 108418.
184 O. Ogbeide, G. Bae, W. B. Yu, E. Morrin, Y. Y. Song, W. Song, Y. Li, B. L. Su, K. S. An and T. Hasan, *Adv. Funct. Mater.*, 2022, **32**, 2113348.
185 S. G. Onkar, F. C. Raghuwanshi, D. R. Patil and T. Krishnakumar, *Mater. Today: Proc.*, 2020, **23**, 190–201.
186 T. V. K. Karthik, A. G. Hernandez, Y. Kudriavtsev, H. Gómez-Pozos, M. G. Ramírez-Cruz, L. Martínez-Ayala and A. Escobosa-Echvarria, *J. Mater. Sci. Mater. Electron.*, 2020, **31**, 7470–7480.
187 C. A. Zito, T. M. Perfecto, A. C. Dippel, D. P. Volanti and D. Koziej, *ACS Appl. Mater. Interfaces*, 2020, **12**, 17745–17751.
188 F. Le Pennec and M. Bendahan, *Int. J. Adv. Syst. Meas.*, 2020, **13**, 333–342.
189 P. Escobedo, M. D. Fernandez-Ramos, N. Lopez-Ruiz, O. Moyano-Rodriguez, A. Martinez-Olmos, I. M. Perez de Vargas-Sansalvador, M. A. Carvajal, L. F. Capitan-Vallvey and A. J. Palma, *Nat. Commun.*, 2022, **13**, 72.
190 P. Awandkar and S. Yawale, *Polym.-Plast. Technol. Mater.*, 2024, **63**, 605–612.
191 Q. Zhou, W. Zeng, W. G. Chen, L. N. Xu, R. Kumar and A. Umar, *Sens. Actuators, B*, 2019, **298**, 126870.
192 X. S. Cui, Z. R. Lu, Z. C. Wang, W. Zeng and Q. Zhou, *Chemosensors*, 2013, 58.
193 X. N. Meng, M. S. Bi, Q. P. Xiao and W. Gao, *Int. J. Hydrogen Energy*, 2022, 3157–3169.
194 X. Cui, Z. Lu, Z. Wang, W. Zeng and Q. Zhou, *Chemosensors*, 2023, **11**, 58.
195 A. Gaiardo, B. Fabbri, A. Giberti, M. Valt, S. Gherardi, V. Guidi, C. Malagù, P. Bellutti, G. Pepponi, D. Casotti, G. Cruciani, G. Zonta, N. Landini, M. Barozzi, S. Morandi, L. Vanzetti, R. Canteri, M. Della Ciana, A. Migliori and E. Demenev, *Sens. Actuators, B*, 2020, **305**, 127485.
196 S. Kumar, S. D. Lawaniya, S. Agarwal, Y.-T. Yu, S. R. Nelamarri, M. Kumar, Y. K. Mishra and K. Awasthi, *Sens. Actuators, B*, 2023, **375**, 132943.
197 X. N. Meng, M. S. Bi, Q. P. Xiao and W. Gao, *Int. J. Hydrogen Energy*, 2022, **47**, 3157–3169.
198 L. Huo, G. Li, C. Wu, X. He, X. Zhao, T. Tao, B. Liang, S.-G. Lu and Y. Yao, *Highly Selective H_2 Gas Sensor Based on Ag Modified Sno_2 Nanoparticles*, available at SSRN, DOI: 10.2139/ssrn.4697561.
199 J. M. Li, Y. X. Li, S. H. Li and Y. F. Guan, *Sens. Actuators, B*, 2024, **409**, 135591.
200 M. Siriwalai, M. Punginsang, K. Inyawilert, A. Wisitsoraat and C. Liewhiran, *J. Mater. Sci. Eng. B*, 2024, **299**, 116968.
201 U. Jagannath Tupe, M. S. Zambare, A. Vitthal Patil and P. Bhimrao Koli, *Mater. Sci. Res. India*, 2020, **17**, 260–269.
202 W. Pan, Y. Zhang, S. Yu, X. Liu and D. Zhang, *Sens. Actuators, B*, 2021, 130221.
203 J. Tan, S. Hussain, C. Ge, M. Wang, S. Shah, G. Liu and G. Qiao, *Sens. Actuators, B*, 2020, 127251.
204 S. Y. Cai, G. J. Song, G. F. Zhang, L. Wang, T. L. Jian, J. T. Xu, F. Y. Su and Y. Q. Tian, *Sens. Actuators, B*, 2022, **367**, 132153.
205 B. Yang, C. Wang, R. Xiao, H. Yu, J. Wang, H. Liu, F. Xia and J. Xiao, *Mater. Chem. Phys.*, 2020, **239**, 122302.
206 A. T. Guntner, M. Wied, N. J. Pineau and S. E. Pratsinis, *Adv. Sci.*, 2020, **7**, 1903390.
207 M. Sai Bhargava Reddy, S. Kailasa, B. Geeta Rani, N. Jayarambabu, K. Bikshalu, P. Munindra and K. Venkateswara Rao, *J. Mater. Sci.: Mater. Electron.*, 2019, **30**, 17295–17302.
208 V. Munusami, K. Arutselvan, S. Vadivel and S. Govindasamy, *Ceram. Int.*, 2022, 29322–29331.
209 P. K. Singh, N. Singh, M. Singh, S. K. Singh and P. Tandon, *Appl. Phys. A*, 2021, **127**, 563.
210 A. K. Vishwakarma, A. K. Sharma, A. K. Mishra and L. Yadava, *National Conference on Environmental Toxicology:Impact on Human Health*, Envtox 2021, Pt 4, 2022, vol. 69, pp. A18–A21.

211 T. Nakajima, Y. Fujio, T. Sugahara and T. Tsuchiya, *Sensors*, 2022, **22**, 1996.
212 H. Wang, M. Chen, Q. Rong, Y. Zhang, J. Hu, D. Zhang, S. Zhou, X. Zhao, J. Zhang, Z. Zhu and Q. Liu, *Nanotechnology*, 2020, **31**, 255501.
213 N. Hikmah, H. F. Hawari and M. Gupta, *Indones. J. Electr. Eng. Comput. Sci.*, 2020, **19**, 119.
214 A. Douaki, B. Demelash Abera, G. Cantarella, B. Shkodra, A. Mushtaq, P. Ibba, A. S. Inam, L. Petti and P. Lugli, *Nanomaterials*, 2020, **10**, 1167.
215 R. Hopper, D. Popa, F. Udrea, S. Z. Ali and P. Stanley-Marbell, *Sci. Rep.*, 2022, **12**, 1690.
216 B. C. Hauck, B. S. Ince and P. C. Riley, *ACS Sens.*, 2023, **8**, 2945–2951.
217 D. N. Barreto, R. Gelamo, B. Mizaikoff and J. Petruci, *ACS Omega*, 2024, **9**, 8374–8380.
218 Y. Zhu, L. Yang, S. Guo, M. Hou and Y. Ma, *Materials*, 2023, **16**, 792.
219 C. Wang, Y. Wang, K. O. Kirlikovali, K. Ma, Y. Zhou, P. Li and O. K. Farha, *Adv. Mater.*, 2022, **34**, e2202287.
220 B. Yang, J. Yu, W. Liu, G. Jing, W. Li and W. Liu, *Sensors*, 2022, **22**, 5468.
221 H. Y. Zhou, S. Y. Li, S. J. Chen, Q. Q. Zhang, W. J. Liu and X. J. Guo, *IEEE Sens. J.*, 2020, **20**, 5004–5011.
222 A. Verma, D. Yadav, S. Natesan, M. Gupta, B. C. Yadav and Y. K. Mishra, *Microchem. J.*, 2024, **201**, 110713.
223 H. X. Liu, L. H. Peng, D. Li and W. H. Shen, *J. Mater. Sci. Mater. Electron.*, 2024, **35**, 359.
224 R. M. Shedam, M. shedam and A. B. Gadkari, *Ethanol Sensor Based on Nano Crystalline Nd3+ Substituted in Mg-Cd Ferrite Thick Film*, available at SSRN 4809197, 2024.
225 M. S. Yang, J. M. Liu, C. X. Hu, W. Q. Zhang, J. Y. Jiao, N. Y. Cui and L. Gu, *J. Mater. Chem. A*, 2023, **11**, 21937–21947.
226 J. X. Zhu, M. Cho, Y. T. Li, T. Y. He, J. Ahn, J. Park, T. L. Ren, C. K. Lee and I. Park, *Nano Energy*, 2021, **86**, 106035.
227 O. Kul, A. Vasiliev, A. Nikitin, A. Dmitrieva and A. Bolshakov, *Proceedings*, 2024, **97**, 128.
228 D. Boonthum, C. Oopathump, S. Fuengfung, P. Phunudom, A. Thaibunnak, N. Juntong, S. Rungruang and U. Pakdee, *Micromachines*, 2022, **13**, 462.
229 S. A. M. Chachuli, W. H. Ying, N. H. Shamsudin and O. Coban, *J. Eng. Technol. Sci.*, 2024, **56**, 593–602.
230 M. Masat, H. K. Sağlam, H. Korul and M. Ertuğrul, *AIP Conf. Proc.*, 2022, **2506**, 080002.
231 W. Zhang, L. Wang, J. Chen, W. Xiao and X. Bi, *IEEE Trans. Instrum. Meas.*, 2021, **70**, 1–14.
232 M. Gheibi, H. Taghavian, R. Moezzi, S. Waclawek, J. Cyrus, A. Dawiec-Lisniewska, J. Koci and M. Khaleghiabbasabadi, *Chemosensors*, 2023, **11**, 126.
233 C. Bruno, A. Licciardello, G. A. M. Nastasi, F. Passaniti, C. Brigante, F. Sudano, A. Faulisi and E. Alessi, *Smart Systems Integration (SSI)*, 2021, pp. 1–5.
234 A. Gupta and V. R. Kumar, *IEEE international conference on electronics, computing and communication technologies (CONECCT)*, 2020, pp. 1–6.
235 P. Narkhede, R. Walambe, S. Mandaokar, P. Chandel, K. Kotecha and G. Ghinea, *Appl. Syst. Innov.*, 2021, **4**, 3.
236 S. L. Mu, W. F. Shen, D. W. Lv, W. J. Song and R. Q. Tan, *Sens. Actuators, A*, 2024, **369**, 115210.
237 S. Huang, A. Croy, B. Ibarlucea and G. Cuniberti, in *Machine Learning for Advanced Functional Materials*, Springer, 2023, pp. 21–41.
238 S. Huang, A. Croy, L. A. Panes-Ruiz, V. Khavrus, V. Bezugly, B. Ibarlucea and G. Cuniberti, *Adv. Intell. Syst.*, 2022, **4**, 2200016.
239 J. C. Xu, B. Y. Mu, L. W. Zhang, R. Chai, Y. F. He and X. S. Zhang, *Comput. Electron. Agric.*, 2023, **212**, 108082.
240 J. Li, Y. Ma, Z. Duan, Y. Zhang, X. Duan, B. Liu, Z. Yuan, Y. Wu, Y. Jiang and H. Tai, *Sens. Actuators, B*, 2024, **404**, 135230.
241 M. A. H. Khan, B. Thomson, R. Debnath, A. Motayed and M. V. Rao, *IEEE Sens. J.*, 2020, **20**, 6020–6028.
242 N. Ha, K. Xu, G. H. Ren, A. Mitchell and J. Z. Ou, *Adv. Intell. Syst.*, 2020, **2**, 2000063.
243 F. Le Pennec, S. Bernardini, M. Hijazi, C. Perrin-Pellegrino, K. Aguir and M. Bendahan, *The Fifth International Conference on Advances in Sensors, Actuators, Metering and Sensing*, IARIA, 2020, pp. 6–7.
244 A. K. Aliyana, S. Naveen Kumar, P. Marimuthu, A. Baburaj, M. Adetunji, T. Frederick, P. Sekhar and R. E. Fernandez, *Sci. Rep.*, 2021, **11**, 24321.
245 H. Mei, J. Peng, T. Wang, T. Zhou, H. Zhao, T. Zhang and Z. Yang, *Nano-Micro Lett.*, 2024, **16**, 269.
246 Z. Gu, Z. Zhou, Z. Huang, K. Wang, Z. Cai, X. Hu, L. Li, M. Li, Y. S. Zhao and Y. Song, *Adv. Mater.*, 2020, **32**, e1908006.
247 R. K. Jha, *Second international conference on inventive research in computing applications (ICIRCA)*, IEEE, 2020, pp. 790–793.
248 D. Mitra and A. Saha, *J. Discret. Math. Sci.*, 2022, **25**, 2173–2182.
249 D. Hercog, T. Lerher, M. Truntic and O. Tezak, *Sensors*, 2023, **23**, 6739.
250 K. Devi, R. Mahajan and D. Bagai, *Int. J. Sens. Netw.*, 2024, **45**, 16–25.
251 G. Karthikeyan, A. L. Jeevitha, K. Sowbarnika and G. V. Vignesh, presented in part at the *2023 2nd International Conference on Vision Towards Emerging Trends in Communication and Networking Technologies (ViTECoN)*, 2023.
252 M. F. R. Al-Okby, T. Roddelkopf, H. Fleischer and K. Thurow, *Sensors*, 2022, **22**, 8161.
253 C. I. Parwati, H. P. Suseno and C. Iswahyudi, in *Bali International Seminar Science Technolology*, 2014, pp. 2–5.
254 D. Goyal, S. Patra, A. Sapre, M. Kaur and N. S. Ramgir, *Sens. Imag.*, 2024, **25**, 30.
255 A. M. Pawar, J. Deshpande and S. Patil, *Digit. Signal Process.*, 2020, **8**, 15–26.
256 P. Mane-Deshmukh, B. Ladgaonkar, S. Pathan and S. Shaikh, *Int. J. Adv. Res. Comput. Sci. Software Eng.*, 2013, **3**, 943–950.

257 M. F. R. Al-Okby, S. Junginger, T. Roddelkopf, J. Huang and K. Thurow, *Sensors*, 2024, **24**, 1295.
258 M. Seraj, M. Parvez, O. Khan and Z. Yahya, *Green Technol. Sustainability*, 2024, **2**, 100079.
259 G. Guillen, *Sensor Projects with Raspberry Pi*, Springer, 2019.
260 D. R. Arivalahan, S. Balaji, M. Kamalakannan and T. Vinoth, *Int. J. Electr. Eng. Technol.*, 2021, **12**, 50–61.
261 A. M. Bayoumy, A. Hessein, M. A. Belal, M. Ezzat, M. A. Ibrahim, A. Osman and A. Abd El-Moneim, *J. Power Sources*, 2024, **617**, 235145.
262 A. Hamed, A. Hessein and A. A. El-Moneim, *Appl. Surf. Sci.*, 2021, **551**, 149457.
263 J. Ma, Y. Li, Z. Wang, B. Zhang, J. Du, J. Qin, Y. Cao, L. Zhang, F. Zhou, H. Wang, S. Zheng, L. Feng, S. Liu and Z.-S. Wu, *Mater. Today*, 2024, **74**, 58–66.
264 X. Y. Shi, J. Y. Chang, J. Q. Qin, H. Q. Liu, X. Zhang, Y. W. Ma, J. He, X. J. Chou, L. Feng, Z. S. Wu and X. H. Bao, *Nano Energy*, 2021, **88**, 106253.
265 S. Y. Guo, X. G. Hu, P. X. Hou, Z. Liu, Y. M. Zhzo, Y. G. Li, F. Zhang, C. Liu and H. M. Cheng, *Cell Rep. Phys. Sci.*, 2022, **3**, 101163.
266 S. Hajra, A. Ali, S. Panda, H. W. Song, P. M. Rajaitha, D. Dubal, A. Borras, P. In-Na, N. Vittayakorn, V. Vivekananthan, H. J. Kim, S. Divya and T. H. Oh, *Adv. Energy Mater.*, 2024, 2400025.
267 B. H. Liu, Y. D. Jiang, G. Z. Xie, Z. H. Duan, Z. Yuan, Y. J. Zhang, Q. N. Zhao, Z. M. Cao, F. Dong and H. L. Tai, *Chem. Eng. J.*, 2023, **471**, 144795.
268 Z. Wen, J. Chen, M. H. Yeh, H. Y. Guo, Z. L. Li, X. Fan, T. J. Zhang, L. P. Zhu and Z. L. Wang, *Nano Energy*, 2015, **16**, 38–46.
269 H. Zhang, Y. Yang, Y. Su, J. Chen, C. Hu, Z. Wu, Y. Liu, C. P. Wong, Y. Bando and Z. L. Wang, *Nano Energy*, 2013, **2**, 693–701.
270 N. Mohamadbeigi, L. Shooshtari, S. Fardindoost, M. Vafaiee, A. Iraji Zad and R. Mohammadpour, *Sci. Rep.*, 2024, **14**, 1562.
271 H. R. Ansari, Z. Kordrostami and A. Mirzaei, *Sci. Rep.*, 2023, **13**, 7136.
272 Y. He, X. Shi, K. Chen, X. Yang and J. Chen, *Nanomaterials*, 2020, **10**, 727.
273 S. Anbalagan, K. Manojkumar, M. Muthuramalingam, S. Hajra, S. Panda, R. Sahu, H. J. Kim, A. Sundaramoorthy, N. Nithyavathy and V. Vivekananthan, *Chem. Eng. J.*, 2024, **497**, 154740.
274 S. Kaaliveetil, J. Yang, S. Alssaidy, Z. Li, Y. H. Cheng, N. H. Menon, C. Chande and S. Basuray, *Micromachines*, 2022, **13**, 1716.
275 A. Yeganegi, K. Yazdani, N. Tasnim, S. Fardindoost and M. Hoorfar, *Front. Chem.*, 2023, **11**, 1267187.
276 M. M. Montazeri, A. O'Brien and M. Hoorfar, *Sens. Actuators, B*, 2019, **300**, 126904.
277 K. Ramya, K. Amreen, I. Pronin, A. Karmanov, N. Yakushova and S. Goel, *Nano Futures*, 2023, **7**, 032004.
278 M. Paknahad, C. McIntosh and M. Hoorfar, *Sci. Rep.*, 2019, **9**, 161.